Assessment of the use of global optimisation techniques for aircraft noise source identification

B. von den Hoff

Delft University of Technology

TUDelft

Assessment of the use of global optimisation techniques for aircraft noise source identification

by

B. von den Hoff

to obtain the degree of
Master of Science in Aerospace Engineering
Control and Operations
Aircraft Noise and Climate Effects

at the Delft University of Technology,
to be defended publicly on Wednesday February 12, 2020 at 10:30.

Prof. Dr. Dick G. Simons *Chair holder*	Aircraft Noise and Climate Effects, Delft University of Technology
Dr. ir. Mirjam Snellen *Daily supervisor*	Associate Professor, Aircraft Noise and Climate Effects, Delft University of Technology
Dr. Daphne M. Stam *Independent member*	Associate Professor, Astrodynamics and Space Missions, Delft University of Technology

Cover photo: `https://www.nlr.org/capabilities/aircraft-noise-sources/`

Preface

This report concludes my thesis at Aircraft Noise and Climate Effects, and with it, also my time as student at the Faculty of Aerospace Engineering. In this thesis I researched the applicability of a new method to localise aircraft noise sources on aircraft fly-overs. I target readers who would like to know more on noise source localisation. I expect however that in the research following this, more knowledge on specific aircraft noise sources is gathered.

I chose this thesis topic for a number of reasons. Firstly, the topic sparked my engineering heart and allowed me to enrich my knowledge in the field of acoustics. This topic also allowed me to combine theory with experiments, with field trips to Amsterdam Airport Schiphol to gather my own aircraft noise data set. Lastly, aircraft noise is an extremely relevant subject in today's society and as such I could easily see the practical use of my research.

This thesis brought along difficult times as well. In fact, the following quote summarises my thoughts perfectly.

> In theory, theory and practice are the same. In practice, they are not.
> *Albert Einstein*

I was lucky to have Mirjam as my daily supervisor who explained ever so patiently new parts of theory, and guided me through the times where I could not make sense of practice. Her enthusiasm for the project always encouraged me and for that I would like to thank her greatly.

I would also like to thank Dick for his feedback and critical view during my midterm and greenlight presentation.

Next to Mirjam and Dick, I would like to thank Ana for her support with the acoustic camera. I enjoyed our trips with Vincent to Amsterdam Airport Schiphol and without her, calibrating the acoustic cameras would have been an impossible task.

Lastly, I would like to thank the fellow thesis students, my friends, and my family for the many cups of coffee and the supporting chats!

Bieke von den Hoff
Delft, December 2019

Executive summary

Over the past years, noise nuisance around airports strongly increased. In order to reduce noise, the noise sources should be known. In this research, the objective is to assess a new imaging technique to identify noise sources.

The most common imaging technique is called Conventional Beamforming (CB). Although robust, it is also suffering from limited spatial resolution and high spatial aliasing. Therefore, this research assesses the use of a new imaging technique, Global Optimisation (GO). In previous research, GO proved to be able to localise sound sources in three dimensions and to localise sources under the Rayleigh limit.

In this research GO is applied to four different cases. For the first two cases, the location and source strength of all sources are known, therefore these serve as benchmark cases. These benchmark cases showed that the algorithm is able to localise sources under the Rayleigh limit. However, the results also show that GO has difficulty in identifying the distance between the source and the array when this distance is not equal for all sources.

For the other two cases on which GO is tested, fly-over measurements are used. The fly-over measurements were recorded at Amsterdam Airport Schiphol. In total 324 fly-overs were recorded, of which 238 are take-offs and 86 are landings. This research is the first, to the best of the author's knowledge, to analyse noise sources of aircraft in take-off with beamforming algorithms. From this data set, a single landing and a single take-off were selected. An unexpected noise source was found during the beamforming analysis of the take-off measurements. This noise source was found in the range of 50 to 400 Hz. At these low frequencies the Power Spectral Density (PSD) is 13 dB higher than at 6000 Hz. When no weighting is applied on the data, this low frequency source causes strong spectral leakage. It is hypothesised that this source is caused by interference of the engine jet stream with the wing trailing edge.

GO has been applied on the landing and take-off fly-over measurement. GO had difficulty finding the aircraft height. For the landing case, the locations of the sources were correctly determined. The source strength was correctly determined for the engines, but overestimated slightly for the landing gear. For the take-off case, GO was not able to identify the sources under the Rayleigh limit correctly.

Overall, the results show that GO is a promising method to localise and quantify noise sources. However, in order to improve the performance on fly-over measurements it is recommended to provide the energy function with more knowledge on the aircraft configuration. When GO with the recommended improvements is able to find the aircraft height and localise sources under the Rayleigh limit, the method would add value to the field of acoustic imaging. This would allow researchers to search more freely for noise sources, and, above all, to identify closely spaced or low frequency sources.

Contents

List of Figures

List of Tables

List of Symbols

Greek symbols

α	Atmospheric attenuation (dB/m)
Δt	Time delay (s)
θ	Angle between steering vectors (°)
λ	Wavelength (m)
ν	Functional beamforming exponent (-)
$\boldsymbol{\xi}$	Scan plane grid point vector (m)
σ	Eigenvalues of $\boldsymbol{C}$ (Pa^2)
$\boldsymbol{\Sigma}$	Diagonal matrix with eigenvalues of $\boldsymbol{C}$ (Pa^2)

Roman symbols

A	Source auto-power (Pa^2)
b	Uniform distribution realisation (-)
c	Speed of sound (m/s)
$\boldsymbol{C}$	Cross spectral matrix (Pa^2)
C_{sat}	Saturation constant (-)
$\boldsymbol{d}$	Descendant population vector (m,Pa)
D	Array aperture (m)
D_{tire}	Tire diameter (m)
E	Energy function (-)
f	Frequency (Hz)
$f_{r,N}$	Relaxation frequency of nitrogen (Hz)
$f_{r,O}$	Relaxation frequency of oxygen (Hz)
F	GO multiplication factor (-)
$\boldsymbol{g}$	Steering vector (1/m)
g	Steering vector component (1/m)
h	Perpendicular distance source-receiver, also height (m)
H	Absolute humidity (%)
i	$\sqrt{-1}$ (-)
J	Cost function (-)
$\boldsymbol{m}$	Candidate solution vector (m,Pa)
N_{freq}	Number of frequencies (-)
N_{gen}	Number of generations (-)
N_{runs}	Number of runs (-)
p	Acoustic pressure (Pa)
p_c	GO crossover probability (-)
p_{ref}	Reference pressure, $2 \cdot 10^{-5}$ (Pa)
$\boldsymbol{P}$	Vector of complex acoustic pressures (Pa)
$\hat{P}$	Least-squares solution of acoustic pressure (Pa)
P	Complex acoustic pressure component (Pa)
q	Population size (-)
r	Distance source-receiver (m)
R	Rayleigh distance (m)
RH	Relative humidity (%)
r_F	Fresnel distance (m)
s	Source strength (Pa)
$\boldsymbol{s}$	Partner population vector (m,Pa)
t	Time (s)
T	Temperature (K)
$\boldsymbol{u}$	Eigenvector of $\boldsymbol{C}$ (1/m)
$\boldsymbol{U}$	Eigenvector matrix of $\boldsymbol{C}$ (1/m)
$\boldsymbol{w}$	Normalised steering vector (1/m)
$\boldsymbol{x}$	Microphone position vector (m)

Subscript

γ	Generation member index
air	Value in air at time of measurement
cor	Correction value
e	At emission
eff	Effective value

h	Frequency index
j	Scan plane grid point index
k	Sound source index
l	Sound source index
m	Microphone index
max	Maximum value
$model$	Modelled parameter
$meas$	Measured parameter
r	Population member index
rec	At receiver
u	Parameter index
0	Reference location
O	Microphone array centre

Superscript

$*$	Complex conjugate transpose

List of Abbreviations

ADS-B Automatic Dependent Surveillance - Broadcast

ANOPP Aircraft Noise Prediction Program

BF Beamforming

BPF Blade Passing Frequency

CB Conventional Beamforming

CSM Cross Spectral Matrix

DAQ Data Acquisition System

DE Differential Evolution

DEMO Electronic and Mechanical Support Division of Delft University of Technology

EPNL Effective Perceived Noise Level

FB Functional Beamforming

FDR Flight Data Recordings

FFT Fast Fourier Transform

GO Global Optimisation

HF High Frequency

ILS Instrument Landing System

KNMI Royal Netherlands Meteorological Institute

LF Low Frequency

MC Measurement Campaign

MLG Main Landing Gear

NASA National Aeronautics and Space Administration

NLG Nose Landing Gear

PSD Power Spectral Density

PSF Point Spread Function

RMS Root Mean Square

RPM Revolutions Per Minute

SNR Signal-to-Noise Ratio

SPL Sound Pressure Level

1

Introduction

The aviation sector faced a tremendous air traffic growth of 6.5% per year on average the past 5 years, resulting in concerns about the sustainability of the current and expected growth [1, 2]. The concerns focus on climate and noise effects, where in this research the focus is placed on aircraft noise emissions. Noise nuisance from aircraft movements is said to cause hypertension, coronary artery disease, annoyance, sleep disturbance, hearing impairment, and decreased performance in the neighbourhoods surrounding an airport [3, 4]. These health impacts caused stricter noise regulations for airports, drawn up by the European Commission in project 'Flightpath 2050'. The goal is a reduction of 15 EPNdB in effective perceived noise level per operation by the year 2050 with respect to the new generation of aircraft in 2000 [5].

In order to reduce noise, the noise source should be known. Literature already indicates potential aircraft noise sources. These can be divided in two groups: airframe and engine noise. Airframe noise covers noise from landing gear, high-lift devices, and wing noise. Engine noise encompasses noise from the engine components such as the fan, core, and jet exhaust. Besides these groups, also installation noise from interference between two sources is named in literature [6]. There are two approaches to gather knowledge on noise sources: modelling and measurements. In this research the focus is applied on measurements. Currently, most research on aircraft noise sources is invested in measurements on landing aircraft [7–9]. Landings are easier to measure than take-offs as they always follow the same flight path due to a similar touch-down location on the runway. Also during landing the engines are turning idle, thus engine noise is not overpowering the airframe sources. But ideally also a better understanding of noise sources in take-off is needed. This understanding can be achieved by acoustic imaging of fly-over noise measurements.

Acoustic imaging is a technique to identify and visualise noise sources. Through measurements with microphone arrays and applying a so-called acoustic imaging technique to the acoustic data, the source location and source strength can be determined and displayed in an acoustic source map. The best-known and most robust imaging method is Conventional Beamforming (CB). Although robust, this method involves an extensive search for source locations over a scanning grid. Moreover, this method has a limited spatial resolution, preventing the imaging of closely spaced noise sources. CB also has high noise levels where no source is present (high levels of grating and side lobes). Over the years, a multitude of research was invested in a vast range of acoustic imaging methods which should overcome these limitations. The majority of these methods are deconvolution methods, which post-process the CB results. There is however one very promising method which is not based on post-processing the CB results but rather solves an inversion problem. This method is Global Optimisation (GO). Studies have proven that GO is able to escape the local optima, i.e. side lobes, and is able to find sources below the spatial resolution limit of CB [10, 11]. GO is potentially able to find multiple sound sources in 3D space, eliminating the need of a 2D scan plane.

1.1. Research objective

The objective of this research is to assess the use of GO as imaging method to localise and quantify acoustic sources on real fly-over data. The assessment is done by applying the GO algorithm to an experimental data set recorded in an anechoic room, to simulated fly-over data, and lastly to experimental data of aircraft fly-overs. The results are compared to CB and Functional Beamforming (FB) source maps. The FB method is similar to CB, but often turns out to be capable of severely diminishing side lobes. An experimental data set consisting of both landing and take-off fly-over measurements will be collected at Amsterdam Airport Schiphol. GO will be tested on a landing and on a take-off measurement to conclude if GO is able to find the aircraft height (omitting the need of Automatic Dependent Surveillance - Broadcast (ADS-B) data) and find sources under the Rayleigh limit.

1.2. Research structure

After this introduction, the data sets that are considered for the performance analysis of GO will be explained in Chapter 2. In that chapter phased microphone arrays are introduced for which the theory is presented in Chapter 3. With the measurement data set and the limitations in mind, the acoustic imaging techniques are introduced in Chapter 4. With these imaging techniques the analysis of the first data set is started. This is a data set from noise measurements in an anechioc room with three speakers at known locations. The results are presented in Chapter 5. The anechoic room experiment assesses the performance of GO in a controlled environment for a challenging application. After that, a simulation is performed for a fictitious aircraft in a take-off operational condition. The results of the analysis with the simulated data set are presented in Chapter 6. With the knowledge of the previous two chapters, the real aircraft fly-over data can be analysed with GO. However, first a basic analysis of the fly-over data is performed in Chapter 7. This basic analysis is to develop an understanding of the fly-over measurements. With this understanding, two fly-over measurements are analysed with GO in Chapter 8. Finally, the conclusions and recommendations following from this research are presented in Chapter 9.

2

Data sets used

This chapter explains the three data sets used to assess the performance of GO. Firstly, a data set in an anechoic room is discussed in Section 2.1. This data set is used as an extension to the knowledge from research by A. Malgoezar and D. Nijhof [10, 11]. Secondly, a simulated data set is considered in Section 2.2. This data set is used to investigate the effect of sources positioned in an aircraft configuration, which more closely resembles the complicated fly-over measurements on which GO is ultimately applied. Lastly, the acquisition of the fly-over measurement data set is explained in Section 2.3.

2.1. Indoor anechoic room measurements

On May 18, 2018, an experimental data set with three sources was gathered in the A-tunnel of Delft University of Technology. This data set has not been analysed before. The A-tunnel is an open-jet anechoic wind tunnel, however the flow stream was not used, thus effectively it is an anechoic room. All aspects of the measurements in the A-tunnel will be referred to as *indoor*. In the A-tunnel, three speakers were set up. First each speaker was measured separately to determine the individual frequency spectrum. After that all three were engaged. The x-, y-, and z-direction of the experiment in the anechoic room are shown in Figure 2.1. The set-up of the speakers is shown in Figure 2.2. The speakers are placed next to each other (x-direction), and are aligned in the y-direction. The speakers however have different distances to the array, reflected in the z-direction.

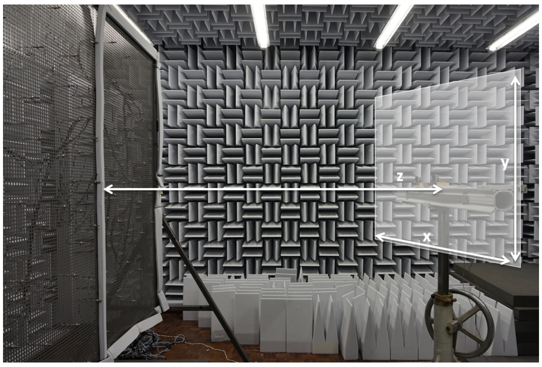

Figure 2.1: Alignment of the speakers with respect to the microphone array in the anechoic room of the A-tunnel. The microphone array is the grid with microphones as visible on the left hand side. The speakers are placed in the white area on the right hand side. The distance z is defined between the speaker and the array. For simplicity, a single XY-plane is depicted here. In reality there are three XY-planes, one for every speaker.

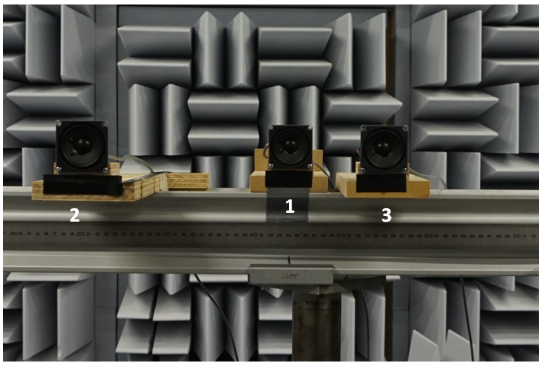

Figure 2.2: Alignment of the speakers on the x-axis. The speakers vary in x- and z-direction with respect to each other. The number of the speaker is added which relates to the parameters in Table 2.1. The right most speaker (3) is closest to the microphone array.

The locations of the speakers are indicated in Table 2.1. The speaker with the smallest z is located closest to the array.

Source	**1**	**2**	**3**
x **(m)**	0	-0.161	0.215
y **(m)**	0	0	0
z **(m)**	2.56	2.466	2.36

Table 2.1: Parameters of the three speaker sources arranged in the anechoic room. Each source is defined by a position in 3D-space with a x-, y-, and z-coordinate. The (x, y) point (0,0) is directly opposite of the microphone array centre. The source strength is determined in Chapter 5 from single speaker measurements.

The speakers broadcast white noise. The sound sources are measured with a microphone array containing 64 microphones in an optimised configuration. The array is optimised for a minimum side lobe level and a low main lobe width [12]. The microphones are mounted on a 2 by 2 m area of a vertical grid in the A-tunnel, see Figure 2.1. The aperture of the array is 1.9 m [12]. The configuration of the microphones is shown in Figure 2.3.

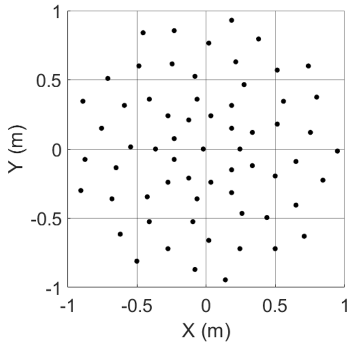

Figure 2.3: Optimised microphone array configuration as used in the A-tunnel measurements. The array contains 64 microphones. The array is optimised for minimum side lobe levels and a minimum main lobe width.

The microphones are connected to a Data Acquisition System (DAQ) which records the digital signals at a sampling frequency of 50 kHz. The signal is recorded for 30 s over which the speaker output is constant. The measurements are started and stopped via Matlab which calls a Labview application.

2.2. Simulating aircraft fly-over measurements

The simulated aircraft fly-over measurements are based on the configuration of a Boeing 747-800. It represents this aircraft during take-off, as this is expected to result in the most complicated data set due to the large distance to the array (see also Section 3.3). Short after the runway it is expected that the noise of the four engines is dominant and that the nose landing gear might still be out and recognised separately from the engines. The source strengths belonging to these sources were taken from a measurement. See Table 2.2 for the parameters per source.

Source	**1**	**2**	**3**	**4**	**5**
x **(m)**	-21.82	-12.19	0	12.19	21.82
y **(m)**	0	-12.87	-27.3	-12.87	0
z **(m)**	250	250	245	250	250
s **(Pa)**	1.2	1.2	0.75	1.2	1.2
Line colour	blue	orange	yellow	purple	green

Table 2.2: Location and source strength of the five simulated sources implemented in the simulated data set. Each source is defined by a position in 3D-space with a x-, y-, and z-coordinate and a corresponding source strength s. The source locations and strengths are derived from a fly-over measurement of a Boeing 747-800. The indication of line colour per source, in the last row, is used to analyse the convergence plots in the following sections.

The simulated data set will be used in combination with the Underbrink array described in Section 2.3. The use of this microphone array represents the fly-over measurements case the best.

2.3. Outdoor fly-over experiments

For the measurements of aircraft fly-overs, referred to as *outdoor*, not only the array is important, but also the environmental conditions and location with respect to the aircraft play a role in the success of the experiment. Next to that, in outdoor measurements the source position and strength is not known in contrary to the two previous data sets. Therefore, two supplementary systems to generate more knowledge on the measurements are discussed. These are the optical camera in the array and the ADS-B receiver. The total system is called an acoustic camera. On a separate laptop an Excel file is kept in which the flight number, registration code, time stamp, and aircraft type are registered for every measurement. This allows for easy tracking of the aircraft later. First the acoustic camera and its subsystems are discussed in Section 2.3.1. After this, the location and weather conditions required for the measurements are discussed in Section 2.3.2 and 2.3.3 respectively. An overview of all measurements can be found in Appendix A.

2.3.1. Outdoor microphone array

The microphone array contains 64 microphones, bundled and spread over 8 spiral arms. The microphones are placed in an Underbrink spiral configuration. The Underbrink configuration places microphones on log-spiral arms causing a higher density of microphones in the middle of the array. This configuration is able to perform well over a broad frequency range in terms of maximum side lobe levels and array resolution, i.e. the ability to resolve closely space sources. Moreover, it is able to analyse far-field (plane wave) as well as near-field (spherical wave) with high resolution [13, 14].

The microphones are mounted on a 4 by 4 m area of wooden plates. The plates are covered with sound absorbent foam to prevent any reflections from the plates. To reduce ground reflection effects on the edges of the array, the outermost microphones are placed 30 cm from the edges. The aperture of the array thus is 3.4 m. Lastly, for outdoor measurements wind shields are placed over the microphones.

The array during operation in the field is shown in Figure 2.4a. The configuration of the microphones is shown in Figure 2.4b.

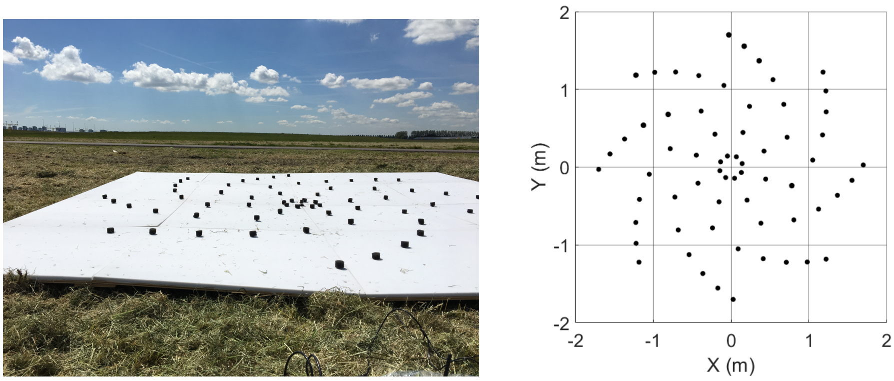

(a) The fully set-up microphone array from the acoustic camera, placed in the field at Amsterdam Airport Schiphol.

(b) Microphone array configuration as used in the outdoor fly-over measurements. Note that this view is from below, looking upward towards the fly-over.

Figure 2.4: Microphone array as used for fly-over noise measurements. The array is designed by a student of Delft University of Technology. The array contains 64 microphones, spread over 8 log-spiral arms. This is the Underbrink configuration which works well over a broadband frequency range [13].

The microphones are connected to the DAQ which records the analog signal and converts this to a digital signal at a sampling frequency of 50 kHz. For outdoor measurements four DAQs are available. In this case DAQ Camera 2 was used for all Measurement Campaigns (MCs).

The DAQ is connected to a laptop which contains a Labview application to direct the DAQ. The Labview application can start and stop a measurement, save the data, and show the real-time microphone data as well as a real-time spectrogram and beamforming image. This allows the user to quickly check the microphone output.

Both the DAQ and the microphones need to be calibrated properly before the start of a MC. The full calibration process is explained in Appendix B.

The optical camera in the centre of the array supports the analysis of the acoustic measurements in two ways. Firstly, the camera makes a video over the measurement time. Thus the overhead location of the aircraft can be determined with the optical camera. Secondly, a still of the video is laid over the acoustic source map to have a reference for the sources.

The optical camera is connected directly to the computer. Its videos are saved in a folder with the microphone measurements. In Labview, settings for the exposure time or camera gain can be altered, which allows for a clear video on sunny or cloudy days. On the optical camera itself, the focal length and contrast are arranged.

The ADS-B meter is connected to the laptop as well and from there the location, speed, and height data of every aircraft around Amsterdam Airport Schiphol is recorded. The ADS-B receiver collects information every second. However, often there are offsets in the aircraft sensors that feed the ADS-B data and therefore for these cases the height and aircraft speed are not properly transmitted. Sometimes, negative heights were found for aircraft flying over the array. Especially for measurements of take-offs potential height errors in the ADS-B pose a problem, as the aircraft all have their own flight path and do not follow the Instrument Landing System (ILS). During landing the aircraft follow the ILS which gives them approximately the same height and location above the array.

Therefore next to the Delft University of Technology receiver, also data from the Open Sky Network is used. This network is a community-based receiver network, with more than 2000 receivers around the world [15]. Preprocessed data per aircraft is available there which serves as good back-up for the receiver of the camera.

2.3.2. Measurement location

Over the course of this research, a data set of noise measurements of aircraft in landing or take-off operation was gathered. To make the results of landings and take-offs comparable, the location and equipment had to be the same during all MCs.

To provide the most accurate measurements, the aircraft should be as close as possible to the microphone array and there should be as little background noise as possible. These requirements translate to a measurement location next to the runway and away from busy roads. The runway lay-out of Amsterdam Airport Schiphol, where the measurements will be taken, is shown in Figure 2.5. An analysis showed that location 18C is the best candidate especially due to its close vicinity to the runway (only 670 m). See the exact location of the measurements in Figure 2.6.

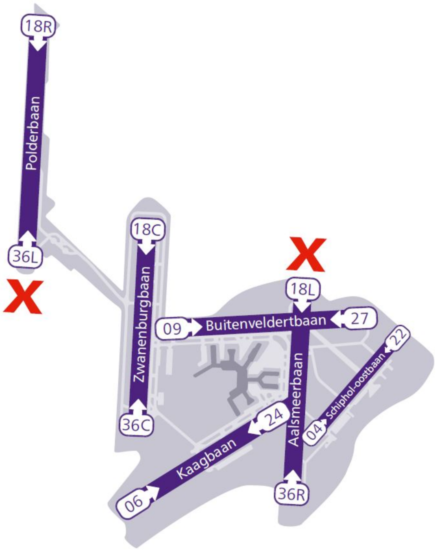

Figure 2.5: Runways at Amsterdam Airport Schiphol with the landing and take-off directions. The red cross indicates that in this direction no flight movements are allowed [16]. Location 18C was chosen for the outdoor measurements.

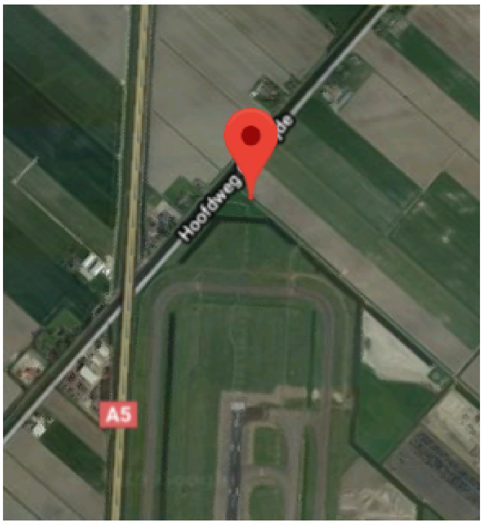

Figure 2.6: Exact location of the microphone array during all MCs at location 18C. The coordinates of the location are 52.337284 N, 4.740565 E.

2.3.3. Weather conditions

Northern wind is needed for aircraft passing over location 18C during take-off. For landing measurements at location 18C, Southern wind is needed. Apart from that, the temperature, air pressure, and humidity are logged to later calculate the atmospheric attenuation correction. The weather data is provided by the Royal Netherlands Meteorological Institute (KNMI) [17]. The wind speed is also logged and is used to check if it is still below the 4 Beaufort, serving as maximum for noise measurements. The weather conditions during all MCs are presented in Appendix A.

3

Limitations of microphone arrays

The microphone arrays introduced in Chapter 2 are phased microphone arrays. These make use of the fact that with a bundle of microphones more information on the sound source can be obtained than with a single microphone, due to different arrival times of an acoustic wave at microphones closer or further away from the source. An array of microphones provides the possibility to locate one or multiple sources and to quantify these separately [18]. The use of an array of microphones thus increases the Signal-to-Noise Ratio (SNR) and the spatial resolution of measurements compared to single microphone measurements [19].

The two most common challenges with microphone arrays are 1. to obtain sufficient spatial resolution and 2. to avoid spatial aliasing [20, 21]. These limitations are discussed in Section 3.1 and 3.2 respectively. Lastly, in this chapter the near-field limit of a microphone array is discussed in Section 3.3. This limit plays a role in the determination of the source location and is related to the array size.

To understand the first two limitations presented in this chapter, the Point Spread Function (PSF) is introduced. The PSF is the acoustic image obtained when a single source is present. Figure 3.1 shows the PSF. No beamsteering is applied, i.e., the signals on the individual microphones are summed and the resulting level (amplitude, effective pressure, or intensity) is displayed for all source positions in the grid. For this case, fully constructive interference only occurs with the source above the centre of the array. Alternatively, one can see the PSF as the beamsteering output with one source present directly above the array. Beamsteering, as treated in Chapter 4, where microphone dependent delays are applied, allows to focus the array to other locations. When analysing a single point source with a circular microphone array of finite aperture, the result is not an infinitesimally small point source. The source resembles a first order Bessel function, hence having a main lobe and several side lobes as shown schematically in Figure 3.1.

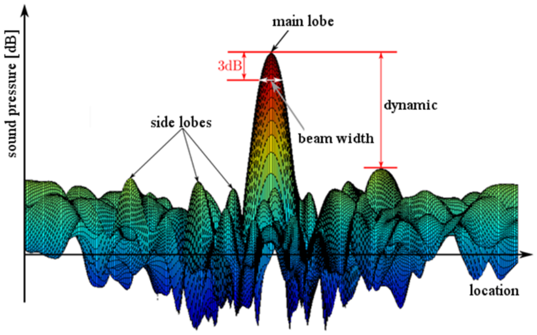

Figure 3.1: Schematic illustration of a PSF which represents the beam pattern of a point source [22]. Here also the main lobe and side lobes are indicated. The dynamic range is the difference in level between the main lobe and the highest side lobe. The beam width is the size of the main lobe 3 dB below its maximum [22]. The source is located at the maximum of the main lobe.

The main lobe width can be reduced by increasing the aperture of the array. Also, when applying beamforming at higher frequencies, the main lobe width reduces. Typically, the abundance of side lobes can be reduced by increasing the number of microphones. Neither the aperture nor the number of microphones on the array used for this research can be altered. Therefore the resulting limitations are indicated in the following sections.

3.1. Spatial resolution

Spatial resolution defines the distance at which two closely spaced sources can still be discerned. Each point source is represented by its own PSF. When one source lies within the main lobe of the other source, the main lobes overlap and are seen as a single source. The limit at which the two sources are still separately visible, is called the Rayleigh limit or spatial resolution. The effect of spacing of two sound sources on the appearance of the two sources around the Rayleigh limit is schematically shown in Figure 3.2. Here the red line indicates the source levels depicted in the acoustic image.

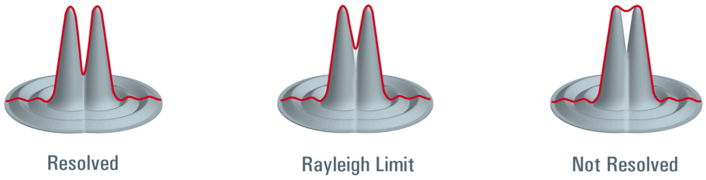

Figure 3.2: Two sources represented by their PSFs around the Rayleigh limit [23]. The red line indicates the value in a source map. On the left the sources are separated by more than the Rayleigh distance, thus separately visible. In the middle the sources are located at the Rayleigh distance and just separable. On the right the sources are located within the Rayleigh distance and hard to identify.

The main lobe width is thus a factor in this limit. This main lobe width is determined by the aperture of the array as well as the frequency of interest. The Rayleigh limit also depends on the location of the source, in perpendicular distance to the array. The Rayleigh limit is defined in Equation 3.1 [24].

$$R = 1.22\frac{ch}{Df} \tag{3.1}$$

R is the Rayleigh distance, c the speed of sound in air, h the distance between source and receiver (for the application considered in this literature study it is the height of the aircraft above the array), D the array aperture, and f the frequency of interest. When the height of the fly-over increases, R increases and thus the spatial resolution decreases. This is especially limiting for take-off fly-over measurements as take-offs pass over the array at higher altitudes.

For the outdoor array used in this report the Rayleigh limit over frequency is calculated as an example. The aperture D is 3.4 m, the speed of sound c is 343 m/s, and as example case an aircraft at a height of 250 m is taken. Figure 3.3 shows R as a function of frequency. A comparison is made with an aircraft at a height of 67 m as expected during landings [25]. Furthermore, for reference, two horizontal dashed lines have been added. The dashed line for the A380 represents the distance between one of the inner engines and the Main Landing Gear (MLG) [26]. The dashed line for the B747-800 represents the distance between the outer and inner engine [27]. If the Rayleigh limit is larger than the reference values, the sources cannot be distinguished.

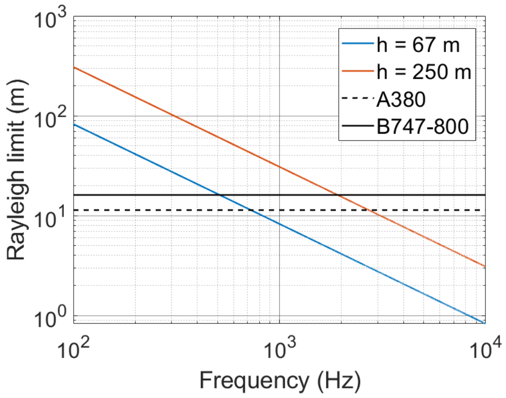

Figure 3.3: Rayleigh limit over frequency for the outdoor array, on a logarithmic scale. The blue line corresponds to the height of an aircraft fly-over during landing. The orange to a take-off. A reference of the shortest distance for the MLG and engines of the A380 is added. For a B747-800 this is done for the distance between the inner and outer engine.

3.2. Spatial aliasing

Spatial aliasing is the appearance of non-existing sources on the source map, reflected in the PSF. It is a result of (partial) constructive interference, where full interference at locations other than the source position is referred to as a grating lobe and partial interference is a side lobe [28]. In Figure 3.1 only side lobes are visible.

It is not possible to avoid side and grating lobes fully as they are a result of the finite number of microphones in an array [29]. However, grating lobes (spatial aliasing) can be reduced by placing the microphones closer together than half the wavelength of interest [19]. This eliminates the grating lobes. This requirement gives complications when high frequency sources (small wavelengths) are researched. This would imply microphones spaced extremely close together. For example, analysing frequencies up to 9500 Hz as is done in [30] requires a microphone spacing of 18 mm for a linear array which is difficult to manufacture.

This section in combination with the previous section poses two conflicting requirements for an array with a set number of microphones to be used on a broad frequency range. To avoid grating lobes at high frequencies, the microphones should be placed closely together. However, to increase spatial resolution at low frequencies the aperture should be as large as possible and thus the microphones should be spaced far apart. This conflict is partially resolved by using irregular spacing of microphones through a spiral configuration [13].

3.3. Fresnel distance

A microphone array has a near-field and far-field for which the boundary is specified by the Fresnel distance. If a source is located under the Fresnel distance, it is in the near-field and the acoustic wave cannot be assumed to be a plane wave. Above the Fresnel distance, the source is in the far-field and the acoustic wave can be considered to arrive on the array as a plane wave, i.e. the curvature of the wave front can be neglected. It is important to know whether sources are in the near-field or far-field when analysing them with an imaging technique. A reason is that for sources in the far-field typically only the direction from which the sound is coming, can be determined. For sources in the near-field, the three-dimensional source location affects the phase delay pattern. In Figure 3.4 a schematic illustration of the spherical and planar wave arriving at the array is made.

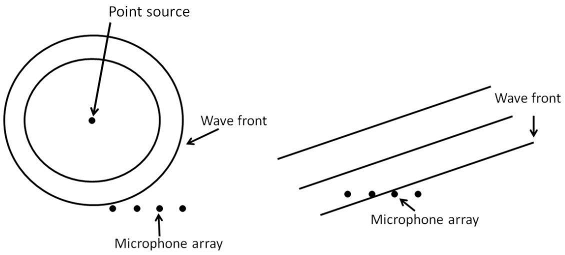

Figure 3.4: Schematic illustration of a spherical wave (left) and a plane wave (right) impinging on a microphone array. For the plane wave the point source lies very far away to the left upper corner of the page. The microphone array here is visible as line array, but could also be an array spreading in x- and y-direction as seen in Chapter 2.

When the acoustic source is in the near-field, the time delays over the microphone array are defined by the x-, y-, and z-location of the source. In this case the z-location has a large influence on the time delay pattern over the array. However, when the radius of the sphere is large, i.e. when the source is far away, with respect to the microphone array this is perceived as a plane wave. No matter how far away the source is, the wave will arrive on the array as a plane. It will thus cause the same phase delay pattern over the array. The direction of the source can still be found by the phase delay pattern. However, the source height can hardly be determined.

The boundary between near-field and far-field is described by the Fresnel distance. The Fresnel distance is specified as r_F and depends on the array size and the wavelength of a signal. D is the receiving array length, thus the aperture of the array. λ is the wavelength of the signal and is defined as $\lambda = \frac{c}{f}$. Equation 3.2 shows the Fresnel distance.

$$r_F = \frac{fD^2}{c} \tag{3.2}$$

The Fresnel distance for the indoor and outdoor array with respect to frequency is shown in Figure 3.5. The array aperture D is 1.9 m for the indoor array and 3.4 m for the outdoor array and the speed of sound c equals 343 m/s. To give an indication of the Fresnel distance for the data sets considered, examples follow here. Keep in mind that if the Fresnel distance is larger than the distance from the array to the source, the source is in the near-field.

The indoor microphone array is analysed from 50 Hz up to and including 5950 Hz. At 50 Hz the r_F equals 0.53 m, hence the sources are in the far-field, but for 250 Hz r_F equals 2.63 m. Thus for the largest part of the analysis the speakers are in the near-field as they are located around 2.5 m from the array. Outdoor measurements are often examined at frequencies around 2500 Hz, 5500 Hz, or 7500 Hz. For measurements with the outdoor microphone array at these frequencies r_F equals 84.3, 185.4, and 252.8 m respectively. This means that for landings, which are on average at 67 m height [25], the sources are always in the near-field. However, take-offs from the experiments are well above 200 m and are thus for most analysis in the far-field. This last part on outdoor measurements is shown visually in Figure 3.5 by the horizontal dashed lines representing the height of a take-off (at 250 m) and a landing (at 67 m).

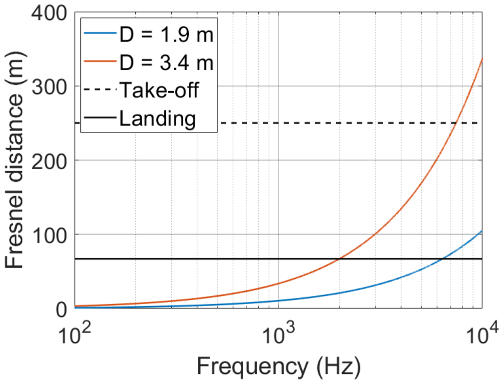

Figure 3.5: Dependency of the Fresnel distance on frequency (on logarithmic scale). The blue line indicates the Fresnel distance for the indoor microphone array with $D = 1.9$ m. The orange line indicates the Fresnel distance for the outdoor microphone array with $D = 3.4$ m. The horizontal dashed lines represent the distance from the array to the aircraft for a landing (at 67 m) and a take-off (at 250 m).

4

Imaging techniques

As introduced earlier, with phased microphone arrays it is possible to locate and quantify sound sources, a process called imaging. The basis of most imaging techniques is Conventional Beamforming (CB). A general introduction to beamforming is given in Section 4.1. Due to the limitations of CB many other imaging methods have been developed. Here two other methods are selected to be further explained, but first the principle of beamforming and the full mathematical explanation of CB is given in Section 4.2, as this provides a good basis for understanding the other techniques. After that Functional Beamforming (FB) is explained in Section 4.3. Lastly, Global Optimisation (GO) is explained in Section 4.4.

4.1. Beamforming

Beamforming is the most widely practised imaging technique to identify a sound source in both location and strength. It is based on differences in the arrival times of signals between microphones. One can imagine that the sound wave arrives first and strongest at the closest microphone. Microphones further away will receive the signal later and at lower amplitudes due to propagation losses. The difference in arrival times is exploited in beamforming. For aircraft fly-overs it works as follows: a scan grid is defined at the height of the aircraft, then for each grid point the propagation time to a microphone on the array is calculated. The individual microphone signals are corrected for the so-called delay times and subsequently the signals are summed over the microphones per grid point. When a sound source is present at the grid point analysed, the delayed signals have constructive interference and a source becomes apparent. Through this a source image is produced, which shows the sound sources. Although beamforming can be done in time and frequency domain, for this purpose the frequency domain is chosen. The reason for this is the ability to analyse sources per frequency band, which gives more detail on the origin of the noise. Moreover beamforming in the frequency domain is computationally more efficient [31].

4.2. Conventional Beamforming (CB)

CB is the most widely applied version of beamforming for (aero)acoustic measurements due to its simplicity and robustness. It is the basis of most imaging methods and is explained in detail here.

In CB the sound source is described as a monopole source. This implies that the acoustic pressure for a specific microphone m is as stated in Equation 4.1.

$$p_0(t) = \frac{r_m}{r_0} p_m(t + \Delta t_m) \tag{4.1}$$

p_0 is the acoustic pressure at a reference distance of $r_0 = 1$ m. t is the time. r_m is the distance from the source to the microphone with p_m the measured acoustic pressure at the microphone. In Equation 4.1, Δt_m is the delay time from the source to a specific microphone for which the equation is given in Equation 4.2.

$$\Delta t_m = (t_{rec} - t_e) = \frac{r_m}{c} \tag{4.2}$$

In the time delay formula, t_{rec} is the receiver time and t_e the emission time.

In the frequency domain, Equation 4.1 becomes Equation 4.3. The transfer to the frequency domain is done with a Fourier Transform.

$$P_0(f) = \frac{r_m}{r_0} P_m(f) e^{2\pi i f \Delta t_m} \tag{4.3}$$

P_0 and P_m are the Fourier transforms of the pressures. P_0 is the acoustic pressure at the source and is unknown. P_m is the acoustic pressure as measured at the microphone. By rewriting Equation 4.3 and introducing the steering vector element g_m, one gets Equation 4.4.

$$\begin{aligned} P_m(f) &= P_0(f) \left(\frac{r_0}{r_m} e^{-2\pi i f \Delta t_m} \right) \\ &= P_0(f) g_m(f) \end{aligned} \tag{4.4}$$

This function of P_m expressed in P_0, can be split in the acoustic pressure at the source, P_0, and a so-called steering vector, containing g_m for all microphones. A steering vector is a vector containing the phase shifts corresponding to the distance between the source position and receiver locations.

In beamforming, the aim is to find source locations and strengths (thus find P_0). This is done by finding that source strength and location that results in a maximum match between the modelled and measured pressures [29]. This match is quantified through a cost function J evaluated at the microphone level, see Equation 4.5.

$$J = \|\boldsymbol{P} - P_0(f)\boldsymbol{g}\|^2 \tag{4.5}$$

In Equation 4.5 all measured acoustic pressures are united in vector $\boldsymbol{P}$, and all microphone steering vector elements (g_m) are united in vector $\boldsymbol{g}$. A maximum match is obtained when J reaches a minimum at $J = 0$. The cost function is minimised in a least-squares manner, for which the solution is given in Equation 4.6.

$$\hat{P}_0(f) = \frac{\boldsymbol{g}^* \boldsymbol{P}}{\|\boldsymbol{g}\|^2} \tag{4.6}$$

In Equation 4.6 the asterisk (*) denotes the complex conjugate transpose and $\hat{P}_0$ is the least-squares amplitude estimate of the acoustic pressure at the location steered at. However, it is more useful to represent source auto-powers as these are reflected in the Sound Pressure Level (SPL).

The source auto-power A for CB is computed by making use of Equation 4.6 and the fact that the effective pressure is the Root Mean Square (RMS) value of $P_0(f)$.

$$A = p_{eff}^2 = \frac{1}{2}|\hat{P}_0(f)|^2 = \frac{1}{2}\hat{P}_0(f)\hat{P}_0^*(f) \tag{4.7}$$

Combining Equation 4.6 and 4.7, gives Equation 4.8.

$$A(f) = \frac{1}{2}\frac{\boldsymbol{g}^*\boldsymbol{P}}{\|\boldsymbol{g}\|^2}\left(\frac{\boldsymbol{g}^*\boldsymbol{P}}{\|\boldsymbol{g}\|^2}\right)^* = \frac{1}{2}\frac{\boldsymbol{g}^*\boldsymbol{P}\boldsymbol{P}^*\boldsymbol{g}}{\|\boldsymbol{g}\|^4} = \boldsymbol{w}^*\boldsymbol{C}\boldsymbol{w} \tag{4.8}$$

Equation 4.8 shows the CB definition with weight vector $\boldsymbol{w}$ and covariance matrix (also called CSM) $\boldsymbol{C}$ after the last equal sign. Here, $\boldsymbol{w}$ equals $\frac{\boldsymbol{g}}{\|\boldsymbol{g}\|^2}$ and $\boldsymbol{C}$ equals $\frac{1}{2}\boldsymbol{P}\boldsymbol{P}^*$. When $\boldsymbol{P}$ is described to be the result of a source of strength s_k at location $\boldsymbol{\xi}_k$ such that $\boldsymbol{P} = s_k\boldsymbol{g}_k$, then $\boldsymbol{C}$ equals $\frac{1}{2}s_k\boldsymbol{g}_k\boldsymbol{g}_k^*s_k = \frac{1}{2}s_k^2\boldsymbol{g}_k\boldsymbol{g}_k^*$. Using Equation 4.8 and steering this at $\boldsymbol{\xi}_k$ results in $A(f) = \frac{1}{2}s_k^2$.

Through this derivation, the source auto-power, thus source strength, is found at a predetermined location. As the source location is usually unknown, the auto-power is calculated at a range of possible source locations. For fly-overs this alleged scan plane is located at the aircraft height with a sufficient span in x- and y-direction to capture the length and span of the aircraft. A grid is applied to this scan plane and the auto-power is computed at each grid point j with coordinates $\boldsymbol{\xi}_j$. The steering vector element following from Equation 4.4 thus develops into $g_m(\boldsymbol{\xi}_j, f)$, a function of $\boldsymbol{\xi}_j$ through $r_m = \|\boldsymbol{x}_{m,O} - \boldsymbol{\xi}_j\|$. $\boldsymbol{x}_{m,O}$ is the microphone position with respect to the centre of the microphone array. Likewise, A becomes a function of grid point $\boldsymbol{\xi}_j$ and frequency f.

Eventually calculating $A(\boldsymbol{\xi}_j, f)$ for the whole scan plane gives the source plot of the sound sources at frequency f. However, CB suffers from low spatial resolution at low frequencies and high spatial aliasing at

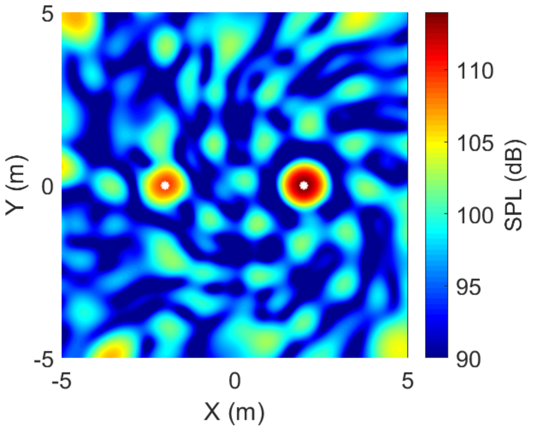

Figure 4.1: Acoustic source map made with CB of two point sources at a frequency of 2000 Hz. The white stars indicate the point source locations at (-2, 0, 10) and (2, 0, 10) with SPLs of 106.5 and 111 dB respectively. The colour represents the SPL with values as indicated by the colourbar. The source on the left can still be recognised, although it might be confused for a side lobe when the source strength is lower.

high frequencies. Both effects can be counteracted by summation of the source map over several frequencies ($h = 1, ..., N_{freq}$), which preserves the good resolution and eliminates side and grating lobes occurring at a single frequency. This summation is called incoherent summation. Incoherent summation is applied as follows in Equation 4.9.

$$A_{incoh}(\boldsymbol{\xi}_j) = \frac{1}{N_{freq}} \sum_{h=1}^{N_{freq}} A(\boldsymbol{\xi}_j, f_h) \tag{4.9}$$

The CB results are converted to SPL levels and corrected for aircraft height and atmospheric attenuation α, see Equation 4.10. The attenuation correction is dependent on the frequency and the meteorological conditions and the equations to calculate α are shown in Appendix C.

$$SPL_{CB}(f) = 20log_{10}\left(\frac{\sqrt{A(\boldsymbol{\xi}_j, f)}}{p_{ref}}\right) + 20log_{10}(h_{aircraft}) + \alpha(f)\|\boldsymbol{\xi}_j\| \tag{4.10}$$

An example of an acoustic source map using CB in the frequency domain can be seen in Figure 4.1. Throughout this chapter the same example will be used, which is a simple simulation of two point sources at location (-2, 0, 10) and (2, 0, 10) at a frequency of 2000 Hz (i.e. no incoherent summation over frequencies). The sources have a source strength of 106.5 dB and 111 dB respectively. The high number of side lobes is clearly visible. For this case, the side lobes do not yet overpower fully the second source but one can imagine this happening.

4.3. Functional Beamforming (FB)

FB makes use of the standard CB algorithm, but adapts the Cross Spectral Matrix (CSM) to obtain a better spatial resolution and dynamic range thus giving a more clear source map. Instead of formulating the CSM as done in Equation 4.8, it is decomposed into its eigenvalues and written as in Equation 4.11. The eigenvectors u of $\boldsymbol{C}$ are the columns of $\boldsymbol{U}$, and $\boldsymbol{\Sigma}$ is a diagonal matrix containing the eigenvalues σ of $\boldsymbol{C}$.

$$\boldsymbol{C} = \boldsymbol{U}\boldsymbol{\Sigma}\boldsymbol{U}^* \tag{4.11}$$

On $\boldsymbol{C}$ the power function $\frac{1}{\nu}$ is now applied to form Equation 4.12 [32]. ν is the functional exponent that can be set by the researcher.

$$\boldsymbol{C}^{\frac{1}{\nu}} = \boldsymbol{U}\text{diag}\left(\sigma_1^{\frac{1}{\nu}}, ..., \sigma_N^{\frac{1}{\nu}}\right)\boldsymbol{U}^* \tag{4.12}$$

As the effect of the power should be counteracted in the full beamformer to calculate the real source strength, Equation 4.8 is adapted to Equation 4.13, where A_ν is the auto-power at a specific ν.

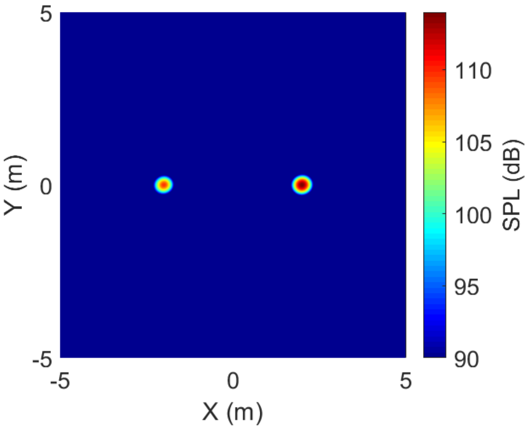

Figure 4.2: Acoustic source map made with FB of two point sources at a frequency of 2000 Hz. A functional exponent ν of 10 is applied. The two sources are clearly visible. The sources are located at (-2, 0, 10) and (2, 0, 10) with SPLs of 106.5 and 111 dB respectively. The colour represents the SPL with values as indicated by the colourbar, the same limits are used as in Figure 4.1.

$$A_\nu(\boldsymbol{\xi}_j) = \frac{1}{\|\boldsymbol{g}_j\|^2}\left(\frac{\boldsymbol{g}_j^* \boldsymbol{C}^{\frac{1}{\nu}} \boldsymbol{g}_j}{\|\boldsymbol{g}_j\|^2}\right)^\nu = \frac{1}{\|\boldsymbol{g}_j\|^2}\left(\frac{\boldsymbol{g}_j^* \boldsymbol{U}\boldsymbol{\Sigma}^{\frac{1}{\nu}}\boldsymbol{U}^* \boldsymbol{g}_j}{\|\boldsymbol{g}_j\|^2}\right)^\nu \tag{4.13}$$

With this equation, the source strength at the source location is found. Let us describe it as a source of strength s_k at location $\boldsymbol{\xi}_k$, such that $\boldsymbol{P} = s_k \boldsymbol{g}_k$ and $\boldsymbol{C} = \frac{1}{2}s_k^2 \boldsymbol{g}_k \boldsymbol{g}_k^*$. The main eigenvalue of $\boldsymbol{C}$ is $\sigma_1 = \frac{1}{2}s_k^2$ and the eigenvector is the steering vector to $\boldsymbol{\xi}_k$, so $\boldsymbol{u}_1 = \boldsymbol{g}_k$. If now the array is steered exactly at the source, $\boldsymbol{\xi}_j$ in Equation 4.13 becomes $\boldsymbol{\xi}_k$. Then the result for any ν is $A_\nu(\boldsymbol{\xi}_k) = \frac{1}{2}s_k^2$, the same as steering to the source in CB.

However when steering to another location than that of the source described before, say to $\boldsymbol{\xi}_l$, the beamform result becomes as shown in Equation 4.14.

$$A_\nu(\boldsymbol{\xi}_l) = \frac{1}{\|\boldsymbol{g}_l\|^2}\left(\frac{\boldsymbol{g}_l^* \boldsymbol{g}_k \left(\frac{1}{2}s_k^2\right)^{\frac{1}{\nu}} \boldsymbol{g}_k^* \boldsymbol{g}_l}{\|\boldsymbol{g}_l\|^2}\right)^\nu = \frac{1}{2}\frac{s_k^2}{\|\boldsymbol{g}_l\|^2}\left(\frac{\|\boldsymbol{g}_l^* \boldsymbol{g}_k\|}{\|\boldsymbol{g}_l\|}\right)^{2\nu} \tag{4.14}$$

It now becomes apparent that when the array is steered away from the source, the source strength is multiplied by a factor. $\|\boldsymbol{g}_l^* \boldsymbol{g}_k\|^{2\nu}$ represents the inner product of the steering vectors which accounts for the angle between the two steering vectors with a factor $cos(\theta)$ [32]. Therefore, when this is normalised, the source strength s_k^2 is always multiplied with a factor in between 0 and 1. This thus reduces the beamformer output outside of the source and this effect is intensified by applying a power of ν, thereby lowering extensively the output. For example, a side lobe of -3 dB analysed with FB at $\nu = 100$ becomes a side lobe of -300 dB. The source plot will thus be cleaned by using FB. When a power of $\nu = 1$ is applied, FB gives the CB results.

Note that for FB currently no model is available with incoherent summation over a frequency band. The method will thus only be applied to a specific frequency that is deemed interesting after analysing the spectrogram or frequency spectrum. However, the correction from Equation 4.10 is applied to FB as well.

The same example as shown for CB is shown for FB in Figure 4.2. It is not needed to indicate the sources with the white star as is done for the CB example, as the sources seen are exactly the sources present. It is clear that the side lobes are strongly suppressed with respect to the example of Figure 4.1.

For FB reductions in SPL are observed for higher values of functional exponent ν. This is caused by small differences between the grid point and the real source location. In literature this issue is dealt with by correcting the FB SPL levels with the difference between the maximum SPL of CB and FB [25]. This correction will be applied in this research as well.

4.4. Global Optimisation (GO)

CB and FB require a predefined scan grid (2D). This constrains the freedom of investigating different types of sound sources, which could be located outside of the grid. As imaging for different scan grids is tedious, GO was proposed and implemented in other knowledge areas such as geoacoustics and plants for industrial processes [33, 34]. Moreover it has been applied to place microphones in a microphone array, and it has been applied to a controlled set-up in an anechoic room [11, 35].

GO does not make use of any grid, merely of preset boundaries to the parameter space it searches in. It finds parameters by minimising an energy (or cost) function for several parameters in a global optimisation manner. When GO is seen as a replacement for other imaging methods, it should at least find the source location(s) and auto-power(s) as parameters. The algorithm works as follows.

In GO a 'trial' or candidate solution is fed into the energy function which calculates the error between the measured data and the candidate solution. By updating the candidate solution through a number of iterations the energy function is minimised. The possible methods for improving the candidate solution include simulated annealing, genetic algorithms, and ant colony algorithms. For anechoic room experiments with acoustic sources previously the Differential Evolution (DE) method from the group of genetic algorithms was used as GO algorithm [11] [36].

First the candidate is defined: a candidate contains possible values for the unknown parameters. Thus, for this application that would be coordinates (x, y, z) and source strength s. Considering one source a candidate becomes $\boldsymbol{m} = [x, y, z, s]$ containing 4 parameters. However, the expectation is that multiple sources are present, thus the candidate solution should be extended to the number of sources present. For three sources the candidate solution is $\boldsymbol{m} = [x_1, y_1, z_1, s_1, x_2, y_2, z_2, s_2, x_3, y_3, z_3, s_3]$. There is also a possibility to not only add extra sources, but extra unknown parameters such as air density or speed of sound. Now that a candidate solution is defined, the energy function to assess the goodness of this candidate should be defined. In this research two energy functions are tested. First E_{BF}, which is very similar to CB, and is explained in Section 4.4.1. Then E_{CSM}, which is solely based on CSM matching, is explained in Section 4.4.2. For the explanation of DE a general reference is made to *an energy function E* which could be either of the two.

The first candidate solution is randomly determined within preset boundaries, but to minimise the energy function the candidate solution has to be updated with DE. This is essentially following the Darwin Evolution Theorem in which natural selection takes place on the basis of how fit a species is. The new or updated candidate is a so-called descendant of current (original) population $\boldsymbol{m}$ and to create this descendant a partner population $\boldsymbol{s}$ is needed. A population exists of multiple members $\boldsymbol{m}$ and of an equal number of partners $\boldsymbol{s}$, thus the generation γ and population member r are used to indicate which $\boldsymbol{m}$ or $\boldsymbol{s}$ is meant. The partner population is created with Equation 4.15.

$$\boldsymbol{s}_{\gamma,r_1} = \boldsymbol{m}_{\gamma,r_2} + F(\boldsymbol{m}_{\gamma,r_3} - \boldsymbol{m}_{\gamma,r_4}) \tag{4.15}$$

The partner population is made from the same generation γ but from different members r which are mutually exclusive with the current population member index. Multiplication factor F can be set by the researcher anywhere between 0 and 1 which is proven to function most optimal [36].

A descendant from the current population with the partner population is found by crossover per parameter between a set of members from the same generation. There are different types of crossover like single-point crossover, two-point crossover, uniform crossover, or exponential crossover [37]. Uniform crossover has been used in aeroacoustic implementations [11, 35]. It is applied by comparing a uniform distribution realisation b to a predefined probability p_c lying between 0 and 1. The descendant population is constructed as in Equation 4.16. Index u indicates which unknown parameter is considered.

$$\boldsymbol{d}_{\gamma,r,u} = \begin{cases} \boldsymbol{m}_{\gamma,r,u} \text{ if } b \geq p_c \\ \boldsymbol{s}_{\gamma,r,u} \text{ if } b < p_c \end{cases} \tag{4.16}$$

The descendants are now assessed by the energy function. When a descendant has a lower energy compared to the original population member $\boldsymbol{m}_{\gamma,r}$, its solution flows into the next generation. When a descendant has a higher energy, it is not suitable and is replaced by the current (original) population member. This is shown in Equation 4.17.

$$\boldsymbol{m}_{\gamma+1,r} = \begin{cases} \boldsymbol{d}_{\gamma,r} \text{ if } E(\boldsymbol{d}_{\gamma,r}) < E(\boldsymbol{m}_{\gamma,r}) \\ \boldsymbol{m}_{\gamma,r} \text{ if } E(\boldsymbol{d}_{\gamma,r}) \geq E(\boldsymbol{m}_{\gamma,r}) \end{cases} \tag{4.17}$$

This process is repeated for a number of generations N_{gen}, after which full reruns are done to obtain independent runs. The outcomes are used to assess the energy landscape, in particular the existence of local optima. The number of independent runs is N_{runs}. N_{gen} and N_{runs} are setting parameters that are set by the researcher, just as the population size q, partner population factor F, and crossover probability p_c. Optimal values can be found through a sensitivity analysis where the convergence is analysed. Especially F and p_c are adapted then. As when F is smaller, the search space is less explored. When p_c is smaller, then combinations of promising parameter values are less exploited.

Now the theory of DE as GO method has been presented, there is one more complication to solve which is the number of unknown parameters given to a population member. For the cases considered in this research the number of unknown parameters is based on the number of sound sources in the volume to be analysed, as each source needs four parameters (x, y, z, s). For a simulation or experiment under known conditions, this is easy to specify. However, for measurements on aircraft fly-overs the number of sources is unknown. It could be guessed from a CB source map, or the NASA prediction model Aircraft Noise Prediction Program (ANOPP) could be used to count the number of sources at a specified frequency. Another option is to run the algorithm several times for different numbers of sources, each time increasing the number of sources starting by the number of non-zero eigenvalues of the CSM [20]. From here on, DE as method for GO is referred to as GO.

Again, to develop an idea of the results of GO the same example as presented for CB and FB, is presented in Figure 4.3. A single frequency analysis has been done with the CSM energy function. F is set to 0.4, p_c is set to 0.75, N_{gen} equals 1000, and N_{runs} equals 10. The boundaries are set from -5 to 5 m for the x-direction and y-direction, 5 to 15 m for the z-direction, and 0 to 2 Pa for the source strength s. In Figure 4.3a the value of the energy of the best solution is shown over the generations for all runs. All runs show the same behaviour in which the energy decreases over the generations, meaning that the CSM as modelled from the candidate solution is increasingly matching with the CSM as "measured". The other four convergence plots show only the convergence of a parameter for the best run where the same type parameter (so e.g. x) is grouped. Clearly within 200 generations the algorithm finds the locations and source strength correctly. Note that for the source strength the values are not expressed in SPL, but in the effective pressures.

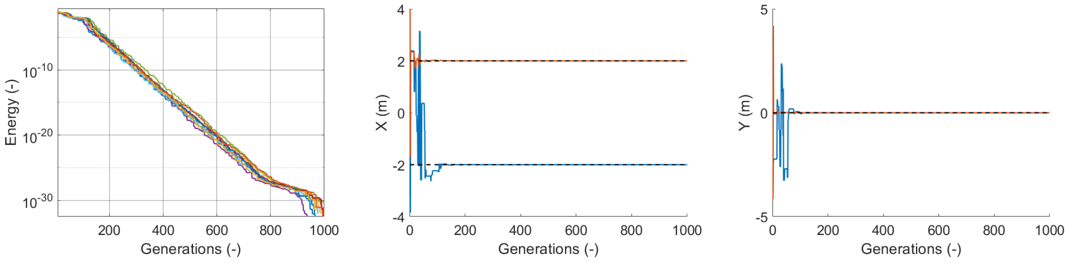

(a) Convergence for the energy.

(b) Convergence for the x-direction.

(c) Convergence for the y-direction.

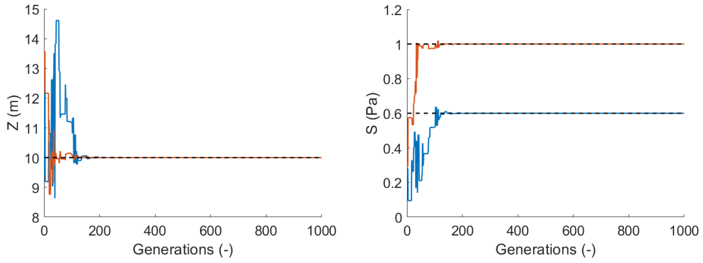

(d) Convergence for the z-direction.

(e) Convergence for the source strength.

Figure 4.3: Energy and convergence plots over generations of GO with the CSM energy function for $f = 2000$ Hz, searching two point sources (as in previous examples). A clear trend can be seen in the energy plot, where the energy reduces every generation. In the other convergence plots the black dashed line indicates the real parameter value. The blue and orange line indicate the value for the best member over the generations. Convergence is achieved in 200 generations.

4.4.1. Energy function based on phase matching

The energy function considered in this section works similar to CB and is therefore denoted as E_{BF}; it steers at a location (x, y, z) and calculates the acoustic energy at that location by applying Equation 4.8. If the steering location differs from the source location, the acoustic energy is reduced as explained with Equation 4.14.

Thus, by trying source locations, a maximum energy can be found which is where the source is located. When the candidate solution is at the actual source location, the source strength can be found through applying CB (see Equation 4.8). Hence, the parameters in the candidate member collapse from (x, y, z, s) to (x, y, z), reducing computational time.

The energy function that is implemented according to this theory is represented in Equation 4.18. As the steering vector is constructed per source location, the energy is summed for all sources (indicated by k). As the candidate location is closer to the source location, the match between modelled and measured phases maximises, but the energy function minimises by taking the negative energy.

$$E_{BF}(\boldsymbol{m}, f) = -\sum_{k} \frac{\boldsymbol{g}_k(\boldsymbol{m}, f)^* \boldsymbol{C}_{meas}(f) \boldsymbol{g}_k(\boldsymbol{m}, f)}{\|\boldsymbol{g}_k(\boldsymbol{m}, f)\|^2} \tag{4.18}$$

As can be seen by comparison to Equation 4.14, in the energy function a normalisation of $\|\boldsymbol{g}(\boldsymbol{m}, f)\|^2$ is implemented instead of a normalisation of the steering vector to power 4. The reason for this is that the power 4 introduces a factor including the distance to the source squared.

If only the effect of $\frac{1}{r}$ from the steering vector element g_m is considered, the auto-power scales with $\frac{1}{r^2}$ over $\frac{1}{r^4}$ i.e. r^2. This means that $A(\boldsymbol{m}, f)$ increases with r^2. This however does not quantify at all the match between the modelled and measured phase. This is artificially increasing $A(\boldsymbol{m}, f)$ for grid positions far away.

Reflecting back on the BF energy function, E_{BF} will achieve a lower energy for a distance further away, hence steer even further away, although that might be an incorrect location. This mainly happens in the z-direction causing the algorithm to find sources at too distant locations. To avoid the distance squared factor, the energy function has a normalisation of $\|\boldsymbol{g}(\boldsymbol{m}, f)\|^2$.

The advantage of this energy function is that it has fewer parameters to search for, which reduces the computational time. A potential disadvantage is that the acoustic energy around a source might be higher than the maximum acoustic energy of a weaker source elsewhere. In this case, the energy function finds only sources around the strongest source. Moreover this energy function is expected to suffer from the same disadvantage as CB with low spatial resolution at low frequencies, thus an inability to find sources under the Rayleigh limit.

4.4.2. CSM-based energy function

The CSM energy function makes use of the CSM from the measured data at a specific frequency f and the modelled CSM. The measured CSM is found by applying $\boldsymbol{C} = \frac{1}{2}\boldsymbol{P}(f)\boldsymbol{P}(f)^*$. The modelled CSM is constructed with a steering vector $\boldsymbol{g}_k$ towards the (x, y, z) of the candidate solution $\boldsymbol{m}$ and the auto-power s_k of the candidate solution as $\boldsymbol{C}_{model} = \boldsymbol{g}_k \frac{1}{2} s_k^2 \boldsymbol{g}_k^*$. This is constructed per source in the candidate solution and then summed to get a CSM which includes all sources.

The energy function is given in Equation 4.19. This represents the difference between the modelled CSM and measured CSM, and thus the result of this function should be minimised.

$$E_{CSM}(\boldsymbol{m}, f) = \sum_{\text{elements of CSM}} |\boldsymbol{C}_{model}(\boldsymbol{m}, f) - \boldsymbol{C}_{meas}(f)|^2 \tag{4.19}$$

An advantage of this method, is that it optimises in three dimensions and for source strength at the same time. However, the higher number of parameters results in a longer computational run time. From literature it is expected that this method is able to find sources below the Rayleigh limit [10].

4.4.3. Incoherent summation in GO

It is expected that the use of incoherent summation in the energy functions supports the ability to escape a local optimum (side lobe). A local optimum may exist at only one frequency and thus averaging over frequencies where it is not an optimum, will penalise a local optimum candidate solution. Similar to the implementation at CB, for the CB-based energy function the energy is averaged over the frequencies as is shown in Equation 4.20. For the CSM-based energy function the difference in modelled and measured CSM is calculated per frequency, after which the average over the frequencies is calculated. See Equation 4.21.

$$E_{BF,incoh}(\boldsymbol{m}) = -\frac{1}{N_{freq}} \sum_{h=1}^{N_{freq}} \left(\sum_{k} \frac{\boldsymbol{g}_k(\boldsymbol{m}, f_h)^* \boldsymbol{C}_{meas}(f_h) \boldsymbol{g}_k(\boldsymbol{m}, f_h)}{\|\boldsymbol{g}_k(\boldsymbol{m}, f_h)\|^2} \right) \tag{4.20}$$

$$E_{CSM,incoh}(\boldsymbol{m}) = \frac{1}{N_{freq}} \sum_{h=1}^{N_{freq}} \left(\sum_{\text{elements of CSM}} |\boldsymbol{C}_{model}(\boldsymbol{m}, f_h) - \boldsymbol{C}_{meas}(f_h)|^2 \right) \tag{4.21}$$

5

Performance of GO on anechoic room data

The goal of this chapter is to find out whether GO is capable of finding sources at different z-locations. This would further prove the ability of GO to find sources in 3D space. This is advantageous for aircraft fly-over measurements where the extended landing gear and engines are not at the same height with respect to the array, or where the aircraft height is unknown. At the same time this data set allows for a further analysis of the performance of GO under the Rayleigh limit.

Firstly, the CB source map of the experiment is shown in Figure 5.1. As the frequency spectrum of the speaker is expected to be constant over time, a signal snapshot of 3 s is used which is subdivided into 150 snapshots which are averaged in the CSM. Thus, the frequency resolution is 50 Hz. For the source map a frequency band of 3000 to 5000 Hz was selected. A different experiment with the same speakers with white noise showed the highest output for these frequencies [12]. The source map is made at a single scan plane for which the largest distance from the array to the speakers is chosen. In the source map, sources 1 (middle) and 2 (left) are just separable. It is clearly visible that there is a low side lobe level as is expected with the optimised array and the averaging over frequency. Note that speaker 2 is the weakest speaker in terms of SPL.

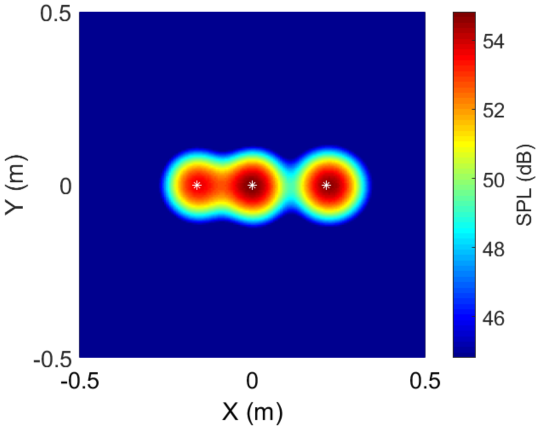

Figure 5.1: CB source map of the three speakers in the anechoic room on a frequency range of 3000 to 5000 Hz. As CB needs a scan plane at a certain distance from the array, a distance of 2.56 m (to the furthest speaker) is used. Source 2 (left) appears the weakest and is just separable from source 1 (middle). Source 3 (right) is closest to the array.

To analyse this data set, GO in combination with the single frequency CSM energy function is used as previous research indicated that this energy function is able to locate sources, at the same z-location, under the Rayleigh limit [10]. Therefore, the ability of this algorithm to find sources under the Rayleigh limit is now tested on sources at different z-locations as this might disturb the convergence of the algorithm. The analysis is done for a large number of frequencies starting at 50 Hz, ending at 5950 Hz in steps of 50 Hz. For the analysis of this data set the following GO algorithm settings are used.

- $q = 128$
- $N_{gen} = 2000$
- $N_{runs} = 5$
- $p_c = 0.55$
- $F = 0.6$
- x- and y-boundaries (m) = -2 to +2
- z-boundaries (m) = 1.5 to 3.0
- s^2-boundaries (Pa^2) = 0 to 0.1

As the source locations are fixed, the frequency range in the emitted signal is exploited to test the use of the algorithm under the Rayleigh limit. Equation 3.1 provides a value of the frequency limit of 3502 Hz when $R = 0.161$ m (the distance between source 1 and 2), $D = 1.9$ m, $c = 343$ m/s, and $h = 2.56$ m (i.e. the distance to the array of source 1). Below this frequency the sources are no longer separable.

The best source locations and sources strengths found per frequency with GO are presented in Figure 5.2. The dashed lines indicate the true value. The best solution is defined as the candidate solution with the lowest energy of all runs and all generations. In the figures, the blue colour represents the strongest source, the orange colour the second strongest source, and yellow represents the weakest source. For the source strength, no reference values are available for the speakers. Therefore a reference is set by analysing the source strength of a single speaker over the frequency. This has been done with GO in combination with the CSM energy function, as literature has proven that for a single source this works perfectly [11]. Note that a certain source parameter (e.g. x_1) does not always have the same colour over frequency. This means that one of the speakers becomes weaker or stronger for a specific frequency. This can be correlated to the source strength plot, Figure 5.2d, where sometimes the weakest source seems to peak and become the strongest, such as at 4900 Hz.

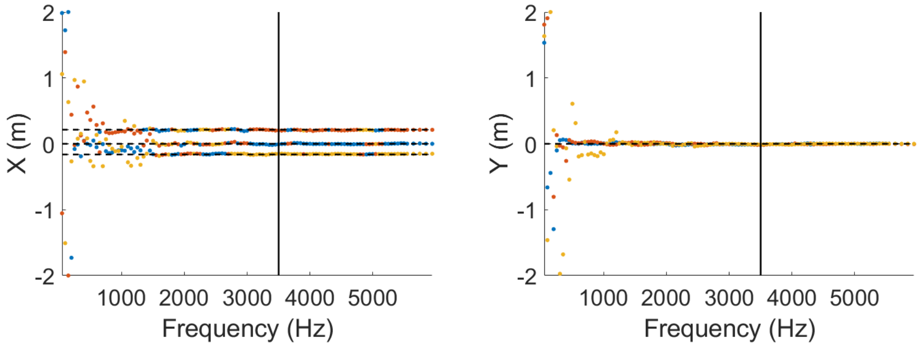

(a) Best location per frequency for the x-direction.

(b) Best location per frequency for the y-direction.

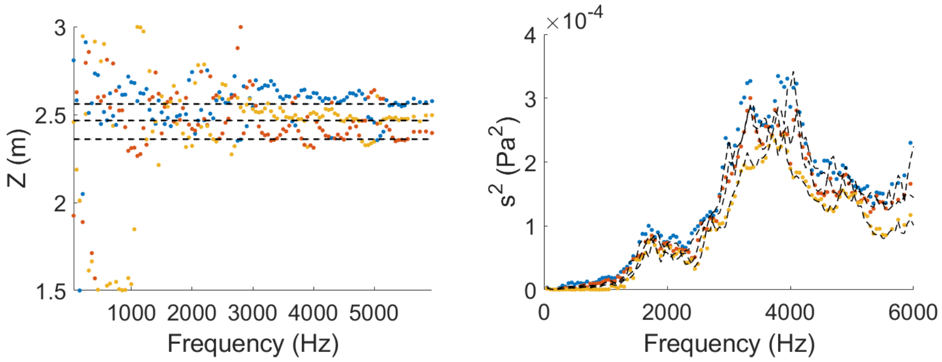

(c) Best location per frequency for the z-direction.

(d) Best source strength per frequency.

Figure 5.2: Location of the sources over frequency for the indoor experiments as found by GO with the CSM energy function. For each frequency the best result is presented, which contains three source locations and three source strengths. The dashed black lines indicate the real source position and strength. The vertical black line represents the Rayleigh limit. A blue dot corresponds to the strongest source, orange to the second strongest source, yellow to the weakest source. From the x-location plot it appears that the middle source (source 1) is the strongest for most frequencies, and source 2 (lowest value for x) the weakest. The z-location is not found properly until a frequency of 5350 Hz. Under the Rayleigh limit the x- and y-location as well as the source strength can still be determined as low as a frequency of 1650 Hz.

From Figure 5.2 can be concluded that the algorithm is capable of finding the x- and y-location to a limit of 1650 Hz while the Rayleigh limit is at 3502 Hz. At such low frequencies also the source strength found matches well with the real source strength. However, the z-location cannot be determined correctly at these low frequencies. In fact up to a frequency 5350 Hz the z-locations found are incorrect and deviate 10 cm. Lastly, the CB source map in Figure 5.1 showed that the second source is the weakest. This is seen with GO as well, with the weakest source (yellow) having a location of x is -0.161 m and z is 2.466 m corresponding to source 2 according to Table 2.1.

To check whether the algorithm converged well and fast, the convergence plots of GO with the CSM energy function for 5350 Hz are shown in Figure 5.3. The source location is easily found and considered stable after 800 generations. At this frequency the strongest source is found at the location of source 1, the weakest at the location of source 2. The source strength is varying more after 1000 generations, but converges as well within 2000 generations. The source strength is correctly found for the two weaker sources, while it underestimates the strength of the strongest source.

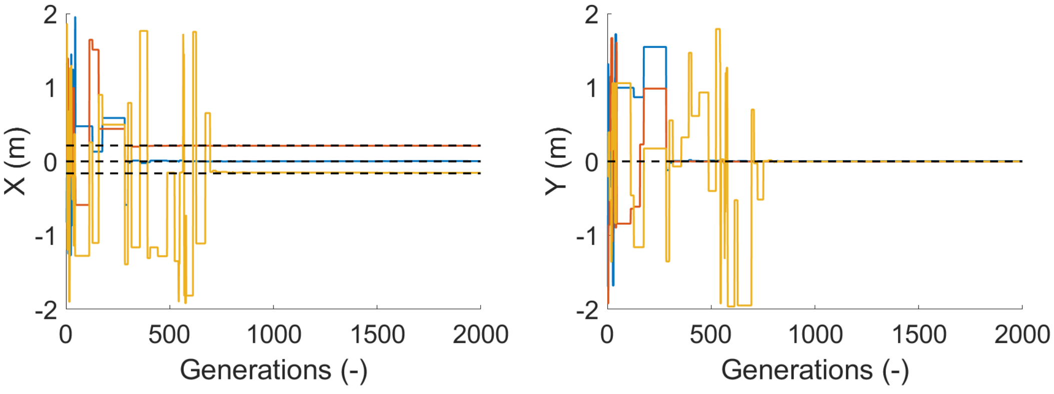

(a) Convergence for the x-direction.

(b) Convergence for the y-direction.

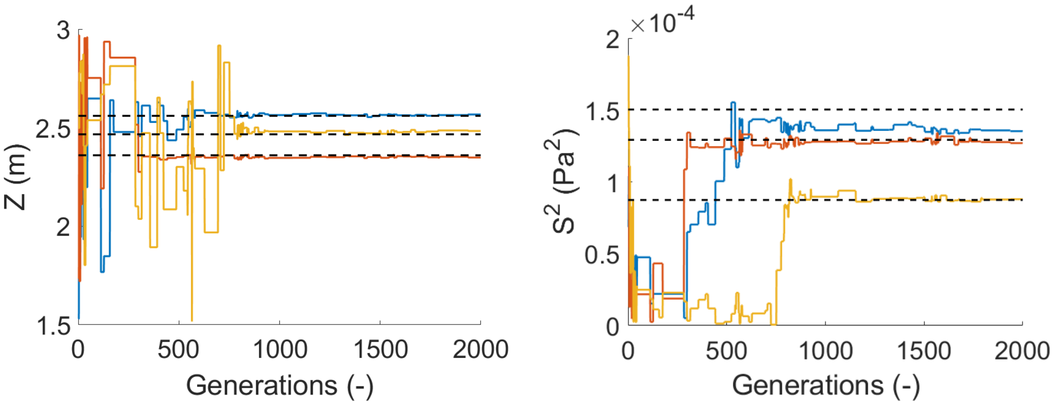

(c) Convergence for the z-direction.

(d) Convergence for the source strength.

Figure 5.3: Convergence plots of the source parameters for the indoor experiments as found by GO with the CSM energy function. The frequency presented is 5350 Hz, well above the Rayleigh limit. The dashed black lines indicate the real source position and strength. The blue line corresponds to the strongest source, orange to the second strongest source, yellow to the weakest source. The source locations are found perfectly within 1000 generations. However, the source strength is underestimated for the strongest source. The strongest source is found at the location of source 1, the weakest at the location of source 2.

As stated above, for a part of the frequencies below the Rayleigh limit, also the correct x- and y-locations are found. The minimum frequency at which this occurs, is 1650 Hz. It is interesting to see whether the algorithm did not yet converge for z or settles wrongly at this frequency. In the first case, more generations could potentially result in finding z. Therefore the convergence plots of GO with the CSM energy function are shown in Figure 5.4 for 1650 Hz. Again, within 1000 generations the algorithm converges. However, only for the x- and y-locations the correct values are achieved. The solutions hardly improve for z after 1000 generations although the z-locations do not match the real locations. The strongest source (blue) from Figure 5.4a is at the x-location of the third source, which is closest to the array and thus should correspond to the lowest z-value. The second strongest source (orange) from Figure 5.4a is at the x-location of the second source, which is at middle distance to the array and thus should correspond to the middle z-value. Thus, only for the weakest source the correct z-location is found. For the other sources it seems to find an optimum energy at the wrong distance to the array. The source strength is overestimated for the strongest source, but is correctly determined for the two weaker sources. At this frequency it appears that source 1 is not the strongest, but the weakest. Source 3 is now the strongest.

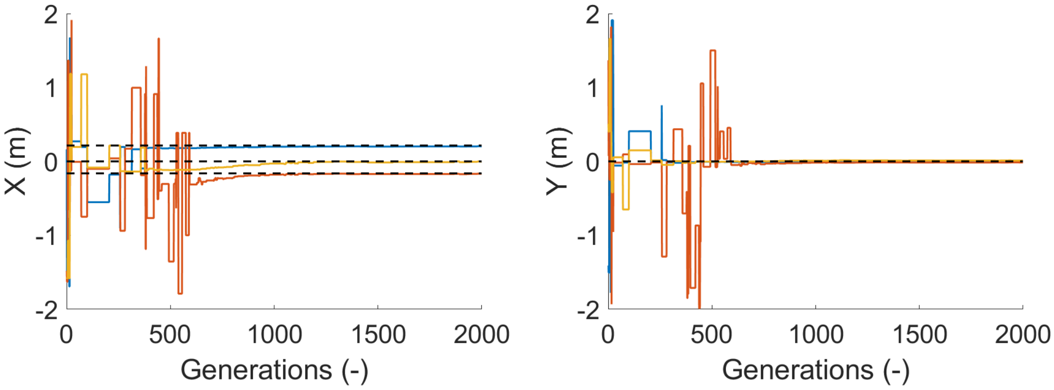

(a) Convergence for the x-direction.

(b) Convergence for the y-direction.

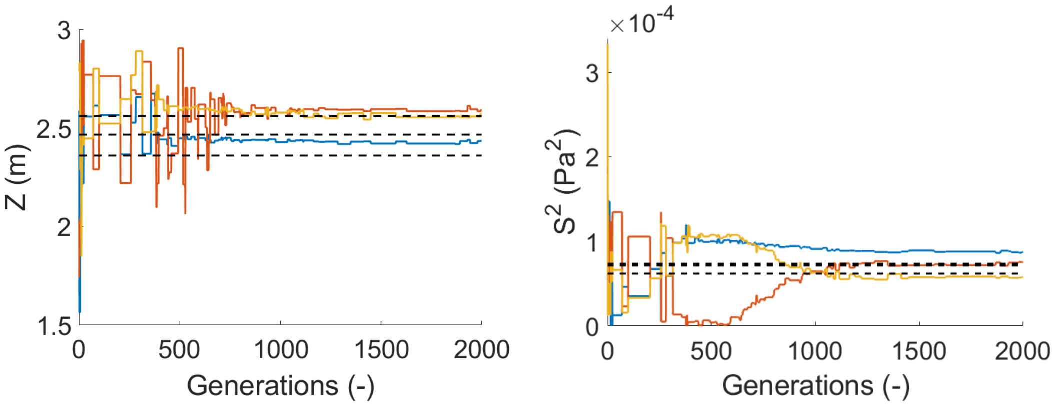

(c) Convergence for the z-direction.

(d) Convergence for the source strength.

Figure 5.4: Convergence plots of the source parameters for the indoor experiments as found by GO with the CSM energy function. The frequency presented is 1650 Hz, well below the Rayleigh limit. The dashed black lines indicate the real source position and strength. The blue line corresponds to the strongest source, orange to the second strongest source, yellow to the weakest source. The x- and y-locations are found perfectly within 1000 generations. The estimates for the z-locations do not chance drastically after 1000 generations, but the locations are incorrect for sources 2 and 3. The source strength is overestimated for the strongest source. The strongest source is found at the location of source 3, the weakest at the location of source 1.

From these results it is concluded that GO with the CSM energy function has difficulty in finding the z-location when sources differ in distance to the array. Especially at low frequencies where the x- and y-location as well as the source strength are still found, the z-location finds a local optimum. Also, these results indicate that GO with the CSM energy function is able to find the source x- and y-location under the Rayleigh limit, even though the z-location is incorrect. The source strengths found seem to match the sources well, especially for the weaker sources, even under the Rayleigh limit. From the analysis in this chapter it is expected that GO will have difficulty in identifying different heights on the aircraft, but will identify (x, y, s) correctly nonetheless.

6

Performance of GO on simulated fly-over data

GO proved successful in finding source locations and strengths in previous research with experimental data in the same 2D plane [10, 11, 35]. It also proved successful in finding sources at different distances from the array at higher frequencies, thus locate in the 3D field, see Chapter 5. However, these experiments both took place in a fully controlled set-up in an anechoic room with no reflections, and with the speakers in the array near-field. This means that the number of sources, the source location, and the source strength were known. This allowed for validation of the algorithm. In measurements of fly-over experiments, none of the aforementioned aspects about the sources will be known, neither will the source be at close distance to the array. Thus there will be propagation losses of the acoustic wave travelling over large distances. With so many unknown aspects, GO is first tested on a simulated data set representing an aircraft fly-over at a large distance from the array. With this data set, mainly the sensitivity of GO to its settings parameters and the number of sources it searches for (with respect to the number in the simulated measurement data) is tested. First, the results for the single frequency analysis, with energy functions from Sections 4.4.1 and 4.4.2, are shown in Section 6.1. After that, a first analysis is made of the ability of GO to find sources under the Rayleigh limit for aircraft fly-over data, in Section 6.2. Then the results of the multi-frequency case are shown in Section 6.3, linked to the energy functions in Section 4.4.3. Lastly, the GO algorithm is adapted to search for a single height for all the aircraft sources in Section 6.4.

6.1. Single frequency analysis

In this section the results of GO inversion on a single frequency are shown. For this, a simulated data set is generated at a frequency of 5500 Hz which shows a clear source map with a good balance between spatial resolution and spatial aliasing. The acoustic source map is shown in Figure 6.1 where the black stars indicate the location of the simulated data sources in the XY-plane according to Table 2.2.

The GO algorithm settings are as per the following. The settings as applied in the anechoic room experiment were found to lead to too slow convergence for the simulated data. Thus the first five parameters are based on values as used in research by [10]. Note that the boundaries for source strength are only applicable when GO with the CSM energy function is used.

- $q = 128$
- $N_{gen} = 2000$
- $N_{runs} = 10$
- $p_c = 0.75$
- $F = 0.4$

- x-boundaries (m) = -30 to +30
- y-boundaries (m) = -35 to +10
- z-boundaries (m) = 200 to 300
- s-boundaries (Pa) = 0 to 5

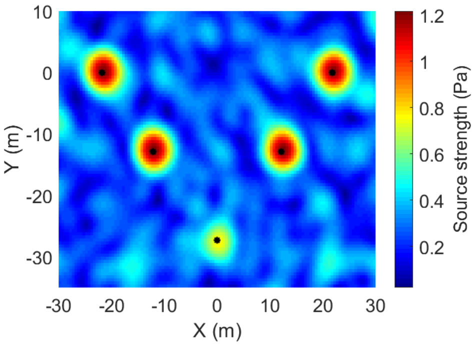

Figure 6.1: CB acoustic source map for the simulated data set at a frequency of 5500 Hz. The black stars indicate the real position of the simulated sources. The source map is made at a distance of 250 m, corresponding to the z-location of all engines. The sources are clearly visible.

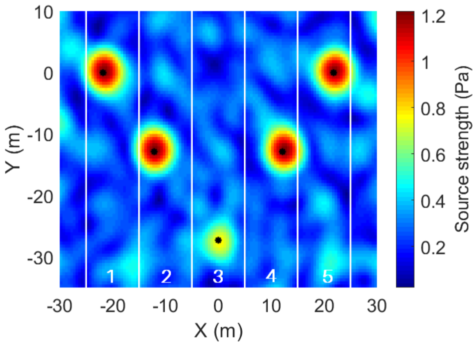

Figure 6.2: Indication of the five search zones applied in x-direction to the simulated data set. The limits of a zone are indicated by the white vertical lines. The search zone stretches from -40 to 40 m in y-direction. The zone is numbered by the source that is in its zone, thus search zone 1 will find source 1 from Table 2.2.

A first analysis on a simple simulated data set with these algorithm settings showed that the algorithm is not converging to the correct values for the unknowns. For GO with the BF energy function all found sources are exactly the same, thus it found only one source. For GO with the CSM energy function, the x- and y-locations are found, but no convergence is achieved for the z-direction and source strength with these algorithm settings.

As to find z and s more generations are needed to converge than the x- and y-direction, the full system cannot converge within 2000 generations. To solve both the problem for the BF as well as the CSM energy function, stricter boundaries for the x- and y-direction are set. The boundaries are set in x-direction, leaving the y-direction free for the algorithm to search in. The boundaries create search zones as shown in Figure 6.2 by the white lines, each containing a single source. The x-boundaries for the first source run from -25 to -15 m. Then with every next set of boundaries, 10 m is added to the lower and upper boundary with respect to the previous source. The upper limit for one source is the lower limit for the next source in the x-direction.

6.1.1. BF energy function

GO is applied with the BF energy function first. As explained before, the boundaries are set to five regions for x and thus it searches for five sources. With the BF energy function only (x, y, z) are searched and thus no convergence plots of s will be shown. In Figure 6.3 the convergence plots for the x-, y-, and z-direction are shown for the best candidate per generation of the best of the 10 runs. Applying GO with the BF energy function shows that the algorithm is capable to find all five sources at the correct location for a frequency of 5500 Hz. Figure 6.3c reflects that indeed for the z-direction a larger number of generations is needed to converge to the correct values even though the algorithm is already supported by setting strict boundaries. If needed, the source strengths can be computed by applying the energy function with a fourth order normalisation for $\boldsymbol{g}$ for the final locations.

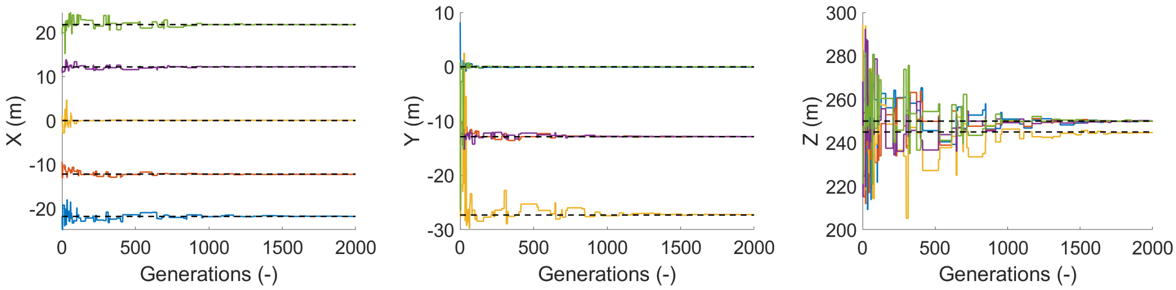

(a) Convergence for the x-direction.

(b) Convergence for the y-direction.

(c) Convergence for the z-direction.

Figure 6.3: Convergence plots of the source parameters for the simulated data set as found by GO with the BF single frequency energy function. The black dashed line indicates the real source location. The correlation between line colour and source number can be found in Table 2.2. For all 5 sources, the locations are found correctly within 1200 generations.

Figure 6.3 shows that the algorithm converges yet the convergence plots do not show the accuracy of the final solution as clearly. The convergence plots also are only presented for the best run and do not indicate whether the other independent runs found similar results. Therefore, Figure 6.4 is added. This figure is built up out of box plots with a box plot per parameter, grouped by parameter type. Thus Figure 6.4a contains box plots for all five x. The values of the box plot are computed with the best candidate of all 10 runs. In a box plot one can see the median of the results, indicated by the red line. The lower limit of the box indicates the middle number between the median and the smallest number, also called the first quartile. The upper limit of the box represents this for the median and the largest number, the third quartile. The whiskers represent the respective minimum and maximum number of the data set. Any outliers are indicated by a red cross. Additionally these box plots contain a horizontal black dashed line indicating the true value of the parameter (corresponding to Table 2.2). Note that for clarity around the x- and y-parameters a margin of ± 2 m is taken, for z this is ± 20 m, and for s, which will be shown only at the CSM energy function, this is ± 0.2 Pa. For all boxplots the same margins are chosen as this makes them easier to compare. This might however result in box plots with very small boxes, which then thus indicates no spread in the data set.

The size of the box in the box plot gives an indication of the convergence behaviour. If the box is small, then for all the runs nearly the same solution is found, which is thus the global optimum. If the median, the red line, is close to the horizontal black dashed line, this indicates that the solutions found are close to the real parameter value. For the single frequency BF energy function, all boxes are very small and the median is close to the true parameter value. Thus, successful convergence is achieved here for all runs.

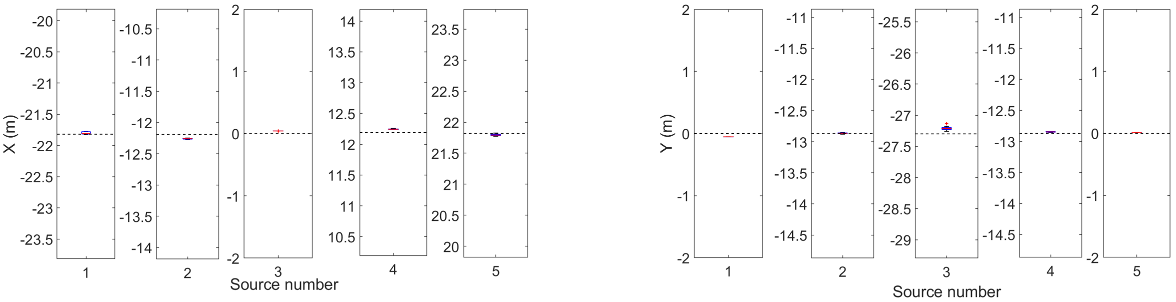

(a) Box plot for the x-direction.

(b) Box plot for the y-direction.

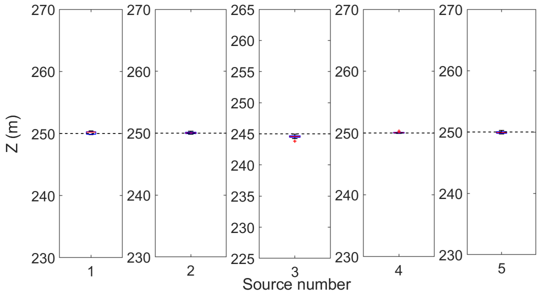

(c) Box plot for the z-direction.

Figure 6.4: Box plots of the source parameters for the simulated data set as found by GO with the BF single frequency energy function. The small size of the box indicates that all 10 independent runs converge to the same parameter. For all 10 runs the position is correctly found.

As it is unknown how GO will react when the number of sources it searches for does not equal the number of sources in the data, this is tested by applying a search for two sources and a search for seven sources, but with the simulated data set still as the result of five sources. The results of such a search on simulated data will help understanding the results of a search on fly-over data when there is a different number of sources present than initially thought. For these searches, only the convergence behaviour will be shown as the goal is not to see the accuracy of the solution, but rather to see the behaviour of the algorithm.

The results of GO with the BF energy function for a search for two sources are presented in Figure 6.5. The search zones defined by the boundaries are now set broad with a slight overlap. This would be the case when accidentally two sources are present within a search zone. So for the first zone the boundaries are from -30 to 5 m in x, and for the second zone from -5 to 30 m in x. The algorithm converges to two of the sources that are present in the simulated data set. For GO with BF it is concluded that too few sources as input leads to finding only the strongest sources. These sources are easily found within 300 generations.

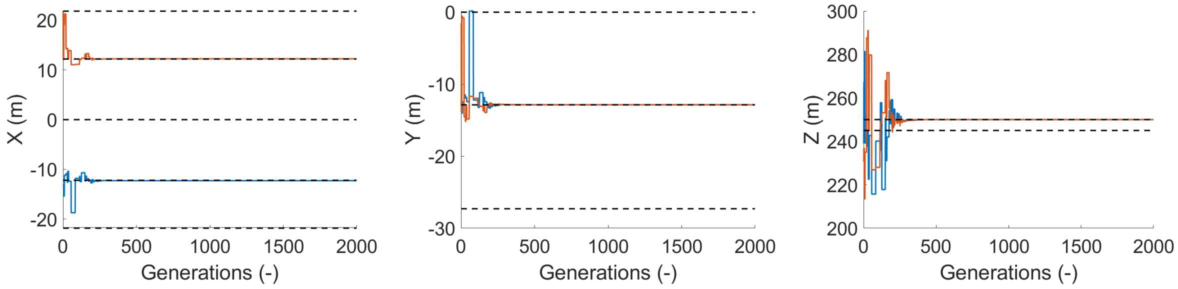

(a) Convergence for the x-direction. (b) Convergence for the y-direction. (c) Convergence for the z-direction.

Figure 6.5: Convergence plots of the source parameters for two sources in the simulated data set as found by GO with the BF single frequency energy function.The algorithm searches for two sources where there are five present. The two sources it finds are two of the strongest four sources. Convergence is achieved in 300 generations.

GO with the BF energy function has also been tested for a search for seven sources when five sources are present. In such a case, the boundaries for the first five zones are the same as in Figure 6.2 and the other two are left fully free. This would be the case when a researcher wants to find an extra source which is not visible in the source map. As can be seen from Figure 6.6, the additional two sources (red and light blue lines) converge to the strongest source location. However, this distorts the search in z-direction for all sources fully. Although convergence is reached, the correct z-values are not found. For GO with BF it is concluded that too many sources with the same source strength as input leads to a strong disturbance in which not all sources are found anymore. When each source has a different source strength, GO with BF is however capable of finding all sources and, as seen earlier, will find the strongest source multiple times.

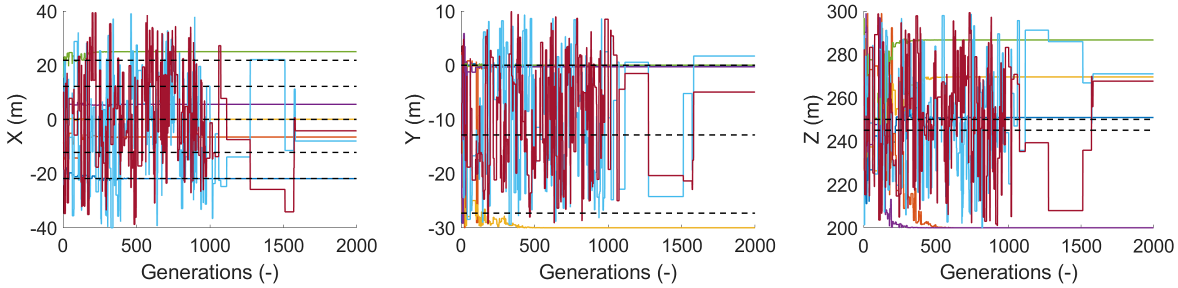

(a) Convergence for the x-direction. (b) Convergence for the y-direction. (c) Convergence for the z-direction.

Figure 6.6: Convergence plots of the source parameters for seven sources in the simulated data set as found by GO with the BF single frequency energy function.The algorithm searches for seven sources where there are five present. The algorithm is completely disturbed and is only able to find the first source (dark blue) correctly.

6.1.2. CSM energy function

In this section GO is applied with the CSM energy function. As explained before, the boundaries are set to five regions for x and thus it searches for five sources. In Figure 6.7 the convergence plots for the x-, y-, and z-location as well as the source strength of the best of the 10 runs are shown. Figure 6.7 shows that the x- and y-location of the sources are found correctly, but that the z-direction of the source needs more than 2000 generations. Compared to GO with E_{BF}, more generations are needed to converge for z when using E_{CSM}. This is perhaps due to the increased number of parameters or due to a compensation of a larger z with a higher s. The found locations for z are however within 5 m of their real position, thus the simulation could be helped to converge better within 2000 generations by setting more strict boundaries on z. The source strength did converge very well, but is slightly further from reality than the source strength values found by E_{BF}. This is expected to be due to a larger number of parameters to optimise for.

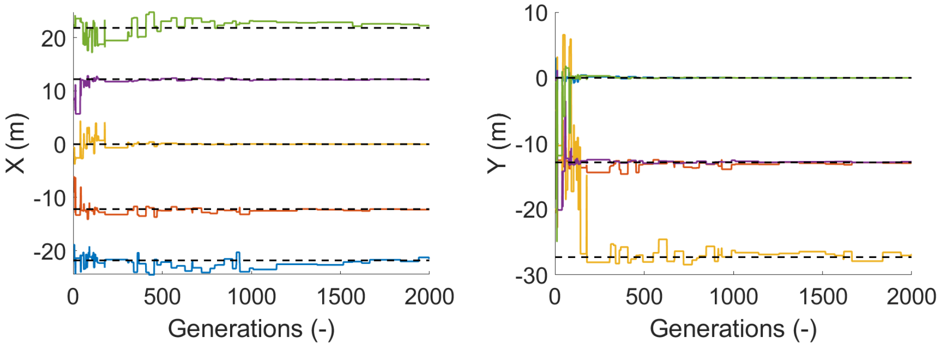

(a) Convergence for the *x*-direction.

(b) Convergence for the *y*-direction.

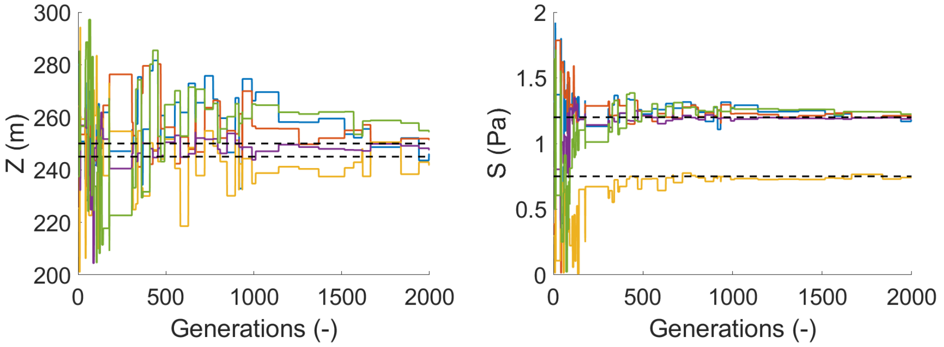

(c) Convergence for the *z*-direction.

(d) Convergence for the source strength.

Figure 6.7: Convergence plots of the source parameters for the simulated data set as found by GO with the CSM single frequency energy function. The black dashed line indicates the real source location. The correlation between line colour and source number can be found in Table 2.2. For all 5 sources, the (x, y, s) are found within 1200 generations. More than 2000 generations are needed to converge fully for z.

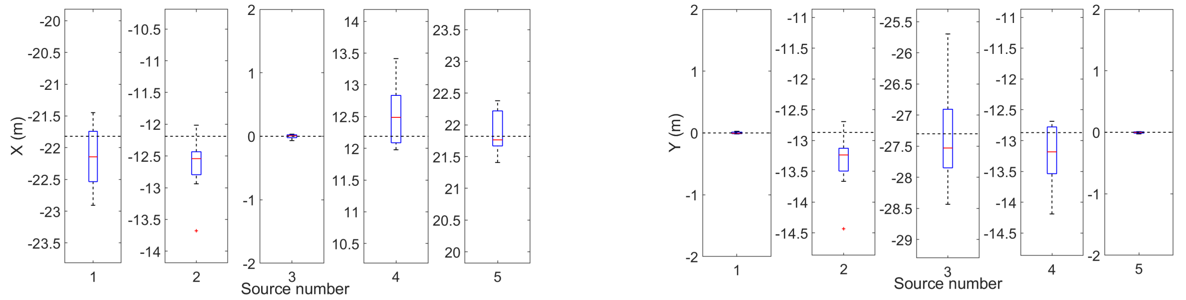

(a) Box plot for the *x*-direction.

(b) Box plot for the *y*-direction.

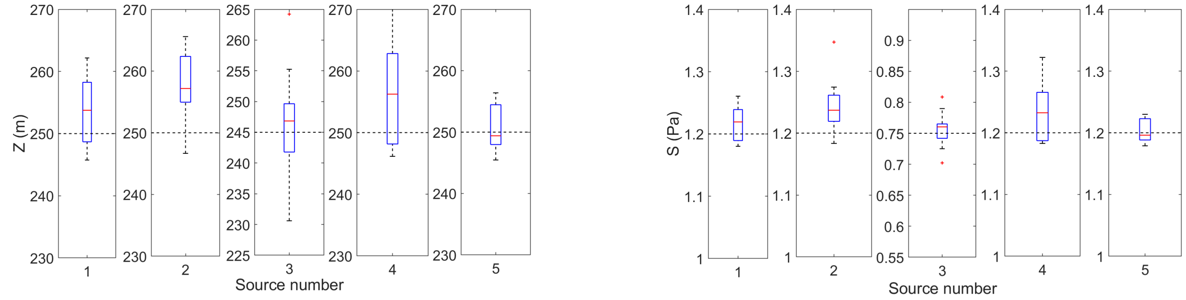

(c) Box plot for the *z*-direction.

(d) Box plot for the source strength.

Figure 6.8: Box plots of the source parameters for the simulated data set as found by GO with the CSM single frequency energy function. The z-direction shows large deviations. For the nose landing gear (source 3) the x-position is well found but the y-position shows large deviations.

Figure 6.8 with box plots is added again to show the convergence behaviour of all runs. A larger spread over the runs can be seen for the CSM energy function than is seen for the BF energy function. Especially for the z-direction large deviations are observed as could be expected from the convergence plot (Figure 6.7c) of the best run already. Clearly, z is more difficult to find. Apart from that, the medians are further away from the true value for the analysis with the CSM energy function, but always within 0.5 m for x and y, and within 0.05 Pa for s. For the nose landing gear (source 3) the x-position is well found but the y-position shows large deviations.

Similar to the analysis of the simulated data set with the BF energy function, the CSM energy function is tested for different numbers of sources. The results of GO with the CSM energy function for a search for two sources are presented in Figure 6.9. The algorithm converges to two of the sources that are present in the simulated data set and z is now found correctly. However it appears that for the strongest source, it overestimates the source strength. For GO with CSM it is concluded that too few sources as input leads to finding only the strongest sources, yet overestimating the source strengths.

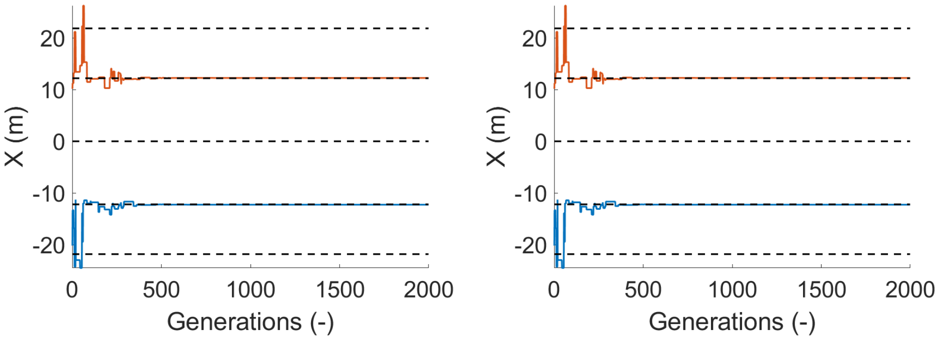

(a) Convergence for the x-direction.

(b) Convergence for the y-direction.

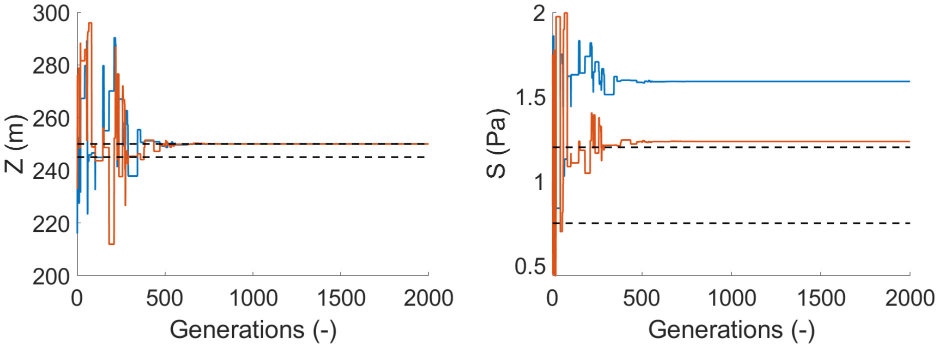

(c) Convergence for the z-direction.

(d) Convergence for the source strength.

Figure 6.9: Convergence plots of the source parameters for two sources in the simulated data set as found by GO with the CSM single frequency energy function. The algorithm searches for two sources where there are only five sources present. Convergence is achieved in 400 generations, but s is overestimated for both sources.

GO with the CSM energy function has also been tested in case of a search for seven sources when five sources are present. It causes the algorithm to not find the third source (yellow) within the boundaries anymore as it satisfies this location with the sixth source (light blue). Thus the two extra sources are represented by the red and yellow lines. As can be seen from Figure 6.10, for the additional two sources only convergence for the source strength is obtained. The source strength for these extra sources is nearly 0 Pa, implying that they can be ignored. For GO with CSM it is concluded that too many sources as input leads to finding sources at very low source strengths which are not present. This behaviour is desired, since it corresponds to the robustness of the method. This is also true when the sources have different strengths, however it is easier to find convergence then.

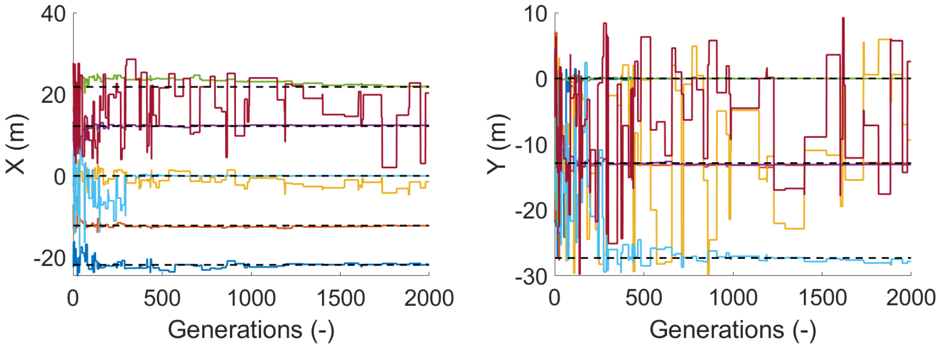

(a) Convergence for the x-direction.

(b) Convergence for the y-direction.

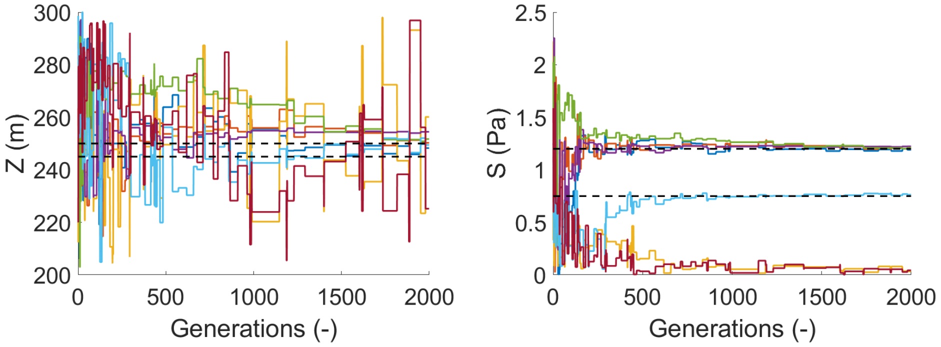

(c) Convergence for the z-direction.

(d) Convergence for the source strength.

Figure 6.10: Convergence plots of the source parameters for seven sources in the simulated data set as found by GO with the CSM single frequency energy function. The algorithm searches for seven sources where there are only five sources present. The red and yellow lines indicate the search for non-existent sources and appear not converging for location, while converging to very low source strengths. The correct (x, y, s) for the remaining five sources is found.

6.2. Source determination under Rayleigh limit

With this simulated data set also GO's ability to find sources under the Rayleigh limit is analysed for the far-field case. Recalling Equation 3.1, a frequency can be selected at which the sources are spaced closer together than the Rayleigh limit and are thus seen as a single source. With $c = 343$ m/s, $h = 250$ m, $D = 3.4$ m the Rayleigh limit is 20.51 m for a frequency of 1500 Hz. This means that the engines are not separable in the CB source map, see Figure 6.11.

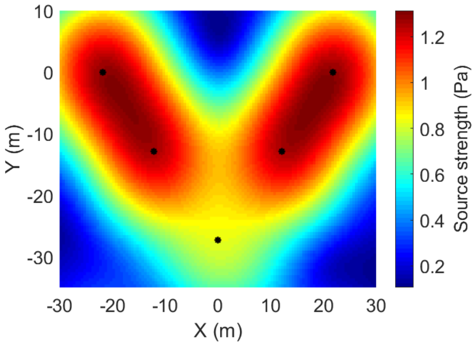

Figure 6.11: CB acoustic source map for the simulated data set at a frequency of 1500 Hz, i.e. below the limit where the sources are still separable according to the Rayleigh limit. The black stars indicate the real position of the simulated sources. The source map is made at a distance of 250 m, corresponding to the z-location of all engines. The engines are not separately visible. Also the nose landing gear cannot be distinguished.

6.2.1. BF energy function

Applying the standard GO search for five sources with the BF energy function shows that the algorithm converges within 600 generations, see Figure 6.12. However, the resulting source locations did not converge to the real locations. Source 2 (orange) and 4 (purple) hit the limit in the x-direction trying to merge with the outer most sources. Source 3 (the nose landing gear, yellow) also goes entirely towards the x-boundary. For the y-location, Figure 6.12b shows for sources 1, 2, 4, and 5 a location in between the true locations. The GO with BF in this case thus converges to regions of higher levels in the beamform plot caused by the overlap of main lobe of the PSF of source 1 and 2 and source 4 and 5. The location found for source 3 is close to the high level region on the negative x-side of the beamform plot. Thus, GO applied with the BF energy function is not able to find sources correctly under the Rayleigh limit. This is as expected as this energy function suffers from the same disadvantages as CB. Surprisingly it is able to find the correct height for two out of five sources. These two sources are those closest to their real location in (x, y).

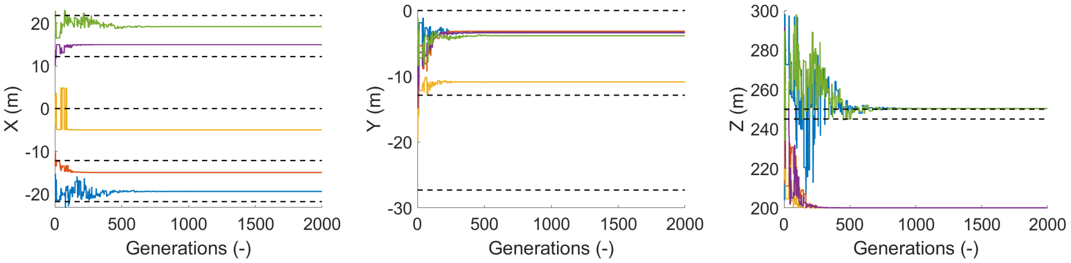

(a) Convergence for the x-direction.

(b) Convergence for the y-direction.

(c) Convergence for the z-direction.

Figure 6.12: Convergence plots of the source parameters for the simulated data set as found by GO with the BF single frequency energy function, below the Rayleigh limit. The candidate solution stabilises very fast at 500 generations, but does not converge to the correct location. However, for two sources the correct height is found.

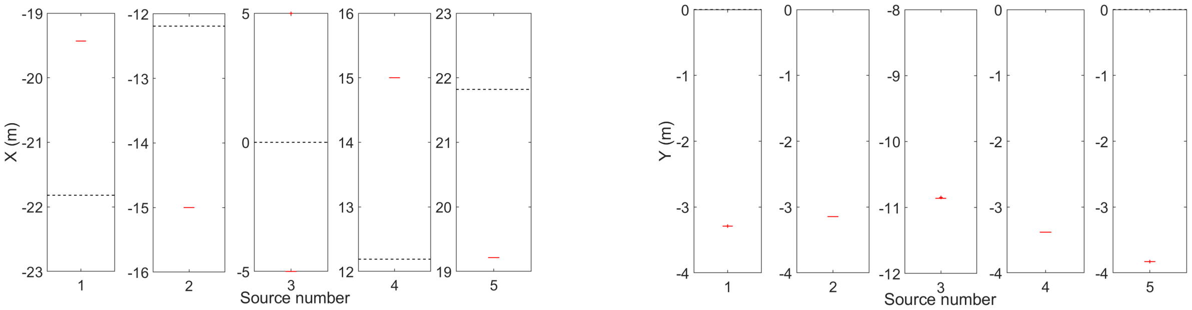

(a) Box plot for the x-direction.

(b) Box plot for the y-direction.

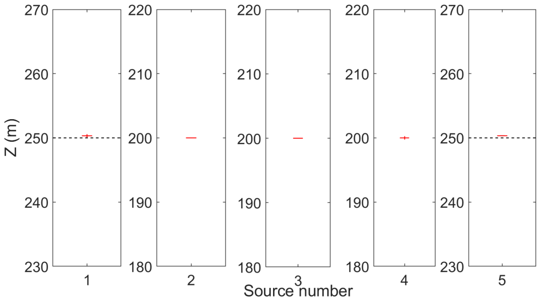

(c) Box plot for the z-direction.

Figure 6.13: Box plots of the source parameters for the simulated data set as found by GO with the BF single frequency energy function, below the Rayleigh limit. The box plots are not made with the margins as introduced earlier as the values found are too far off from the true source parameters for x and y and most z.

The box plots are added in Figure 6.13. Note that the margins around the true value as introduced in the previous section, are not used here. The values found are too far from the true parameter values, as could already be concluded from the convergence plots in Figure 6.12. Only where possible the reference value for the source position is added. It appears that the BF energy function is able to locate the height of strong sources. In conclusion, under the Rayleigh limit this energy function will only be of use to find the height of dominant sources.

6.2.2. CSM energy function

Applying the GO search for five sources with the CSM energy function shows that the algorithm converged for a large part within 1000 generations for the x- and y-direction and source strength, however it has difficulty converging for the z-direction, see Figure 6.14. Yet, using the CSM energy function, the source locations and strengths can be found in a satisfactory manner especially when increasing the generations to find a better solution for z. An even lower frequency was tested, a frequency of 500 Hz, unfortunately here the algorithm did not converge.

The ability to find sources under the Rayleigh limit is however not unlimited and is most likely influenced by the SNR and also by the frequency [10]. For further research, it is interesting to find out if there is a certain limit to which the source location can still be determined.

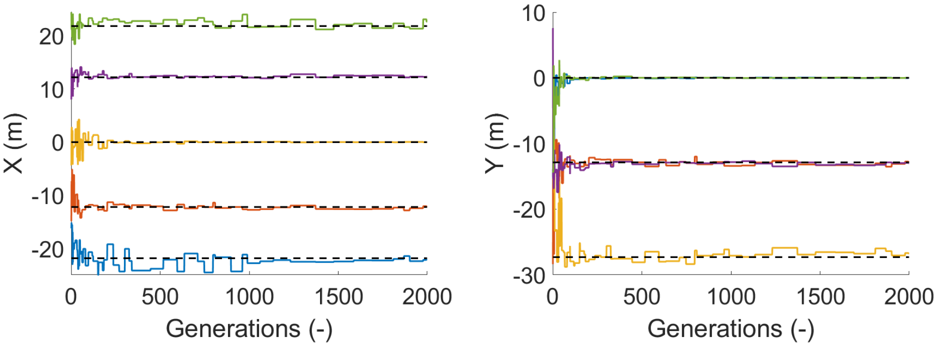

(a) Convergence for the x-direction.

(b) Convergence for the y-direction.

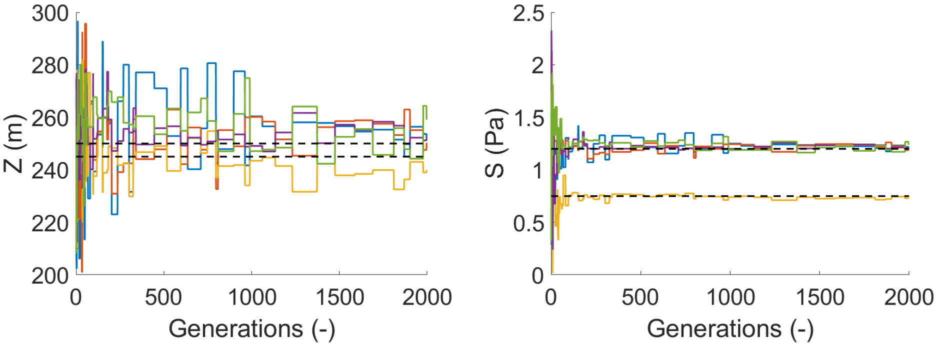

(c) Convergence for the z-direction.

(d) Convergence for the source strength.

Figure 6.14: Convergence plots of the source parameters for the simulated data set as found by GO with the CSM single frequency energy function, below the Rayleigh limit. Convergence is achieved for parameters (x, y, s) after approximately 1000 generations. The search for z only slowly converges and more than 2000 generations are needed.

Figure 6.15 shows very similar sizes of the box compared to Figure 6.8 for the x- and y-direction. However, for source 5 the x-direction contains a large spread and a the median is relatively far from the true value (1 m). Figure 6.14a already hinted this as there source 5 (green line) also has difficulty converging fully within 1000 generations. For the z-direction more spread over the runs is seen. The source strength is well found.

With this analysis the use of GO with the CSM energy function to find sources spaced within the Rayleigh limit is confirmed.

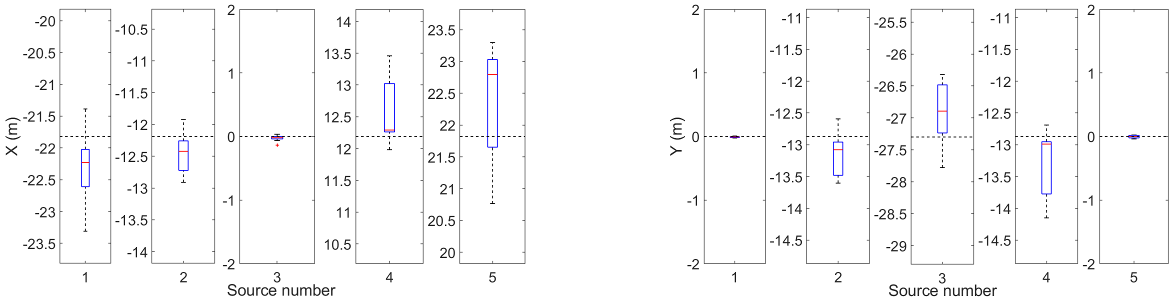

(a) Box plot for the x-direction.

(b) Box plot for the y-direction.

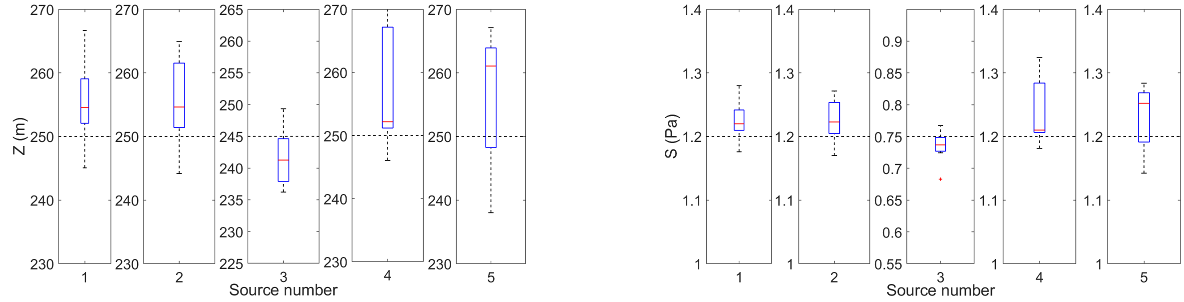

(c) Box plot for the z-direction.

(d) Box plot for the source strength.

Figure 6.15: Box plots of the source parameters for the simulated data set as found by GO with the CSM single frequency energy function, below the Rayleigh limit. The box plots are very similar to the case above the Rayleigh limit, showing only more uncertainty on the z-parameters.

6.3. Multi-frequency analysis

Next to the single frequency analysis, a multi-frequency analysis was performed. The main reason for this is to see if faster convergence is reached as local optima in one frequency could be taken out when at the other frequencies this does not result in a lower energy. In this analysis a low frequency band from 1500 to 4500 Hz has been used, although applied in steps of 500 Hz to limit computational time. This band is based on a common low frequency band that is often used in aircraft imaging research [30]. The source map of this band is shown in Figure 6.16.

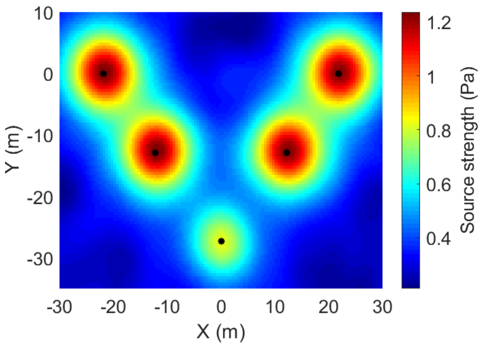

Figure 6.16: CB acoustic source map for the simulated data set at a low frequency band from 1500 to 4500 Hz. The black stars indicate the real position of the simulated sources. The source map is made at a distance of 250 m, corresponding to the z-location of all engines. The sources are clearly visible.

The multi-frequency inversion constraints the unknown parameters that are independent of frequency (i.e. in general not source strength) more tightly, since a good match needs to be found for a realisation of the unknowns for all frequencies.

6.3.1. BF energy function

Multi-frequency analysis with a BF energy function might especially be useful when frequencies are included where the CB source map suffers from low spatial resolution and many side lobes.

In Figure 6.17 it is seen that the correct source locations are found and that convergence is achieved fast, while there are frequencies included where the sources are under the Rayleigh limit.

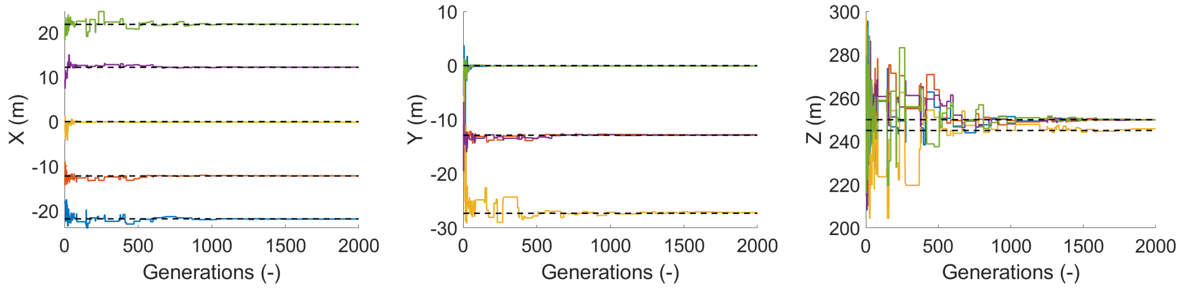

(a) Convergence for the x-direction.

(b) Convergence for the y-direction.

(c) Convergence for the z-direction.

Figure 6.17: Convergence plots of the source parameters for the simulated data set as found by GO with the BF multi-frequency energy function. The sources are found perfectly within 1000 generations.

Figure 6.18 is added again to show that the runs find the same solution. There is hardly any improvement for the multi-frequency case with respect to the single frequency case.

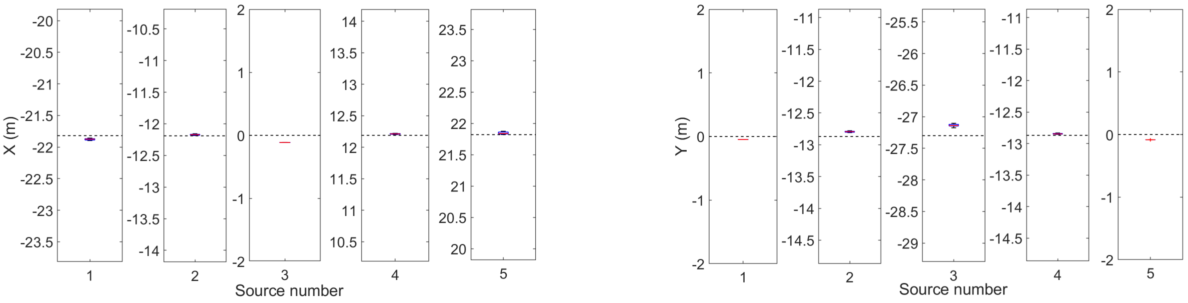

(a) Box plot for the x-direction.

(b) Box plot for the y-direction.

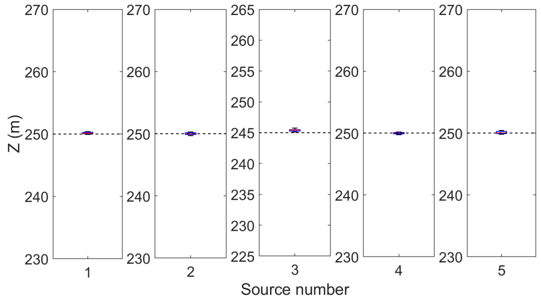

(c) Box plot for the z-direction.

Figure 6.18: Box plots of the source parameters for the simulated data set as found by GO with the BF multi-frequency energy function. The box plots show that all runs find the same, correct, values.

It is concluded that multi-frequency analysis could improve the results for a frequency band which includes frequencies where the sources are under and above the Rayleigh limit. However, this is computationally expensive and still does not allow for a real analysis of sources under the Rayleigh limit. Thus, above the Rayleigh limit a single frequency analysis is advised.

6.3.2. CSM energy function

As GO with CSM is able to find sources under the Rayleigh limit, see Section 6.2.2, it is expected that the multi-frequency analysis only supports fast convergence and perhaps supports finding the correct z-location. In Figure 6.19 it is visible that the correct source locations are found in x- and y-direction, but that again the search is not fully converged in z-direction.

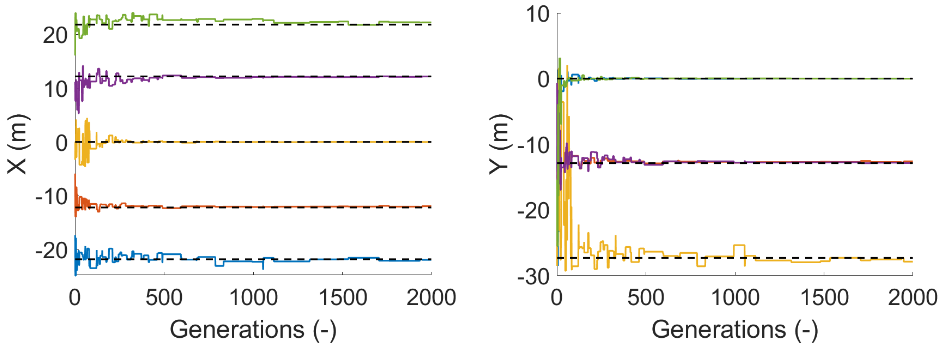

(a) Convergence for the *x*-direction.

(b) Convergence for the *y*-direction.

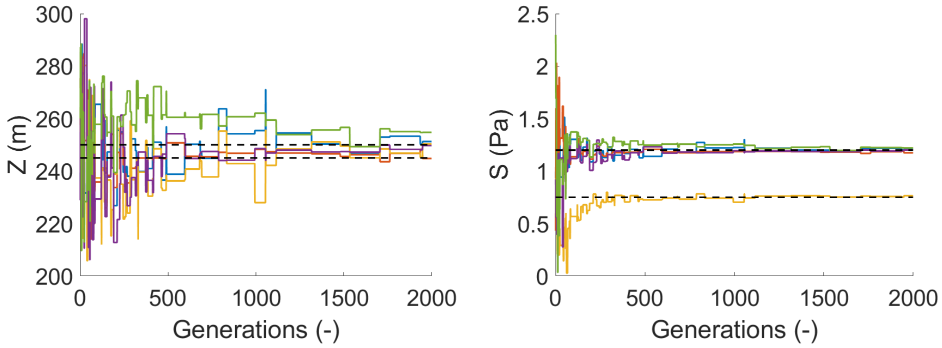

(c) Convergence for the *z*-direction.

(d) Convergence for the source strength.

Figure 6.19: Convergence plots of the source parameters for the simulated data set as found by GO with the CSM multi-frequency energy function. The parameters for *z* are already more converged after 2000 generations than in the single frequency analysis, but still it is not correct, while the other parameters converged in 1000 generations.

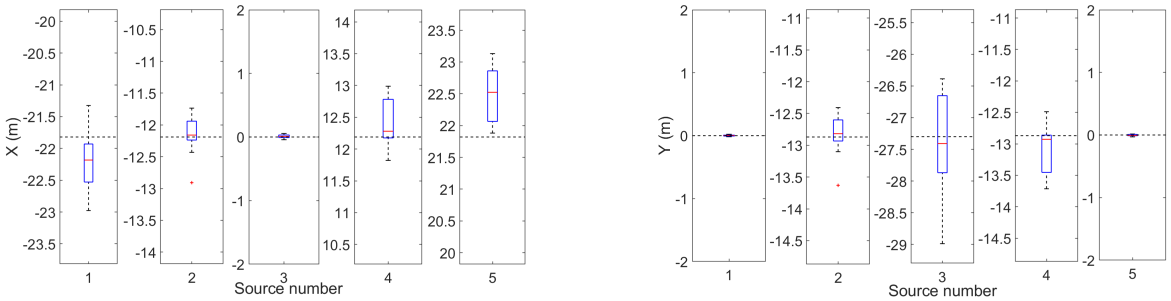

(a) Box plot for the *x*-direction.

(b) Box plot for the *y*-direction.

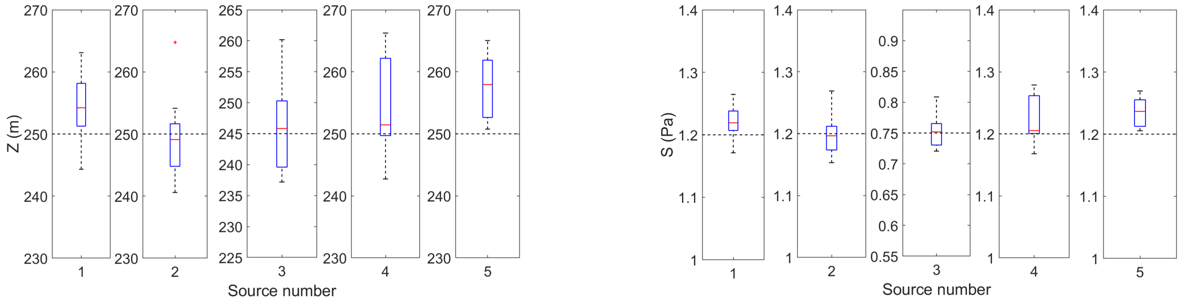

(c) Box plot for the *z*-direction.

(d) Box plot for the source strength.

Figure 6.20: Box plots of the source parameters for the simulated data set as found by GO with the CSM multi-frequency energy function. The medians are mostly close to the true value, but the spread of the box remains roughly the same size as for the single frequency case.

When Figure 6.20 is compared to Figure 6.8 one notices that there is only a very small improvement visible in box sizes. However, for most parameters in the x- and y-direction, as well as for the source strength, the median is closer to the true parameter value. The expected improvement on the z-direction is however marginal. For sources 2, 3, and 4 the median is closer to the true value, but the spread remains large.

It is concluded that for GO with the CSM energy function only marginally better z-locations are found, while the computational time increases strongly.

6.4. Single aircraft height

As the previous results all show a sincere difficulty to converge for the z-direction for large distances in z, an extra test has been performed. In this test, the height of the aircraft is searched instead of a height per source, thus there is now only one z-parameter. As the differences in height between different elements on the aircraft (e.g. landing gear and engines) are within 5 m, it is expected that using the same z-value for all sources is a valid assumption. Searching for only one z-location lowers the number of search parameters and might result in a faster convergence.

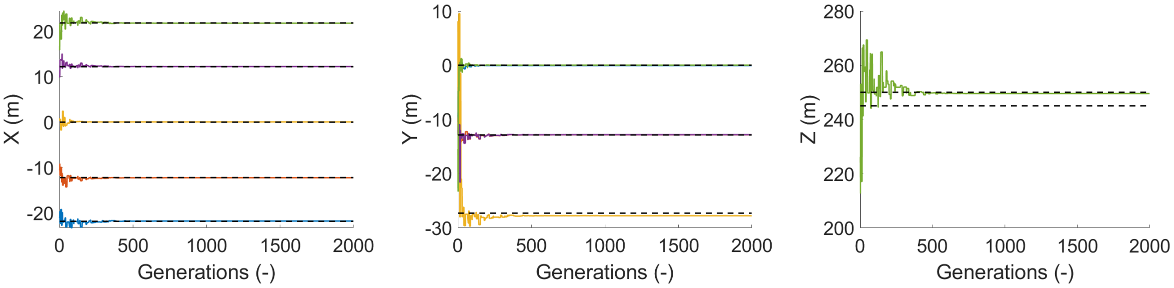

(a) Convergence for the x-direction.

(b) Convergence for the y-direction.

(c) Convergence for the z-direction.

Figure 6.21: Convergence plots of the source parameters for the simulated data set as found by GO with the BF single frequency energy function when searching for a single aircraft height. The (x, y) per source is found within 200 generations. For z 500 generations were needed. It finds the z-value corresponding to the z of four of the sources.

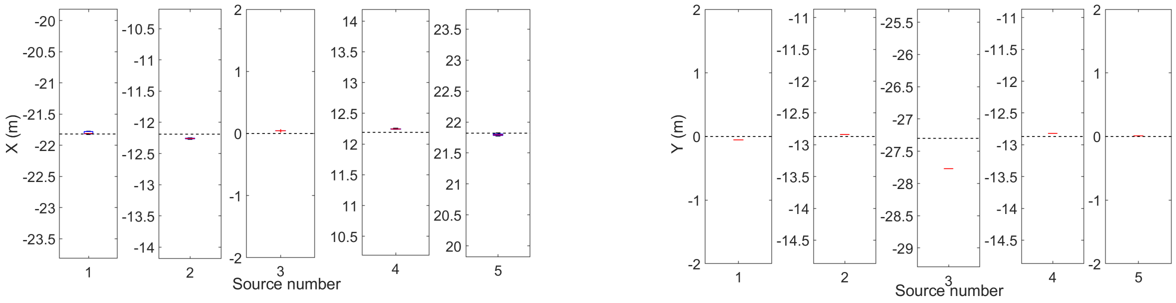

(a) Box plot for the x-direction.

(b) Box plot for the y-direction.

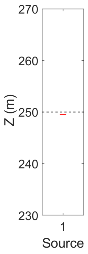

(c) Box plot for the z-direction.

Figure 6.22: Box plots of the source parameters for the simulated data set as found by GO with the BF single frequency energy function when searching for a single aircraft height. The box plots show that all runs find the same, correct, values.

6.4.1. BF energy function

The results for a single z search for GO with BF are shown in Figure 6.21. The convergence is achieved within 500 generations with a perfect convergence for the z-direction as well. There are different source heights indicated in the simulated data set and here, the z-location of the largest number of sources is found. This is due to the fact that it finds the lowest energy when using this z-location is used.

Figure 6.22 shows that the runs do not show any spread at all. Thus the results are the same for all sources. The height of the strongest sources is found. This means that the height is incorrect for the nose landing gear (source 3). The effect of this is clearly visible in Figure 6.22b where an offset is seen between the median and the true value for y.

From this section can be concluded that the BF energy function will find the accurately the height of the strongest sources.

6.4.2. CSM energy function

The results for GO with CSM and searching for one height only are shown in Figure 6.23. The convergence is achieved within 500 generations for the x- and y-location as well as the source strength. However, the algorithm struggles to get the z-location correct. In fact, it stays around 260 m where it is expected to find 250 m like the BF energy function does. For source 3 (yellow), which has a height of 245 m, there is a clear offset in the found y-location and source strength which potentially is caused by the too high z-location.

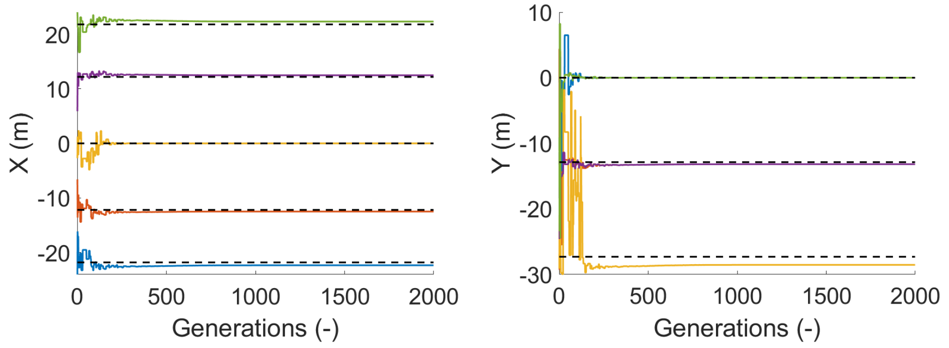

(a) Convergence for the x-direction.

(b) Convergence for the y-direction.

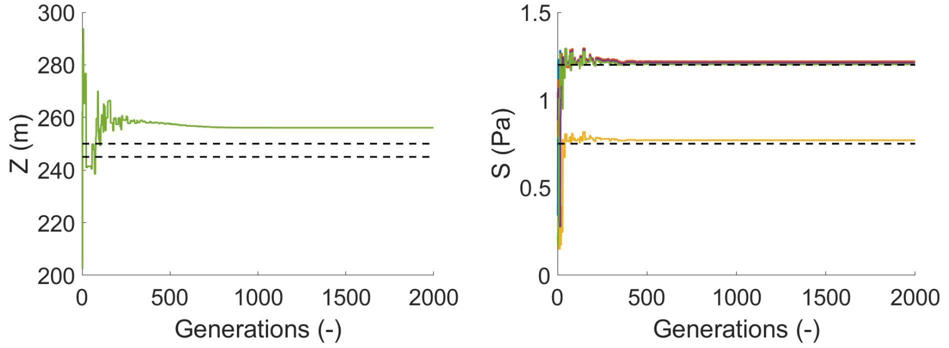

(c) Convergence for the z-direction.

(d) Convergence for source strength.

Figure 6.23: Convergence plots of the source parameters for the simulated data set as found by GO with the CSM single frequency energy function when searching for a single aircraft height. z is overestimated, but most source locations are still found.

The box plots in Figure 6.24 show that the deviations over the runs, i.e. the spread of the boxes, is smaller. However, the median is far from the true value. Also, for nearly all box plots an outlier is apparent. These outliers are closer to the true parameter value. The convergence plots in Figure 6.23 are from the run with all outliers. The box plot in Figure 6.22c shows that the resulting z for the other runs is worse than presented in Figure 6.23c. If this method will be used, then it is strongly advised to allow more independent runs.

From this section can be concluded that the CSM energy function will have difficulties in finding a relevant height. For the case considered the algorithm overestimates the height of the aircraft when a single representative height is searched for.

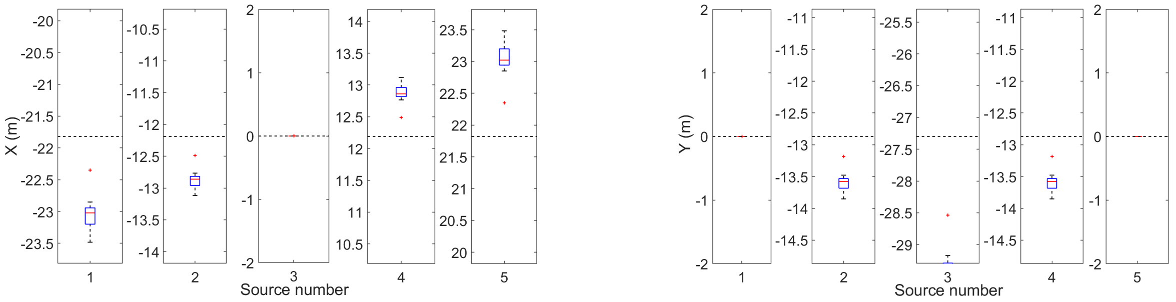

(a) Box plot for the x-direction.

(b) Box plot for the y-direction.

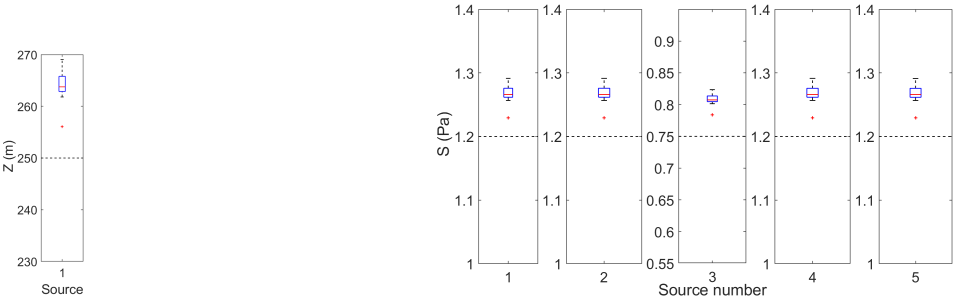

(c) Box plot for the z-direction.

(d) Box plot for the source strength.

Figure 6.24: Box plots of the source parameters for the simulated data set as found by GO with the CSM single frequency energy function when searching for a single aircraft height. The box plots indicate that the runs converge to nearly the same result, except for one outlier present in all box plots. The z is overestimated strongly.

7

Beamforming analysis on fly-over data

For these fly-overs an initial analysis using the spectrogram, PSD, and acoustic source maps is performed to assess the data.

This chapter contains the initial assessment of the fly-over data of the two selected fly-overs. There is already a good understanding of noise sources during landing based on the analyses of previous fly-over measurements, therefore it is easiest to start with an analysis of the A380. This is done in Section 7.1. After that, the take-off case is analysed in Section 7.2. Lastly, a more in-depth analysis of a low frequency noise source for take-off conditions is given in Section 7.3.

7.1. Beamforming analysis of an A380 landing

First, the spectrogram is inspected to get an idea of the noise sources or dominant tones that are present in the measurement. The spectrogram is presented in Figure 7.1. It appears that at low frequencies until 2000 Hz there is a high acoustic energy. Moreover, the fan tones are slightly visible in the spectrogram.

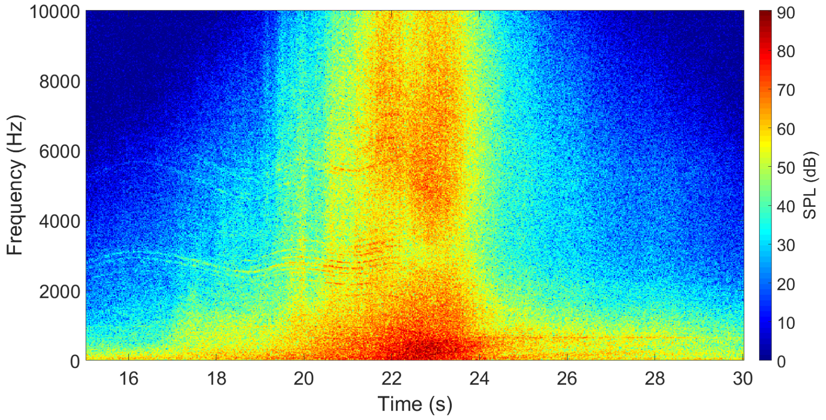

Figure 7.1: Spectrogram of an A380 during landing. The aircraft is overhead at 22.43 s. Noise in the lower frequencies up to 2000 Hz is dominant. Some fan tones are visible at higher harmonics.

To find out which aircraft components dominate the lower frequencies, an analysis is made with a semi-empirical aircraft component noise prediction method called ANOPP [38, 39]. For the noise prediction method the parameters in Table 7.1 and 7.2 are used. The results of the noise prediction method are shown in the ANOPP spectrum in Figure 7.2. The predictions are only presented for airframe noise. The coloured smooth solid lines represent different components while the black smooth solid line is the total of the individual sources. The measured PSD is also added to the spectrum for reference, this is the black fluctuating line. A comparison between the modelled and measured spectrum indicates that until 2000 Hz indeed mostly airframe noise is present with a contribution of around 10 dB/Hz maximum for remaining noise components in the measurement. The differences between the model and measurements are hypothesised to be due to the engines. In the model the main landing gear acts as dominant noise source. Above 2000 Hz, the model and measured PSD differ strongly due to the engine contribution which is clearly visible in the PSD as the increment above 3000 Hz. Thus the acoustic energy visible in the spectrogram above 3000 Hz is attributable to engine noise.

Aircraft type	**Height (m)**	**Speed (m/s)**	**Wing area (m^2)**	**Wing span (m)**	**Flap area (m^2)**	**Flap span (m)**
A380	50	66.5	753	80	103	42
B747-800	250	78.8	554	68.45	60.4	38.8

Table 7.1: ANOPP aircraft geometry parameters for an A380 and a B747-800 [30, 40, 41].

Aircraft type	**D_{tire} (m) MLG**	**#wheels/bogie (-) MLG**	**#bogies (-) MLG**	**D_{tire} (m) NLG**	**#wheels/bogie(-) NLG**	**#bogies (-) NLG**
A380	1.5	4	4	1.5	2	1
B747-800	1.245	4	4	1.245	2	1

Table 7.2: ANOPP aircraft landing gear parameters for the Main Landing Gear (MLG) and Nose Landing Gear (NLG) for an A380 and a B747-800 [30, 40, 41]. D_{tire} is the tire diameter of the landing gear tires.

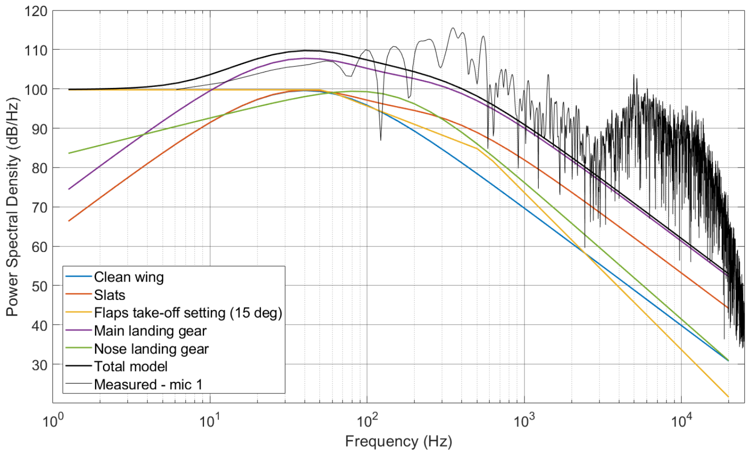

Figure 7.2: Comparison of the measured PSD with the semi-empirical ANOPP prediction model spectrum for an A380. The prediction model contains airframe noise components, which are the fluent lines. The black fluent line is the total modelled airframe spectrum. The black fluctuating line is the measured PSD. The parameters used for the prediction model are given in Table 7.1 and Table 7.2. A deviation between the modelled and the measured spectrum is caused by the engines. The main landing gear (purple) is the main airframe noise component according to the model.

To investigate further which sources are dominant (and thus should be found in the GO inversion) a CB source map is made. This is done at two frequency ranges: one where the airframe noise is expected to be present, and one where the engines are expected to be visible. To select which frequencies are most interesting for analysis, the information of the spectrogram, the measured spectrum, and the modelled spectrum is combined. CB is applied to a frequency band of 1000-2000 Hz (LF-band) and a band of 2500-4000Hz (HF-band). The lower bound for the Low Frequency (LF) is based on spatial resolution. Considering that the height is around 50 m according to ADS-B data of the OpenSkyNetwork [15], at this frequency the Rayleigh limit is 6.15 m which is sufficient to see the engines separately, but below that the spatial resolution becomes worse. The upper limit is set at the dip in the measured PSD from where on the engine noise becomes more important. For the limits of the High Frequency (HF) band, the decision was made based on the distance the aircraft moves during the time snapshot. For CB a time snapshot of 0.05 s was taken when the aircraft was overhead. As the aircraft is moving at a speed of 66.5 m/s [15], it displaces 3.3 m in this time. At the start of the band the Rayleigh limit is 2.46 m and thus the displacement could already be noticed. To minimise the source map deterioration yet trying to include the Blade Passing Frequency (BPF) tones visible in the spectrogram up to around 4000 Hz, the maximum frequency is 4000 Hz. The overhead time of the aircraft is 22.43

s, as determined through finding the maximum time-averaged pressure measured by the centre microphone. This is checked with the spectrogram and the video.

The steps for processing the data until a frequency domain pressure signal is achieved, are described in Appendix D. The CB method of Section 4.2 is applied, with incoherent summation and the SPL corrections for height and atmospheric attenuation. The meteorological conditions used can be found in Table A.1. Figure 7.3a shows the result of CB in the LF band. Figure 7.3b shows the results for the HF band.

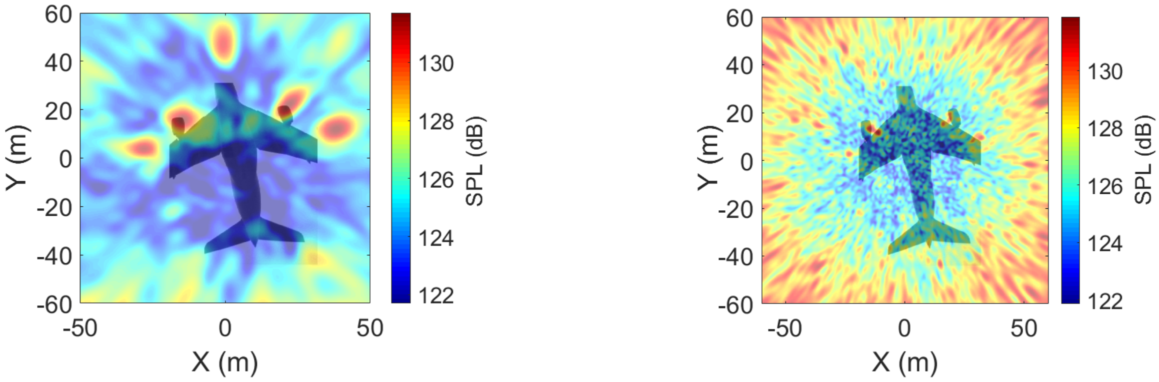

(a) Incoherent summation is applied over the LF band from 1000 to 2000 Hz.

(b) Incoherent summation is applied over the HF band from 2500 to 4000 Hz.

Figure 7.3: CB acoustic source maps at the LF and HF band for an A380 during landing. The aircraft height is taken from the ADS-B data at 50 m. An overlay from the video is applied, but the wings of the A380 do not fully fit. For the LF band the engines as well as the nose landing gear are clearly visible. The main landing gear is only lightly visible. For the HF band only the engines are visible.

For the LF band the four engines are visible as well as the nose landing gear. Although only slightly visible, it seems that the main landing gear sources are present as well in between the two inner engines. The expected small contribution of engine noise in the LF band according to Figure 7.2, is thus larger, with the engines dominantly visible. Surprisingly, the nose landing gear appears as a strong noise source although the ANOPP model predicts that the main landing gear is the main noise component in the low frequency range.

For the HF band, only the engines appear, which is as expected for this frequency band. The CB source map suffers from a high number of side lobes at the scan plane edges.

7.2. Beamforming analysis of a B747-800 taking-off

For the analysis of take-off measurements, the same procedure is followed as for the analysis of the landing fly-over measurement. A B747-800 fly-over during take-off was selected for which the spectrogram is shown in Figure 7.4. It strikes immediately that the fan tones are strongly visible here. Also at the overhead time a very strong tone appears at a frequency of 680 Hz. This is equal to the BPF for a B747-800 with GEnx-2B67 engines, when a thrust setting of 80% is used [42–44]. Although this seems low for a thrust setting during take-off conditions, analysis by [45] shows similar thrust settings are used by pilots.

Up to 1500 Hz, high acoustic energy is seen. However, unlike at the landing measurement, here around 1500 Hz the engine contribution is already present. This last statement can be deduced from the ANOPP prediction in Figure 7.5. For the calculations of the prediction model the parameters in Table 7.1 and 7.2 are used. As with the spectrum shown for the landing A380, the total model is presented by the black smooth line and the measured spectrum is represented by the black fluctuating line. The measured spectrum shows, at lower frequencies, a 10 dB/Hz to nearly 15 dB/Hz deviation from the modelled spectrum which is caused by the engine contribution. From the modelled airframe noise spectrum the main landing gear is expected to be dominant in the airframe noise contribution.

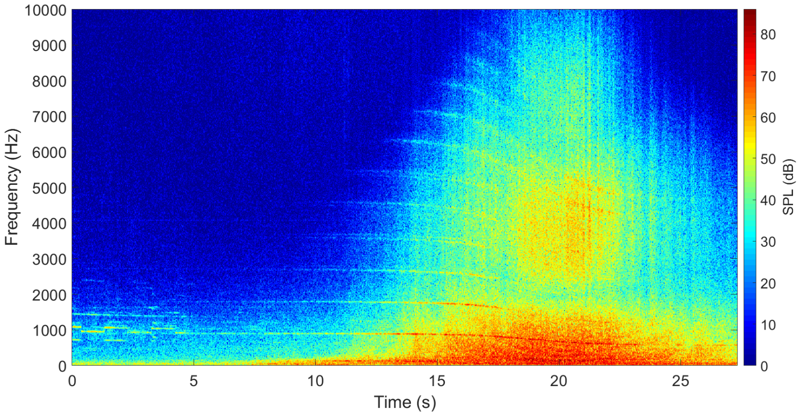

Figure 7.4: Spectrogram of a B747-800 during take-off. The aircraft is overhead at 19.96 s. Noise in the lower frequencies up to 1500 Hz is dominant. A very strong tone is visible at a low frequency, at the overhead time at 680 Hz. The fan tone and its harmonics are clearly visible.

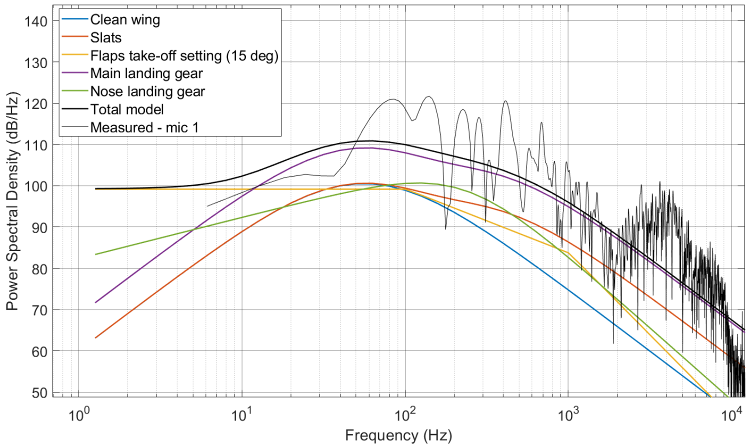

Figure 7.5: Comparison of the measured PSD with the semi-empirical ANOPP prediction model spectrum for a B747-800. The prediction model contains airframe noise components, which are the fluent lines. The black fluent line is the total modelled airframe spectrum. The black fluctuating line is the measured PSD. The parameters used for the prediction model are given in Table 7.1 and Table 7.2. A deviation between the modelled and the measured spectrum is caused by the engines. The main landing gear (purple) is the main airframe noise component according to the model.

Also for the take-off, CB source maps are analysed as those give a quick insight in the dominant sources and the lay-out of the sources. Again, two frequency bands are selected from the spectrogram and spectrum. The LF band is selected to range from 1000 to 2000 Hz and the HF band from 2500 to 5000 Hz. A snapshot of 0.05 s is taken around the overhead time of 19.96 s. The height of this fly-over is around 250 m according to ADS-B data of the OpenSkyNetwork [15]. As the range for which the sources can be discriminated (according to the Rayleigh limit) is proportional to height, the spatial resolution decreases strongly with respect to the landing A380 as already deduced from Figure 3.3. At a frequency of 1000 Hz the limit is 30.77 m, at 2000 Hz this is 15.38 m, and at 5000 Hz it is 6.15 m. Thus, for a large part of the LF band, the sources are overlapping which is exactly why GO with the CSM energy function could later provide additional value. The limits of the HF band are determined by the high increment in Figure 7.5. Here the engines are expected to be dominantly visible. The upper limit of 5000 Hz is chosen as above that no additional information is expected on the engines, while it would add computational time. Figure 7.3a shows the result of the CB for the LF band, where Figure 7.3b shows this on the HF band. For these figures, the same data processing steps are applied as at landing and also incoherent summation with the SPL corrections is used. The acoustic source map is overlaid with the video and thus the aircraft is seen from below.

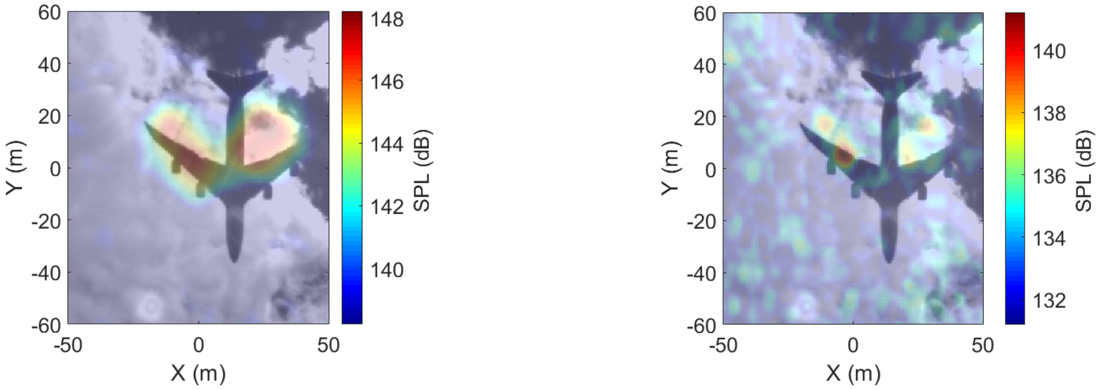

(a) Incoherent summation is applied over the LF band from 1000 to 2000 Hz.

(b) Incoherent summation is applied over the LF band from 2500 to 5000 Hz.

Figure 7.6: CB acoustic source maps at the LF and HF band for a B747-800 during take-off. The aircraft height is taken from the ADS-B data at 250 m. An overlay from the video is applied, but the source locations and the video do not match perfectly. For the LF band no separate sources are visible, but two high energy fields can be seen. On the right side higher acoustic energy is seen behind the wing. For the HF band, the four engines are separately visible although the locations do not match the video.

As can be seen, especially on the right side of the LF source map, is that the noise source is behind the engine. Left and right are here defined with respect to the source map for clarity. On the right side the high acoustic energy area seems more spread. The nose landing gear is not visible due to the dominance of the engines. In the HF source map, the engines are separately visible. However, here the location seems even more shifted than at the LF source map. Currently it is unknown whether this is caused by an incorrect match with the optical camera or that the sources are really located here. A deviation could also be caused by assuming a wrong height of the aircraft for the scan grid positions.

Lastly, the tone of 680 Hz is inspected. As this is at a low frequency, with a wide main lobe, the CB source map does not give specific information on the source location as seen in Figure 7.7a. FB can provide more information on the location of the source and is applied for this case with a functional exponent of $\nu = 10$. A higher exponent does not result in a more accurate location, but does introduce sources at locations far outside the aircraft that are not visible in a CB source map. The FB source map shows a source close to the left outer engine, see Figure 7.7b. The FB source map does not show with certainty that the noise source is an engine. However, as seen in Figure 7.6 the engine sources seem to be placed slightly outside and after the engine. Thus the tone at 680 Hz is still hypothesised to be at the left outer engine.

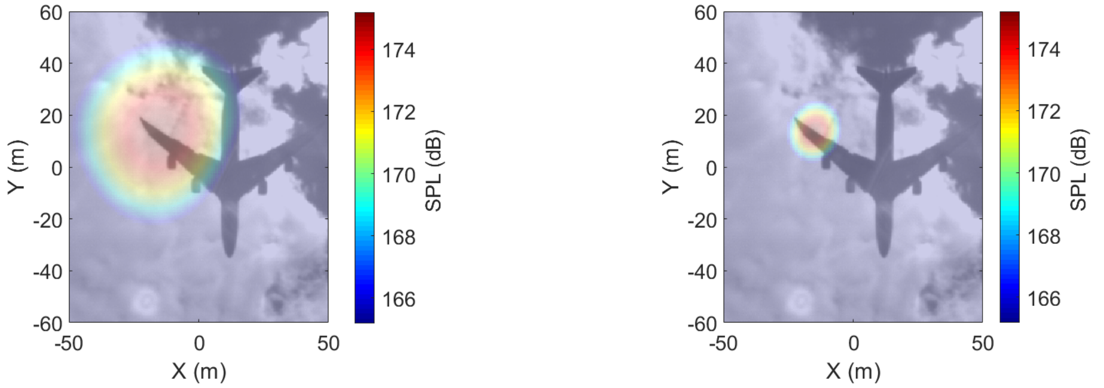

(a) CB acoustic source map.

(b) FB acoustic source map with functional exponent $\nu = 10$.

Figure 7.7: CB and FB acoustic source maps of a B747-800 during take-off at a tone of 680 Hz. The SPL values for FB are corrected according to Section 4.3. The CB source map shows a larger field, but seems to focus on the left most engine. The FB source map shows a location on the wing, very close to the engine.

Also higher harmonics of the tone have been analysed. The clearest tones have been selected from the spectrogram, which are at a frequency of 1331 Hz and 4834 Hz. For these tones the FB source maps are presented in Figure 7.8a and 7.8b respectively. Note that for the tone of 4834 Hz a functional exponent of $\nu = 5$ is chosen, instead of $\nu = 10$. A higher exponent did not result in a clearly visible source location.

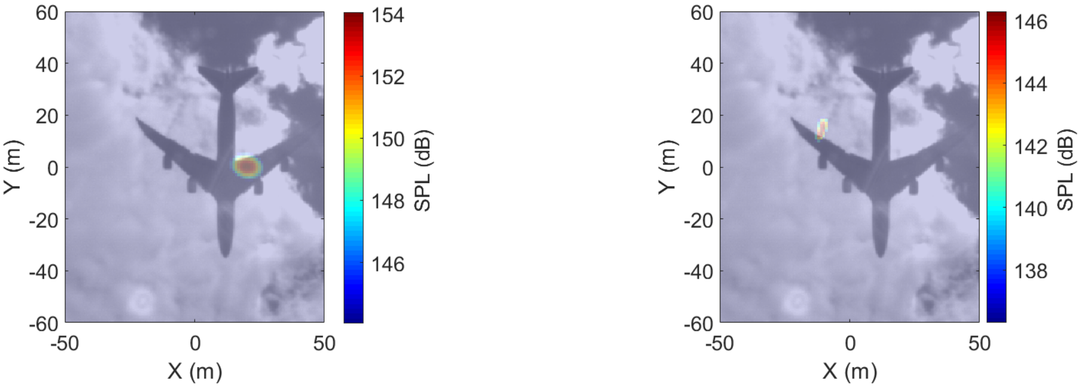

(a) FB acoustic source map for a frequency of 1331 Hz, with functional exponent $\nu = 10$.

(b) FB acoustic source map for a frequency of 4834 Hz, with functional exponent $\nu = 5$.

Figure 7.8: FB acoustic source maps of a B747-800 during take-off for a tone of 1331 Hz and 4834 Hz. The SPL values for FB are corrected according to Section 4.3. At 1331 Hz the right inner engine causes the strong tone. At 4834 Hz the outer left engine causes the tone, similarly to the tone at 680 Hz.

For a frequency of 1331 Hz, the right inner engine is found as source. For a frequency of 4834 Hz the left outer engine again is found as source. Thus, these fan tones can clearly be linked to the engines.

7.3. Low frequency noise source occurring during take-off

This part of the research is not part of the assessment of the data leading up to an analysis with GO. This side-step was executed to investigate unexpected sources in the basic analysis of take-off fly-over measurements.

During data processing of fly-overs it appeared that for landing fly-over measurements hardly any spectral leakage was present. Thus no weighting had been applied on the time snapshot. However during an initial CB analysis of the first take-off measurements (for which a B737-800 was selected), a source appeared consistently at position (0,0) in the HF source map which overpowered largely the other sources. Using the same conditions at landing measurements did not result in such a strong source at location (0,0). When Hanning weighting was applied on the data, this source disappeared and the expected sources were visible. As weighting is applied to solve spectral leakage, this could indicate that a strong low frequency source leaks into higher frequencies. As the effect was not expected to be so strong, several checks have been performed.

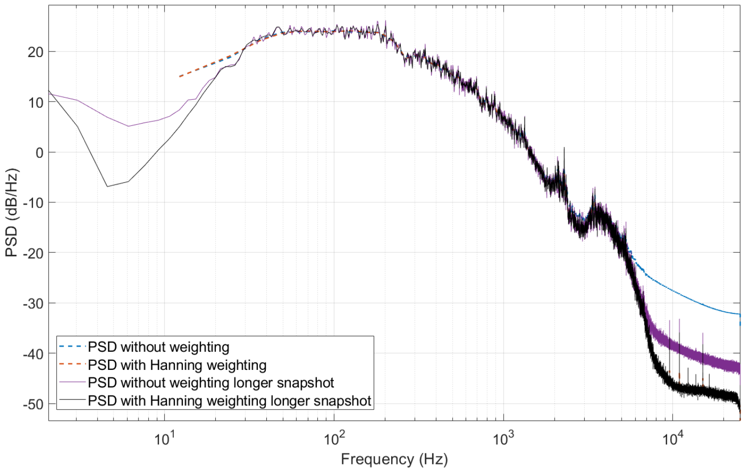

Figure 7.9: PSD for a B737-800 around the overhead time. The effect of Hanning weighting on the signal is investigated by comparing the PSD without weighting, with weighting, and with a longer snapshot. The results for the PSDs with Hanning weighting overlap. At high frequencies a deviation of nearly 20 dB is seen for the short time snapshot with and without Hanning weighting.

Firstly, the PSD was checked to see what the difference between no weighting and Hanning weighting is. Per standard, the snapshot taken to compute the PSD is 0.05 s around overhead time. When the snapshot is lengthened to 0.5 s, spectral leakage is reduced. This is caused by the relation of the size of the main lobe width to the length of the snapshot, which is $1/T$. Hence the main lobe width is decreased with a longer snapshot. The side lobes are then also closer to the main lobe and will decay faster than with a broader main lobe. The spectrum with a longer snapshot thus resembles more closely the real spectrum. The PSD with longer snapshot is added for comparison, although it overlaps in Figure 7.9 with the Hanning weighted PSD. In reality it is not convenient to use such a large snapshot as the aircraft will fly a larger distance than the spatial resolution, resulting in unclear sources. In Figure 7.9 the spectrum is shown for a Boeing 737-8.

From Figure 7.9 it is clearly visible that at frequencies above 5000 Hz a strong difference occurs with a higher energy for the spectrum without weighting, thus indicating indeed spectral leakage. This behaviour was then checked for a large part of the data set, by analysing the difference between the PSD with and without Hanning weighting at 7000 Hz. Table 7.3 gives the respective results. The A380, B747-800, B777-200ER, B777-F1, B787-9, and B787-10 do not seem to have this strong frequency leakage above 7000 Hz. However, for some aircraft types only a few measurements are available and therefore it is not possible to say with certainty that they do not suffer from this.

Type	Total	Strong spectral leakage
A319-100	10	10
A320-200	27	25
A320-neo	1	1
A321-100	1	1
A321-200	9	8
A330-200	8	6
A330-300	5	2
A380	1	0
B737-524	1	1
B737-700	18	11
B737-800	51	27
B737-900	7	4
B747-400	3	1
B747-800	1	0
B767-300	2	2
B777-200er	1	0
B777-200lr	2	1
B777-300er	3	2
B777-F1	4	0
B787-9	2	0
B787-10	1	0
CRJ-7	4	4
CRJ-9	1	1
ERJ175	30	28
ERJ190	26	25
ERJ195	4	3

Table 7.3: Aircraft types that need Hanning weighting on data due to extreme spectral leakage. The total gives the number of measurements of that type analysed, while the other column gives the number of aircraft which needed the weighting applied. Overall, most aircraft types seem to suffer from the strong spectral leakage. For the types that do not need Hanning weighting, there are too few measurements to be certain.

To see if this behaviour could indeed be caused by low frequency noise of the aircraft, the location of a potential source is sought. For this, the acoustic data is filtered on a frequency band by applying a Buttersworth filter. In one frequency band from 50 to 400 Hz it can be seen that there is indeed a pressure wave passing over the array, see Figure 7.10.

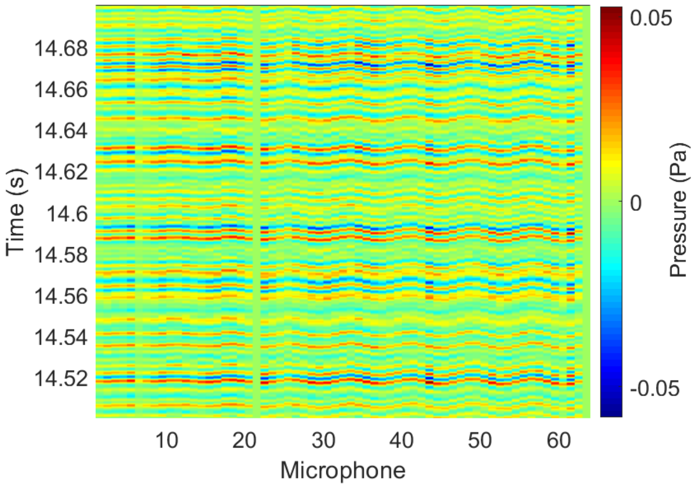

Figure 7.10: Microphone output in pressure over time for a frequency band of 50 to 400 Hz. The red line indicates that a high pressure wave is arriving at that point in time at a certain microphone. For this frequency band a wave over the array is visible, as the wave does not arrive at all microphones at the same time. As it occurs repeatedly over time, a source should cause this.

For the frequency band from 50 to 400 Hz, an beamforming analysis over multiple snapshots has been performed. At these low frequencies it is not possible to determine the exact location of the source, but the source maps can show the behaviour of the source. Three snapshots are selected, one at overhead time, one 0.5 s before overhead time, and one 0.5 s after overhead time. The CB source maps from the snapshots are presented in Figure 7.11.

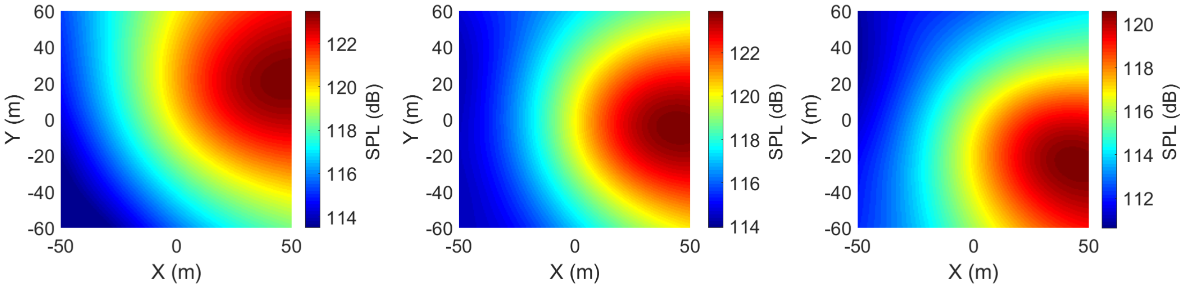

(a) Snapshot 0.5 s before overhead time.

(b) Snapshot at overhead time.

(c) Snapshot 0.5 s after overhead time.

Figure 7.11: CB source maps for three snapshots: before, at, and after overhead time. It is visible that the source moves towards the negative y-direction.

Figure 7.11 shows that the source moves towards the negative y-direction over snapshots. For take-offs it is known that the aircraft travels in negative y-direction over the array, see also Section 7.2. This confirms that the source moves along with the aircraft and is thus caused by the aircraft.

Moreover, applying a Buttersworth band-pass filter from 400 Hz to 11 kHz and then applying beamforming, without applying Hanning weighting, results in a clean source map without the source at (0,0). The high noise below 400 Hz (stemming from the aircraft) is thus causing the spectral leakage and needs to be eliminated when analysing the high frequency data.

Lastly, to confirm that this source from 50 to 400 Hz is capable of causing such strong spectral leakage above 5000 Hz and overshadow other sources there, a simulation was carried out. This simulation consists of a strong signal spread over the 50 to 400 Hz band and a much weaker signal of 6500 Hz. Figure 7.9 shows the PSD of the signal is 40 dB higher at the low frequencies than at 6500 Hz. This is a factor 100 difference which is indeed the situation simulated. The PSD of this model is shown in Figure 7.12 where the signals are shown separately (magenta for the low frequency signal and red for the high frequency signal) and combined (blue line). Without weighting it is visible that the side lobes of the low frequency signal are still very dominant at high frequencies. When this graph is zoomed at a frequency of 6500 Hz, see Figure 7.13, it is visible that the combined signal (blue) is still largely influenced by the low frequency signal when no weighting is applied. The low frequency signal side lobes are still very strong at higher frequencies, only 5 dB lower than the high frequency signal. In both plots it is visible that this is fully resolved when applying Hanning weighting.

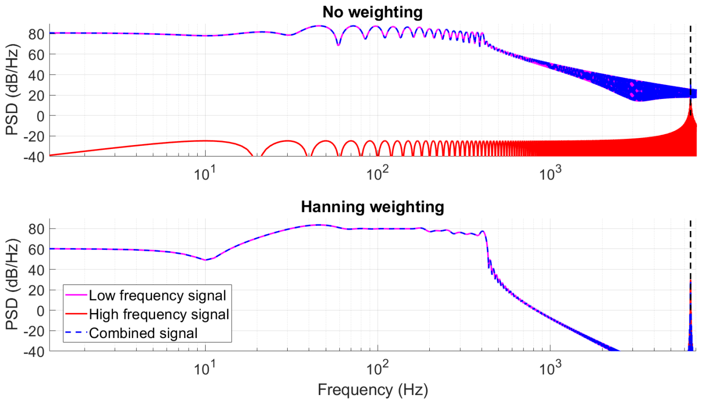

Figure 7.12: PSD of the simulation of a low frequency noise with high acoustic energy. The low frequency source is presented in magenta, the high frequency tone in red, and the combined signal in blue. The spectrum is shown with and without Hanning weighting to see the impact of Hanning weighting for a strong low frequency noise. Without weighting, the side lobes of the low frequency source are still significant at the high frequency source.

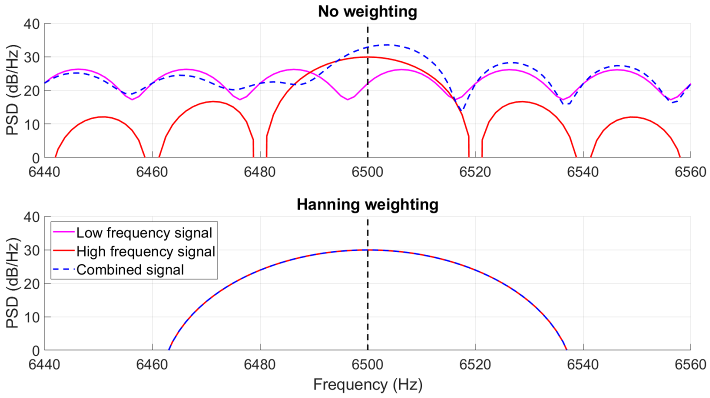

Figure 7.13: A closer view of the PSD from Figure 7.12 around the high frequency of interest to better observe the impact of weighting. Without weighting, the side lobes of the low frequency source (magenta) clearly have a large impact on the total spectrum (blue). The level is higher than that of the high frequency tone and also the peak is shifted, giving the wrong frequency indication of the high frequency source. With Hanning weighting, the total spectrum at high frequency is the same as that of the high frequency source.

With the above checks of applying a band pass filter, applying GO cross-checked with CB, and performing a check with simulated data, it is concluded that this behaviour is caused by very strong spectral leakage from a low frequency source. The question arises what type of source is causing this. The outdoor microphone array does not have the spatial resolution to separate sources at such low frequencies at take-off heights, thus no exact location will be visible in acoustic source maps. However, from the circumstances at which this artefact is found, a first deduction is possible. It occurs in take-off circumstances and not during landing, which directs the search to engine noise as the engines are turning idle during landing. Research by [46] shows numerically that interference of the jet stream with the trailing edge of the wing, causes a 13 dB PSD increase at lower frequencies. Although it is out of scope of this research to investigate whether this is the case for the behaviour seen here, it is an interesting theory.

8

Performance of GO on fly-over data

In this chapter, the performance of GO on the two cases from Chapter 7 is tested. Similar to the previous chapter, first the landing aircraft is analysed in Section 8.1. In Section 8.2 the take-off aircraft is analysed with GO. However, first the scope of the analysis with GO is set out.

For the data analysis with GO the main interest is in the LF band, as this is where most sources (thus most information) can be found and where CB has difficulties in revealing closely spaced sources. As multi-frequency analysis did not give as good results as a single frequency analysis with the simulated data set in Section 6.3, it is chosen to analyse a range of frequencies one by one. Combining the final results of each frequency could give more information again. The frequencies in the one-third octave band 31 will be analysed. This band runs from 1120 Hz to 1410 Hz, in steps of 20 Hz, and is a good representation of the LF bands shown in the previous sections. This frequency range allows for two things:

1. For a landing fly-over measurement the Rayleigh limit on this frequency range is low. As can be seen in Figure 7.3a the engines, nose landing gear, and slightly the main landing gear are identifiable. Thus, with the landing measurement case the ability of GO to find the aircraft height and closely spaced low frequency sources in experimental field data is tested.

2. For a take-off fly-over measurement, at this frequency range CB suffers from the Rayleigh limit preventing the imaging of individual noise sources. In Figure 7.6a there exist two high acoustic energy fields which both most likely contain multiple sources. This case is thus ideal to test the ability of GO to find sources under the Rayleigh limit in the experimental field data.

Further, although results of the simulation analysis show otherwise, GO with neither the BF nor the CSM energy function is able to converge for the z-location on fly-over data. The algorithm steers always entirely to the z-boundaries, dominantly the lower boundary, even when the boundaries are expanded. The anechoic room case already slightly hinted that finding different z-locations is difficult at lower frequencies. For the take-off case this can be explained by the fact that the source is in the far-field and thus the z-location cannot be well estimated. However the landing case is in the near-field and thus the z-location was expected to be found. However, the anechoic room case and the simulation case both have a high SNR, which is not the case for outdoor fly-over measurements where wind or background noise could cause disturbance. This could explain why more difficulty in finding the z-location is seen for the fly-over measurements. To discard the problem, the algorithm was set to search for a single height. As the simulation analysis for a single height (Section 6.4) made clear that with the CSM energy function the height is not correctly determined, the data set is analysed for height with the BF energy function first. Also the simulation analysis showed that under the Rayleigh limit the BF energy function will not find any of the sources, but it will still find the correct height of the strongest sources. The height found with the BF energy function will serve as input for GO with the CSM energy function, which will thus only search parameters (x, y, s) per source.

Lastly, using the same setting parameters as for the simulated data set it is hardly possible to cover a range of frequencies due to the high computational time of 8 hours per frequency. Therefore, the number of population members (q) has been reduced from 128 to 64. The minimum setting for q that still allows good convergence is disputed in literature. An extensive review by [47] showed that q is often used anywhere between 1 and 40 times the amount of search parameters. Setting q below 50 is however not recommended. Also for large-dimensional problems with 30 to 50 search parameters anywhere between 3 to 5 times the amount of parameters is advised [47]. In this part of the research the number of search parameters is 22 at most (for 7 sources find x, y, s and once find z). Thus, setting q at 64 is deemed in line with the review. The following GO setting parameters per frequency are used:

- $q = 64$
- $N_{gen} = 2000$
- $N_{runs} = 10$
- $p_c = 0.75$
- $F = 0.4$

8.1. GO analysis of an A380 landing

To analyse the data with GO, search zones need to be applied. For that, the CB source map from Figure 7.3a is used. A selection of seven sources has been made: the four engines, the nose landing gear, and two sources for the main landing gear. Around these locations a broader search zone of 10 by 10 m is defined. With this, the GO analysis is initiated.

The results of the analysis of GO with the BF energy function to search the height, showed an average height of 53.78 m with a standard deviation of 8.59 m. The large deviation does introduce uncertainty and therefore the height is analysed via a weighted histogram. For a single frequency the minimum energy of the best run is divided by the energy per generation. Thus, when the energy of the solution is lower, indicating a better candidate solution, the fraction is higher. With this, a weighted histogram can be constructed where the z-location of a good solution is given a higher impact than that of a lesser solution. This is repeated for all frequencies and combined in the weighted histogram of Figure 8.1. The highest bar is expected to represent the best z-location.

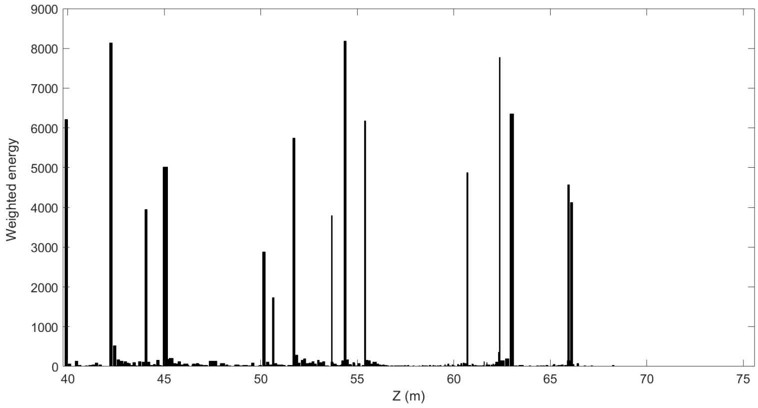

Figure 8.1: Histogram of the estimated height for an A380 during landing. The height estimates are taken from the best results per frequency analysed by GO with the BF energy function searching for a single height. The results are weighted by their energy. A lower energy means a better result, and thus a higher value in the histogram. The histogram shows the best aircraft height at 42, 54, and 63 m.

The histogram in Figure 8.1 shows many peaks. This is unexpected but can be due to the fact that a bad solution for z can be compensated by good estimates for x and y. Although this weighted histogram is not ideal, it gives a first indication that the best z-location is either at 42 m, 54 m, or 63 m. To find out whether one of these heights could indeed be the aircraft height, a geometry check is performed. Thus, the distance between the locations of the engines in a CB source map is computed. For an A380, the inner engines are 29.6 m apart and the outer engines are 51.4 m apart. The distance between the nose landing gear and the main landing gear should be 27.6 m [26]. At a height of 42 m the engines are too close together, at 63 m they are too far apart. Around 54 m the engines are also too far apart. Thus, the weighted histogram does not help in finding z. Therefore an extensive search has been done with CB source maps on different scan planes. It was concluded that for a height of 50 m the engine locations match best with reality. This is the same aircraft height as is used for the CB figures (Figure 7.3a and 7.3b) earlier. Thus an aircraft height of 50 m served as input for GO with the CSM energy function.

Table 8.1 contains the mean and standard deviation of the best solutions per frequency of GO with the CSM energy function. These values indicate the average location of a source over the frequency band. The standard deviation for the x- and y-location is within 4.3 m which indicates that the source location found per frequency is relatively stable. However, the source strength deviates up to half the mean source strength. This can be explained by looking at source maps of a single frequency within the band. Not all sources are visible at each frequency. As the simulation analysis proved, when searching for a non-existent source the GO algorithm with the CSM energy function tends to find sources at a low source strength.

Source	**1**	**2**	**3**	**4**	**5**	**6**	**7**
x **(m)**	-30.1 ± 3.72	-16.9 ± 2.44	1.05 ± 2.44	13.4 ± 2.08	21.3 ± 2.52	-0.56 ± 1.52	1.73 ± 1.71
y **(m)**	7.51 ± 3.81	15.1 ± 1.91	39.1 ± 4.25	10.9 ± 2.63	1.0 ± 2.80	7.70 ± 2.98	7.71 ± 3.07
s **(Pa)**	2.99 ± 1.19	3.53 ± 1.39	2.29 ± 0.56	3.08 ± 1.20	3.00 ± 1.11	3.77 ± 1.68	3.82 ± 1.66

Table 8.1: Mean and standard deviation of the best source parameters over the frequency band as found by GO with the CSM energy function for an A380 in landing. The height of the aircraft was fixed at 50 m and thus is not a parameter in the table. For the source strength large deviations of its mean are seen. This is due to sources not being equally strong at every frequency. Source 3 corresponds to the nose landing gear, while sources 6 and 7 correspond to the main landing gear.

The mean and standard deviations can also be presented in histograms per parameter. This gives more clearly an indication of which locations and source strengths are found amongst the best solutions over the frequency band. The histograms for the x- and y-location as well as the source strength are presented in Figure 8.2. The higher the bar, the more often that location is found over the frequencies. For the x-location clearly a source between -18.5 and -16 m is visible. Also a source between -0.1 and 1.1 m is seen, this is the nose landing gear. Also between 13.4 and 14.7 m and 22.0 and 23.3 m two x-locations are found more often. For the y-location sources are found multiple times between 0.3 and 1.3 m, which corresponds most likely to the two sources of the main landing gear. Also between 7.3 and 8.3 m and 13.3 and 14.3 m sources are found often. However, there is a higher spread around the bars than for the x-location histogram. For the source strength, very clearly the highest source strength of 5 Pa is found. This is due to the fact that both sources of the main landing gear have this source strength for GO. From the source strength histogram it is concluded that there is quite a spread for source strength for the other sources.

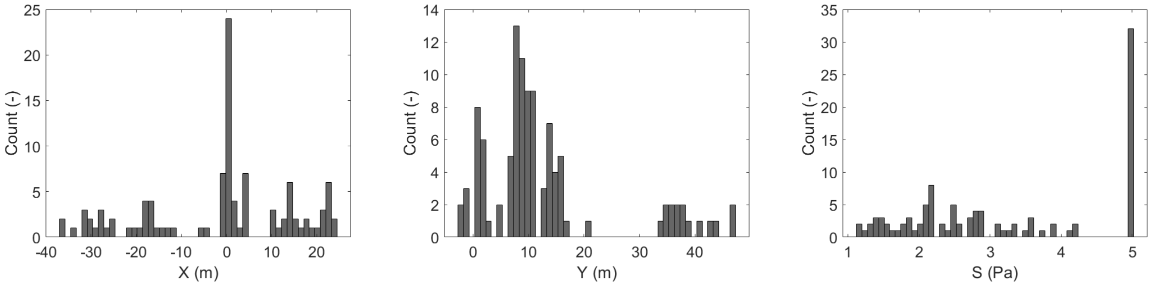

(a) Histogram for the x-location.

(b) Histogram for the y-location.

(c) Histogram for the source strength.

Figure 8.2: Histogram plots for the source parameters found by GO for an A380 in landing. Dominantly found is the nose landing gear at x = 0 m. Also the source strength of the two main landing gear sources is found dominantly at s = 5 Pa.

The locations in the table and histogram plots give an indication whether the same locations are found multiple times. However, they do not give an indication whether the source is correctly found. Therefore, acoustic source maps are constructed which give a visual insight. From the frequency range, only for one frequency the results are presented in Figure 8.3. The other frequencies have been analysed as well, but will not be presented here to keep the report concise. For clarity a frequency is chosen for which the figures do not show too high side lobe levels. Figure 8.3 is built up out of three separate acoustic source maps. In all figures of Figure 8.3 the location of the sources found by GO are indicated with black and white stars. The colour of the star is chosen based on the clarity with respect to surrounding colours, it has no meaning.

- Figure 8.3a shows an acoustic source map of the full one-third octave band 31 generated with the standard CB algorithm, this is essentially the same as the source map in Section 7.1. Note that although the same CB algorithm is used as in the previous sections, the levels displayed here are different. The reason for this is that in the GO post-processing the SPL is presented without the height and attenuation correction from Equation 4.10.

- Figure 8.3b gives the CB source map for solely the frequency of interest (1300 Hz), while Figure 8.3a, described in the previous item, gives an indication of the sources present in the full band. Here a high number of side lobes can be seen that are not visible in Figure 8.3a as they are averaged out for the band with incoherent summation.
- Figure 8.3c is also a source map generated with the CB algorithm for a frequency of 1300 Hz, but the CSM is constructed differently. For the first two images, the CSM is generated with measurement data as explained in Section 4.2. For the last image the CSM is constructed based on the sources found by GO. Hence $\boldsymbol{C}_{model}$ of Section 4.4.2 is used. The source strength found by GO is included the $\boldsymbol{C}_{model}$ used for Figure 8.3c and thus is only represented in the last figure.

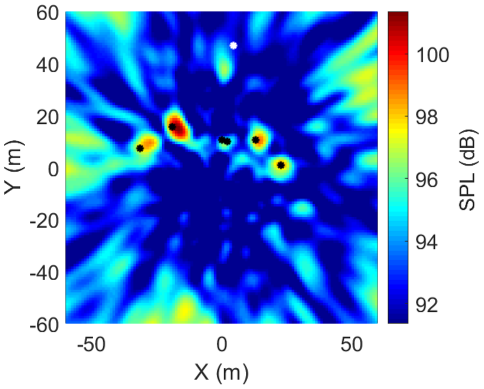

(a) CB source map for one-third octave band 31.

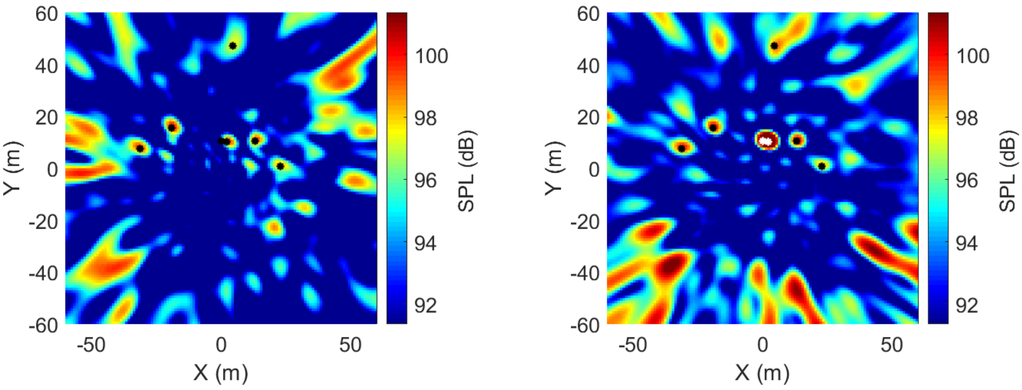

(b) CB source map for a frequency of 1300 Hz.

(c) CB source map for a frequency of 1300 Hz with the GO results at the same height as CB.

Figure 8.3: CB acoustic source maps to represent the sources found by GO with the CSM energy function for the A380 in landing at a frequency of 1300 Hz. All source maps use the same colour scale. The first two figures are constructed with measurement data with the source locations found by GO plotted on top in dots. The last figure is constructed with a CSM based on the parameters found by GO. The source locations found by GO are correct. However, the source strength for the landing gear is strongly overestimated.

From Figure 8.3a is concluded that the algorithm is able to find the engine locations and the main landing gear, but is slightly off for the nose landing gear. By inspecting Figure 8.3b it is clear that GO did find the highest acoustic energy locations for this specific frequency. Thus it provides a good match for frequency 1300 Hz, but deviates from the average location of the source over the band. From the first two figures, only a conclusion on the source location found by GO can be drawn, for the conclusion on the source strength Figure 8.3c is needed which should be compared to Figure 8.3b. Figure 8.3c shows that the source strength around the main landing gear location is overestimated strongly. Perhaps this is caused by a compensation of the too high z (landing gear are expected 5 m lower than the engines) for a higher s. This causes a slightly different side lobe pattern with respect to Figure 8.3b. To conclude this analysis, it appears that the the locations found are correct, but that the source strength is overestimated for the main landing gear.

As seen in the analysis of simulated sources in Chapter 6, the algorithm has not always converged within 2000 generations. In that case the final solution might not be the best solution the algorithm can find. Therefore, convergence plots of the algorithm at a frequency of 1300 Hz have been added, see Figure 8.4. The algorithm converged within 250 generations thus here the final solution is the best GO can find. The convergence plots also show that only the nose landing gear (yellow) goes to the upper boundary for the x- and y-direction. Furthermore the red line representing a source of the main landing gear goes to its source strength upper boundary. Note that z is constant as it is at a fixed height. The fast convergence indicates that F could be set larger and p_c smaller to explore the search space more. This gives a slower convergence, but might improve the result for s.

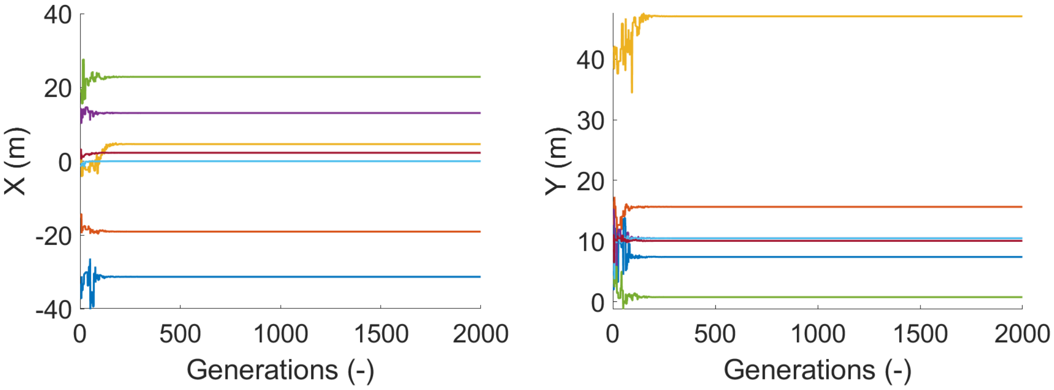

(a) Convergence for the x-direction.

(b) Convergence for the y-direction.

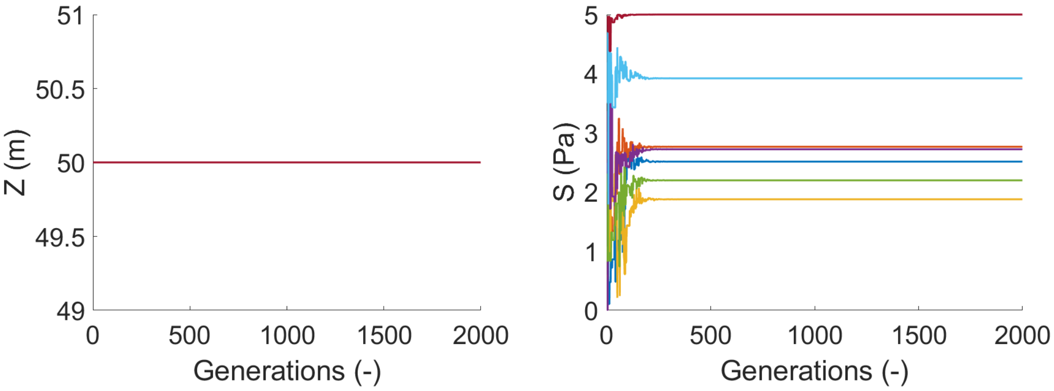

(c) Convergence for the z-direction.

(d) Convergence for the source strength.

Figure 8.4: Convergence plots of the source parameters for the A380 in landing as found by GO with the CSM energy function for a frequency of 1300 Hz. Each colour represents the same source in all convergence plots. Seven sources are searched for in this data set. Convergence is achieved in 200 generations, however, for some sources the boundaries are found.

It is concluded that for the landing case GO is not able to find the correct source height, but it is able to find the correct source locations when the height is fixed. Additionally, GO is able to determine correctly the source strength of the engines, but overestimates the source strength of the landing gear.

8.2. GO analysis of a B747-800 taking off

The search zones for GO need to be defined to start the analysis. However for the low frequencies analysed with GO (1120 Hz to 1400 Hz) the CB source map does not show separate sources. Therefore, the search zones have been defined based on the HF band source map from Figure 7.6b. Although only the engines are visible in Figure 7.6b, an estimation has also been made for the location of the nose landing gear. Lastly, an extra source seems to be present (on the aircraft wing in the optical picture). For this, also a search zone is added. Thus, in total six sources are searched for the B747-800 take-off case: three for the engines on the left side, two for the engines on the right side, and the last one for the nose landing gear.

The analysis of GO with the BF energy function over the frequency range showed an average height of 246.69 m with a standard deviation of 18.08 m. This is a very large deviation and thus similarly to the landing case the weighted histogram is constructed, see Figure 8.5.

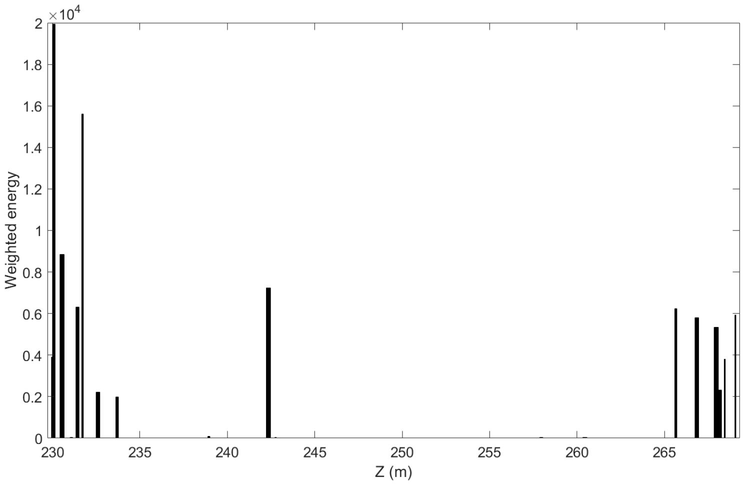

Figure 8.5: Histogram of the estimated height for a B747-800 during take-off. The height estimates are taken from the best results per frequency analysed by GO with the BF energy function searching for a single height. The results are weighted by their energy. A lower energy means a better result, and thus a higher value in the histogram. The histogram shows the best aircraft height at 230 m, but also gives a high value at 243 m and above 265 m.

The histogram in Figure 8.5 shows especially good z-candidates at the search boundary of 230 m. It further shows a peak between 265 and 270 m. Although the analysis of simulated data indicated that the height could still be found in the far-field, this is not supported by the results of the fly-over data. When at h = 230 m and h = 270 m source maps are constructed, it becomes clear that the engine sources are not at the correct distance with respect to each other. The inner engines should be 25 m apart and the outer engines should be 45 m apart [27]. For a height of 230 m they are too close together, for a height of 270 m they are too far apart. According to the histogram, the aircraft could also be at a height of 243 m. However, this did not result in the correct aircraft geometry as the engines are too close together. Again a source map has been made with CB for several heights which showed that 260 m could be the correct aircraft height. With this height, the GO algorithm with the CSM energy function is initiated over one-third octave band 31.

Table 8.2 gives the mean and standard deviation of the best results over the frequencies. It is visible that the source strengths are higher than those for the landing, which is as expected especially for the engines. The sixth source is the nose landing gear, for which a large standard deviation in y is seen.

Source	**1**	**2**	**3**	**4**	**5**	**6**
x **(m)**	-29.5 ± 3.95	-25.9 ± 3.62	-19.5 ± 4.08	6.13 ± 3.59	9.99 ± 3.80	-17.4 ± 1.84
y **(m)**	16.7 ± 3.17	4.23 ± 5.33	11.5 ± 3.43	10.8 ± 4.73	13.4 ± 4.92	-18.3 ± 6.39
s **(Pa)**	4.47 ± 2.82	4.71 ± 2.35	5.43 ± 2.20	5.10 ± 2.15	5.50 ± 1.61	1.51 ± 0.92

Table 8.2: Mean and standard deviation of the best source parameters over the frequency band as found by GO with the CSM energy function for a B747-800 in take-off. The height of the aircraft was fixed at 260 m and thus is not a parameter in the table. For the source strength deviations up to half its mean are seen. This is due to sources not being equally strong at every frequency. Source 6 corresponds to the nose landing gear, the other sources correspond to the engines.

Next to the means and standard deviations per source parameter over the frequencies, also the histograms for $x, y,$ and$s$ are presented, see Figure 8.6. There are seven peaks visible for the x-location, while six sources are searched. From -30 to -15 m for x several sources are found often. From -15.4 and -14.4 m, as well as from 9.4 to 10.4 m two sources are found. Both should correspond to engine locations. In the histogram plot for the y-location all the negative y-locations are options for the nose landing gear. The nose landing gear location is thus hard to find. The engines seem to be located between 9.3 and 10.3 m, between 13.3 and 14.3 m, or between 19.3 and 20.3 m. Lastly the source strength histogram shows that for nearly all sources the maximum source strength of 7 Pa is found. This however does not correspond to the mean and standard deviation in Table 8.2 where the mean of the source strength is around 5 Pa for most sources. Thus, for each location a very high and very low source strength are found.

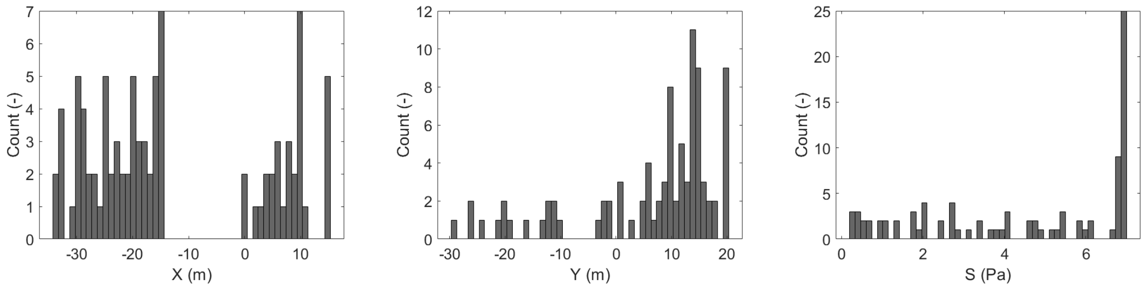

(a) Histogram for the x-location. (b) Histogram for the y-location. (c) Histogram for the source strength.

Figure 8.6: Histogram plots for the source parameters found by GO a B747-800 in take-off. Two main x-locations are found and a peak is visible for y around 14 m. Several sources found the upper boundary of the source strength at s = 7 Pa.

Analogous to Section 8.1, the results for a single frequency are shown with acoustic source maps. The first three source maps are made at an height of 250 m which is in line with the ADS-B height. These source maps are thus comparable to those in Section 7.2. An extra source map is added here, Figure 8.7d, with the CSM constructed based on the parameters GO found, however, at the height at which the GO algorithm was set in the end, h = 260 m. This energy landscape represents what is expected to be the real acoustic source map.

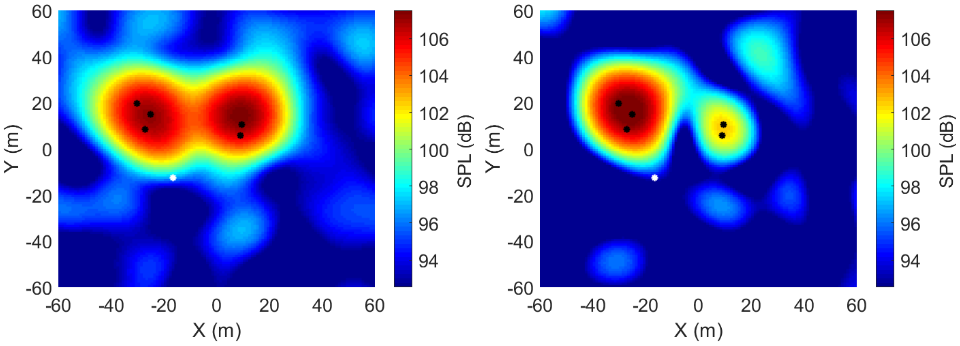

(a) CB source map for the one-third octave band 31. (b) CB source map for the single frequency.

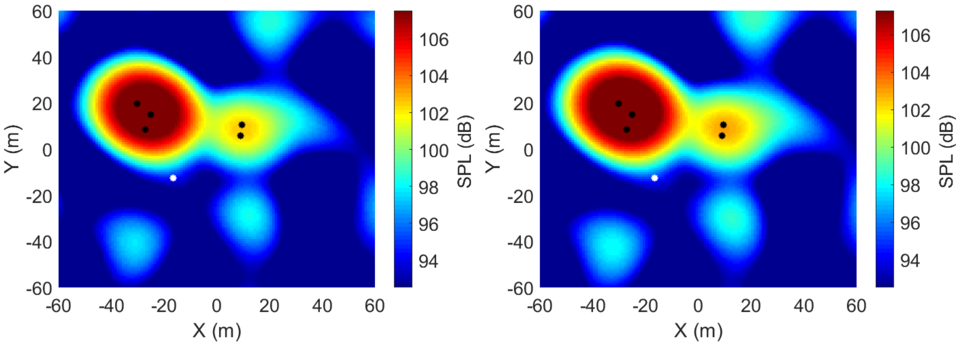

(c) CB source map for the GO results at the same height as the CB results. (d) CB source map for the GO results at the height found by GO.

Figure 8.7: CB acoustic source maps to represent the sources found by GO with the CSM energy function for the B747-800 in take-off at a frequency of 1180 Hz. All source maps use the same colour scale. The first two figures are constructed with measurement data with the source locations found by GO plotted on top in dots. The last two figures are constructed with the CSM based on the parameters found by GO, constructed at a height of 250 m (left lower corner) and 260 m (right lower corner). The source locations found by GO are too closely spaced together to be the engines. The nose landing gear (white dot) is also not in the middle of the two high energy regions as it should be. The source strengths are strongly overestimated. The difference in height of 10 m between the lower two figures causes the main lobe to spread more for higher heights.

Figure 8.7d is added to see the impact of height on the source map. From comparison it appears that the high acoustic energy areas are slightly larger for $h = 260$ m. Figures 8.7c and 8.7d show the acoustic source maps with a CSM based on the parameters found by the GO with the CSM energy function at a frequency of 1180 Hz.

In Figure 8.7 it strikes immediately that at this single frequency the left side of the aircraft has a higher SPL region than the left side. GO finds multiple source locations under the Rayleigh limit as the simulated data set proved earlier. The locations found should be the engines, however they are too closely spaced. Furthermore the nose landing gear location is incorrect, as it is far from the higher energy region in Figure 8.7b. Regarding the source strength, a comparison is made between Figure 8.7d and Figure 8.7b. Clearly, the high energy region is larger for the source map constructed with GO sources, which means that the source strength for the engines is overestimated. Also the size of the main lobes and side lobes as well as their location do not match between the source map based on measured data and modelled data. Thus, there is uncertainty about the 'engine sources' found.

The convergence plots for this search at a frequency of 1180 Hz are shown in Figure 8.8. It shows that the algorithm converges within 100 generations, but goes multiple times to the boundaries. This indicates that the search boundaries are not wide enough and that the source solutions presented in this section, might indeed not be correct.

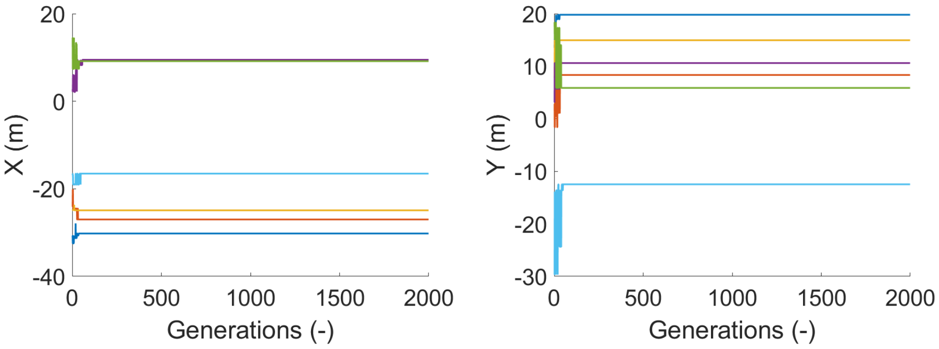

(a) Convergence for the x-direction.

(b) Convergence for the y-direction.

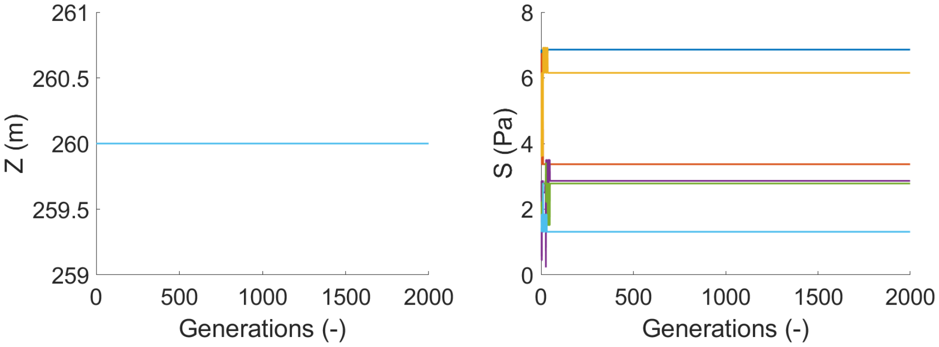

(c) Convergence for the z-direction.

(d) Convergence for the source strength.

Figure 8.8: Convergence plots of the source parameters for the B747-800 in take-off as found by GO with the CSM energy function for a frequency of 1180 Hz. Each colour represents the same source in all convergence plots. Six sources are searched for in this data set. Convergence is achieved within 100 generations, however, for most sources the boundaries are found.

In conclusion, the weighted histogram in Figure 8.5 gives hardly a conclusion on the height. The large distance of the aircraft to the microphone array not only gives the far-field problem, but also gives rise to another problem, i.e. a high amount of signal disturbance (a low SNR) could be introduced when the signal propagates to the microphones. These problems combined, could cause trouble in finding the source height, but also the source location.

From the source maps in Figure 8.7 it is visible that the engine locations found are too close together. Therefore, currently the method is deemed unsuccessful for the LF band. For future research, first a test on the HF band for take-offs should be performed. In the HF band, the engines are separately visible as can be seen in Figure 7.6b. If GO finds the engines correctly in the HF band, as happened for the landing case, one can state whether GO works at all for take-off measurements. If GO is proven to be successful on the HF band, the LF band can be analysed again for less sources and with stricter boundaries per source. Also geometry restrictions as the minimum distance between the engines could be added to improve the results for the take-off case.

9

Conclusions and recommendations

In this chapter, the conclusions drawn from this research are presented in Section 9.1. Several recommendations for future research based on these conclusions are presented in Section 9.2.

9.1. Conclusions

The objective of this research was to assess the use of GO as imaging method to localise and quantify acoustic sources on real fly-over data. For the assessment, a DE algorithm with two energy functions is used; an energy function based on CB, referred to as BF energy function, and an energy function based on CSM-matching, referred to as CSM energy function. The algorithm was applied to four different measurement sets: 1. three speakers set up in an anechoic room at different distances to the array, 2. a simulation of an aircraft fly-over during take-off, 3. a measurement of an aircraft fly-over during landing, and 4. a measurement of an aircraft fly-over during take-off. Measurement set 3 and 4 result from an extensive measurement campaign at Amsterdam Airport Schiphol. The results will be discussed in the same order as these four cases.

GO in combination with the CSM energy function has been applied to the anechoic room measurements to test the use of GO when the sources do not have the same z-location. Here it is not possible to analyse the sources with a single CB source map as they are not located in the same scan plane. GO had difficulty to find the correct z-locations, but identified the x- and y-location perfectly. The source strength was also found correctly. This case also showed that GO with the CSM energy function is able to identify sources in (x, y) under the Rayleigh limit.

The second case allowed for an extensive comparison of energy functions on simulated data. The BF energy function proved to converge faster than the CSM energy function due to the lower number of search parameters. However, the BF energy function is not capable of identifying sources under the Rayleigh limit. The CSM energy function does not suffer from this limitation.

Next to single frequency analysis, multi-frequency energy functions for both the BF and CSM energy function have been tested. The multi-frequency energy functions only improved the results marginally, while the computational time strongly increased. Lastly, the search for a z-location per source was replaced by searching one z for the whole aircraft. In this case, the CSM energy function overestimates z while the BF energy function is capable of finding the z matching with most sources.

After the analysis of simulated data, a basic analysis on the fly-over measurements was performed. Although from prediction with ANOPP the main landing gear was expected to be visible in CB source maps, for both the landing and take-off case they are not visible. The engines are dominantly visible for both cases in all frequency bands. The basic analysis also showed that the take-off case suffered from strong spectral leakage caused by a strong low frequency noise source when no weighting was applied to the data. From literature research, the low frequency source is hypothesised to be caused by interference of the jet stream with the wing.

Lastly, GO was applied to the fly-over measurements to reach the objective. For neither cases, with neither energy function, GO was able to find the aircraft height. This might be due to the low SNR of real fly-over measurements with respect to the high SNR of an anechoic room experiment or simulated data. The single frequency CSM energy function was applied on a range of frequencies from 1120 to 1400 Hz. The algorithm made use of a fixed height found by analysing CB source maps. GO did find the correct source locations for the landing case and the correct source strengths for the engines. The source strength for the landing gear was overestimated. For the take-off case at this frequency the sources are located within the Rayleigh distance. The source locations were not found correctly and the source strengths were overestimated. This is perhaps due to the low SNR of outdoor measurements, while the capability to see under the Rayleigh limit was tested with cases of high SNR.

Overall, this research concludes that GO is a promising method to identify noise sources. However, a set of recommendations is provided to improve the performance of GO in low SNR cases.

9.2. Recommendations

This insights obtained in this research, led to recommendations for future research on this topic. First a set of recommendations for the measurement set-up is provided.

- The calibration of the microphones as explained in Appendix B is a tedious process. To save time on the calibration process for future MCs, a single high quality microphone can be added in the centre of the outdoor microphone array. This would provide a constant reference for the signals measured by the rest of the array. Additionally, a second pistonphone at a different frequency could be added to the equipment. This gives a fast idea of the offset of a microphone at different frequencies and replaces the need of an extensive comparison in an anechoic room.
- It would be ideal to have access to the Flight Data Recordings (FDR) data from the aircraft or to airport radar data. This extra data can serve as verification or reference to the ADS-B data and will provide better insight into the real aircraft position.

For the experimental take-off case, GO did not provide satisfying results for the analysis where sources are not separately distinguishable (i.e. are closer spaced than the Rayleigh limit). Several recommendations are suggested to further assess the applicability of GO for this case. Note that only the GO algorithm with the single frequency CSM energy function is considered here for its use in finding sources under the Rayleigh limit.

- Noise can be added to the simulated data set to see the effect of signal disturbance on the localisation and quantification of the sources in the far-field of the microphone array.
- The use of GO for the take-off case can be tested by applying it on the HF band first where the four engines are clearly distinguishable. If GO passes this test and is able to identify the engines as it did for the landing case, then a following test can be done. By removing artificially the measurements of the outer microphones, the aperture of the array is decreased. If the aperture is decreased to an extent where in the HF case the engines are not distinguishable, GO can be applied again. If GO still identifies the sources, it proves its capability to identify sources under the Rayleigh limit when the SNR is low. If GO does not identify the sources, the below recommendations can be implemented to improve the algorithm.
- The aircraft geometry can be used to restrict the search by GO when it is implemented in the energy function. The geometry constraint can be used to discriminate better the sources in the LF band for take-offs. It can be implemented as a minimum distance between the sources found by GO, e.g. for the inner engines of a B747-8 this would be 25 m [27]. Additionally, a geometry constraint could improve the search for the aircraft height. It can be implemented such that the z-location of sources is set respective to the average height of all sources. This can be very useful for the landing case and anechoic room case as well, where a similar difficulty in finding z was perceived.
- Multiplication factor F and crossover probability p_c could be set to different values, such as 0.6 and 0.55 respectively. Increasing F and decreasing p_c allows for a broader exploration of the search zone. This increases the number of generations needed for convergence, but could aid in finding optima better.
- The CSM energy function can be aided in its search by removing the contributions from known sources from the CSM, thus leaving only a search for the unknown sources.

Lastly, from this research three interesting leads followed for future research. These recommendations can potentially require their own research.

- It is strongly advised to investigate whether the low frequency noise source could indeed be caused by interference of the exhaust jet stream with the wing trailing edge as is suggested in Section 7.3. This can be done in a wind tunnel experiment where an engine and wing are set up. When in the future the results of GO with a BF or CSM energy function are satisfactory, GO might also aid in the analysis. However, in that case the energy function needs to be adapted. Currently the energy functions are based on incoherent sources, but interference noise presents a coherent source system.

- GO proved to be able to find sources far under the Rayleigh limit in simulations and in the anechoic room, where a high SNR is achieved. This raises the question if there is a new limit to which sources still can be distinguished from each other with GO combined with the CSM energy function. This can be tested with simulations or in anechoic room experiments.

- When the current microphone array will be used again for far-field measurements, it is suggested to base the energy function on another type of imaging. The wavenumber beamforming algorithm is proposed to test first. This is the algorithm with which the Underbrink array is tested for the far-field in [13].

Bibliography

[1] Boeing. Commercial market outlook 2018-2037. `https://www.boeing.com/resources/boeingdotcom/commercial/market/commercial-market-outlook/assets/downloads/2018-cmo-09-11.pdf`, 2018. [Last visited: May 28, 2019].

[2] ICAO Air Transport Bureau. Apr 2019: Air transport monthly monitor - world results and analyses for feb 2019. `https://www.icao.int/sustainability/Documents/MonthlyMonitor-2019/MonthlyMonitor_April2019.pdf`, 2019. [Last visited: May 28, 2019].

[3] J.L. Peters, C.D. Zevitas, S. Redline, A. Hastings, N. Sivoz, and J.E. Hart, J.I. Levy, C.J. Roof, G.A. Wellenius. Aviation noise and cardiovascular health in the united states: a review of the evidence and recommendations for research direction. *Current Epidemiology Reports*, 5(2):140—-152, 2018.

[4] WHO Regional office for Europe. Environmental noise guidelines for the european region. Technical report, World Health Organization, 2018.

[5] European Commission. Flightpath 2050 - europe's vision for aviation. Technical report, Publications Office of the European Union, 2011.

[6] L. Bertsch. *Noise Prediction within Conceptual Aircraft Design.* PhD thesis, Technischen Universität Carolo-Wilhelmina, 2013.

[7] J. Piet, U. Michel, P. Böhning. Localization of the acoustic sources of the a340 with a large phased microphone array during flight tests. *8th AIAA/CEAS Aeroacoustics Conference & Exhibit*, 2002.

[8] R. Stoker, Y. Guo, C. Streett, N. Burnside. Airframe noise source locations of a 777 aircraft in flight and comparisons with past model-scale tests. *9th AIAA/CEAS Aeroacoustics Conference and Exhibit*, 2003.

[9] H.A. Siller. Localisation of sound sources on aircraft in flight. *Berlin Beamforming Conference 2012*, February 2012.

[10] D. Nijhof. Assessing the performance of two new acoustic imaging techniques. Delft University of Technology, January 2018. MSc thesis.

[11] A.M.N. Malgoezar, M. Snellen, R. Merino-Martinez,D.G. Simons, P. Sijtsma. On the use of global optimization methods for acoustic source mapping. *The Journal of the Acoustical Society of America*, 141(1): 453–465, 2017.

[12] S. Leusutthiviboon, A. Malgoezar, M. Snellen, P. Sijtsma, D.G. Simons. Improving source discrimination performance by using an optimized acoustic array and adaptive high-resolution clean-sc beamforming. *Berlin Beamforming Conference 2018*, March 2018.

[13] Z. Prime, C. Doolan. A comparison of popular beamforming arrays. *Australian Acoustical Society*, Victor Harbour, November 2013.

[14] S. Doljé. Quantifying microphone array directivity. Delft University of Technology, December 2017. MSc thesis.

[15] The OpenSky Network. `https://opensky-network.org/`, 2019. [Last visited: November 11, 2019].

[16] W.H. Dalmeijer. Gebruiksprognose 2019. Technical report, Schiphol Group, October 2018.

[17] KNMI. Knmi - uurgegevens van het weer in nederland. `https://projects.knmi.nl/klimatologie/uurgegevens/selectie.cgi`, 2019. [Last visited: September 30, 2019].

[18] Leon Brusniak, James Underbrink, and Robert Stoker. Acoustic imaging of aircraft noise sources using large aperture phased arrays. *12th AIAA/CEAS Aeroacoustics Conference (27th AIAA Aeroacoustics Conference)*, 2006.

[19] J. Benesty, J. Chen, Y. Huang. *Microphone Array Signal Processing*. Springer-Verlag, Berlin, 2 edition, 2008. ISBN 978-3-540-78611-5.

[20] R. Merino Martinez. *Microphone arrays for imaging of aerospace noise sources.* PhD thesis, Delft University of Technology, December 2018.

[21] A. Cigada, M. Lurati, F. Ripamonti, M. Vanali. Beamforming method: Suppression of spatial aliasing using moving arrays. *Berlin Beamforming Conference 2008*, February 2008.

[22] Acoustic Camera. Point spread function. `https://www.acoustic-camera.com/en/support/frequently-asked-questions/knowledge-base/point-spread-function.html`, 2016. [Last visited: August 4, 2018].

[23] M. Wilson. Microscope resolution: Concepts, factors and calculation, Dec 2016. URL `https://www.leica-microsystems.com/science-lab/microscope-resolution-concepts-factors-and-calculation/`.

[24] T.J. Mueller. *Aeroacoustic Measurements*. Springer-Verlag, Berlin, 1 edition, 2002. ISBN 978-3-662-05058-3.

[25] R. Merino-Martínez, M. Snellen, D.G. Simons. Functional beamforming applied to imaging of flyover noise on landing aircraft. *Journal of Aircraft*, 53, No. 6:1830–1843, November-December 2016.

[26] AIRBUS S.A.S. A380 aircraft characteristics, airport and maintenance planning - general aircraft dimensions. Technical report, AIRBUS S.A.S. Customer Services, February 2019.

[27] M. Kingsley-Jones. In focus: Boeing 747-8 technical description & cutaway. `https://www.flightglobal.com/in-focus-boeing-747-8-technical-description-and-cutaway/107801.article`, November 2012. [Last visited: December 20, 2019].

[28] S. Luesutthiviboon. Design of an optimized acoustic array. Delft University of Technology, November 2017. MSc thesis.

[29] P. Sijtsma. Experimental techniques for identification and characterisation of noise sources. Technical Report NLR-TP-2004-165, National Aerospace Laboratory NLR, April 2004.

[30] D.G. Simons, M. Snellen, R. Merino Martínez, A.M.N. Malgoezar. Noise breakdown of landing aircraft using a microphone array and an airframe noise model. *Inter-Noise 2017: Taming Noise and Moving Quiet*, Hong Kong:4361–4372, August 2017.

[31] M. Snellen, R. Merino-Martínez, D.G. Simons. Assessment of noise variability of landing aircraft using phased microphone array. *Journal of Aircraft*, 54, No. 6:2173–2183, November-December 2017.

[32] Robert P. Dougherty. Functional beamforming for aeroacoustic source distributions. *20th AIAA/CEAS Aeroacoustics Conference*, 2014.

[33] M. Snellen, D.G. Simons. An assessment of the performance of global optimization methods for geo-acoustic inversion. *Journal of Computational Acoustics*, 16(02):199–223, 2008.

[34] P. Kumar, M. Pant. Noisy source recognition in multi noise plants by differential evolution. *2013 IEEE Symposium on Swarm Intelligence (SIS)*, 2013.

[35] A. Malgoezar, M. Snellen, P. Sijtsma, D.G. Simons. Improving beamforming by optimization of acoustic array microphone positions. *Berlin Beamforming Conference 2016*, February 2016.

[36] R. Storn, K. price. Differential evolution - a simple and efficient heuristic for global optimization over continuous spaces. *Journal of Global Optimization*, 11, No. 4:341–359, 1997.

[37] D. Zaharie. Influence of crossover on the behavior of differential evolution algorithms. *Applied Soft Computing*, 9(3):1126–1138, 2009.

[38] W.E. Zorumski. Aircraft noise prediction program theoretical manual part 1. Technical report, NASA, 1987. NASA Technical Memorandum 83199.

[39] W.E. Zorumski. Aircraft noise prediction program theoretical manual part 2. Technical report, NASA, 1987. NASA Technical Memorandum 83199.

[40] Flugzeug info.net. Boeing 747-8. `http://www.flugzeuginfo.net/acdata_php/acdata_boeing_7478_en.php`, 2019. [Last visited: November 11, 2019].

[41] Modern Airliners. Boeing 747-8 specs. `http://www.modernairliners.com/boeing-747-8/boeing-747-8i-and-8f-specs/`, 2019. [Last visited: November 11, 2019].

[42] D.G. Simons. *Aircraft Noise and Emissions.* Delft University of Technology, January 2019. Lecture notes Course AE4431.

[43] European Union Aviation Safety Agency,. Type-certificate data sheet for engine - genx series engines, December 2019. No. IM.E.102.

[44] GE Aviation. Genx high bypass turbofan engines data sheet, 2004. The GEnx Commercial Aircraft Engine.

[45] D. Hooijmeijer. Dutch aircraft noise model analysis. Delft University of Technology, July 2019. MSc thesis.

[46] L. Rego, D. Casalino, F. Avallone, D. Ragni. Noise amplification effects due to jet-surface interaction. *AIAA Scitech 2019 Forum*, June 2019.

[47] A.P. Piotrowski. Review of differential evolution population size. *Swarm and Evolutionary Computation*, 32:1–24, 2017.

[48] K. Attenborough. Sound propagation in the atmosphere. *Handbook of Noise and Vibration Control*, page 67–78, 2014.

A

Data set of measured aircraft

The data set of measured aircraft is constructed over three days in total, of which two days for take-offs and one day for landings. A single measurement day is called a MC. All measurements took place at location 18C at Amsterdam Airport Schiphol, see Figure 2.6 for the precise location. The weather conditions per MC are listed in Table A.1 [17]. The number of measurements per aircraft type per MC is given in Table A.2. This shows that the A320-200, B737-800, and ERJ190 are the most common aircraft types for the Zwanenburgbaan where the measurements took place.

The landing fly-over measurement used in this research was the second A380 measured during MC3, at time 13:21. The take-off fly-over measurement used in this research was the B747-800 measured during MC2, at time 12:21.

Meteorological condition	**MC1**	**MC2**	**MC3**
Date	June 22, 2019	July 3, 2019	September 24, 2019
Measurement time start-end (h:m)	11:57-17:32	12:01-17:47	11:49-14:30
Operational condition	Take-off	Take-off	Landing
Location at Schiphol	18C	18C	18C
Temperature start-end (° C)	19.4-20.5	17.6-19.6	15.9-17.1
Humidity start-end (%)	66-57	45-48	82-81
Pressure start-end (hPa)	1023.5-1020.3	1026.5-1026.6	1007.9-1006.8
Wind direction start-end	ENE-ENE	N-NNW	SSE-SSE
Wind speed start-end (m/s)	4-6	4-7	7-7

Table A.1: Meteorological conditions during the different MCs [17]. On MC3 rain was pouring in the afternoon, explaining the short measurement time frame.

Aircraft type	**MC1**	**MC2**	**MC3**
A319-100	2	8	5
A320-100	0	0	1
A320-200	10	16	9
A320neo	0	1	0
A321-100	0	1	0
A321-200	4	4	3
A330-200	4	3	3
A330-300	0	4	1
A380	1	0	2
B737-500	1	0	0
B737-700	8	11	6
B737-800	38	26	21
B737-900	1	4	2
B747-400	0	2	2
B747-800	0	1	0
B757-200	0	0	1
B767-300	1	0	3
B777-200	1	1	1
B777-300	0	2	3
B777-F1	0	4	0
B787-9	0	2	3
B787-10	0	1	0
Background	3	3	2
CRJ-7	2	3	0
CRJ-9	0	1	0
ERJ145	1	0	0
ERJ175	15	16	2
ERJ190	12	16	14
ERJ195	2	2	1
Havilland dash8-400	0	0	1
Total	106	132	86

Table A.2: Number of measurements per aircraft type, sorted per MC. In total 238 take-offs are measured (during MC1 and MC2), while 86 landings are measured during MC3. The aircraft types are sorted per manufacturer. Background measurements are performed for reference. A320-300, B737-800, and ERJ190 are the most common aircraft types for the Zwanenburgbaan at Amsterdam Airport Schiphol.

B

Microphone calibration

The microphones in the set-up degrade slightly over time, causing deviations between the true pressure of a sound source and the measured pressure of that source. This influences the acoustic sources maps and thus to counteract this, the measurement system is calibrated. First the DAQ is calibrated in Section B.1. After that the microphones are calibrated with a pistonphone in Section B.2. Lastly a microphone attenuation check is performed over a larger frequency range, see Section B.3.

B.1. Calibration of the DAQ

It is especially important for the DAQ to have all signals in phase as the acoustic imaging technique relies on calculated phase differences. Thus, a phase difference inside the DAQ could translate in wrong acoustic source maps.

The performance of the DAQ is tested with a signal generator for a single frequency and multi-frequency case. First the 1000 Hz signal is applied. An analysis on amplitude and phase deviations of the output signal is performed, but no deviations between the channels are found. Then a signal consisting of frequencies 0.5, 1, 2.5, 3, 4, 5, 10, 15, and 20 kHz is applied to all channels. The output for this signal is also checked for amplitude and phase, and now one channel is ill-performing, see Figure B.1.

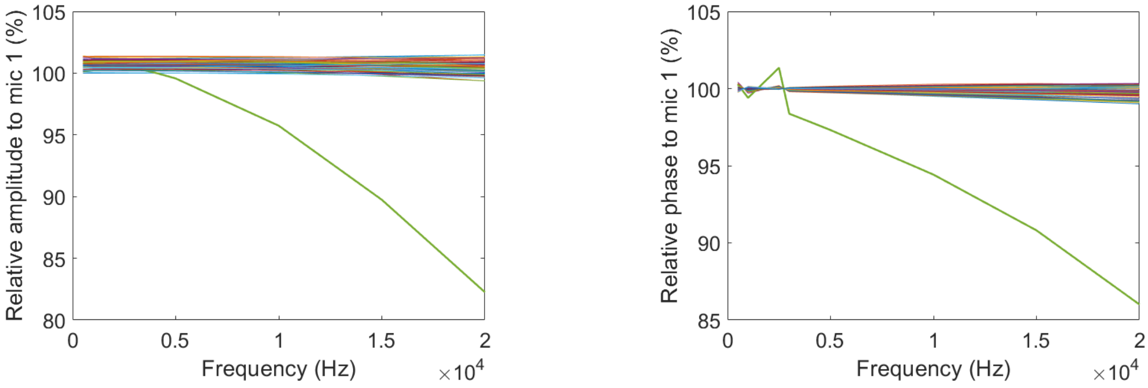

(a) Relative amplitude of the signals with respect to microphone 1.

(b) Relative phase of the signals with respect to microphone 1.

Figure B.1: Calibration of the output signal of DAQ camera 2 for a multi-frequency input signal. The relative amplitude and phase of all channel outputs over frequency is plotted. They are made relative to channel 1. Ideally, all outputs are 100% and thus exactly the same as microphone 1. However, channel 40 is ill-performing for higher frequencies for both the amplitude and the phase.

This analysis showed that channel 40 has a large offset in both phase and amplitude, and thus is taken out of the data. This malfunctioning could not be seen in the single frequency case as the offset starts well above 1000 Hz.

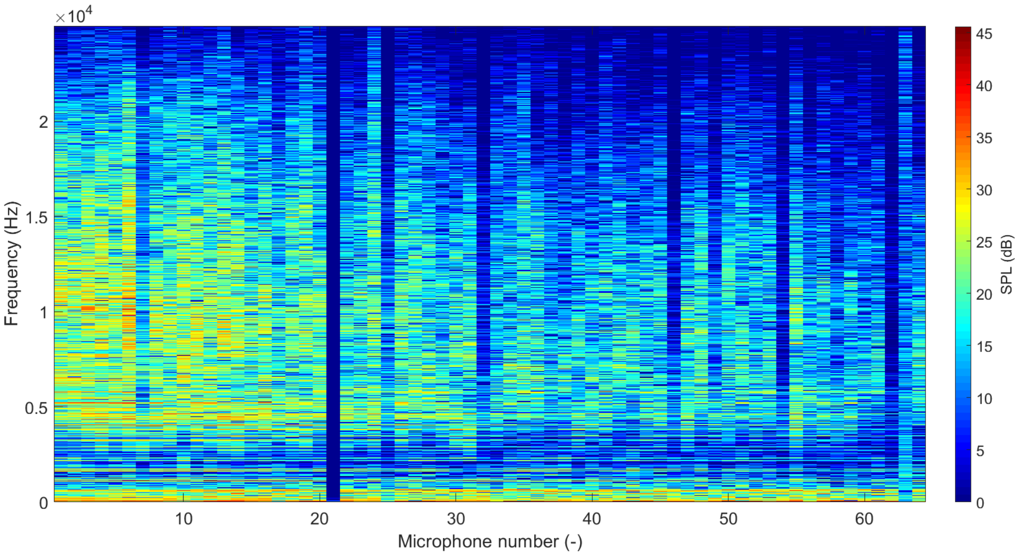

Figure B.2: SPL output for all microphones over frequency for a reference measurement in the Cyberzoo. The higher the microphone number, the lower the output should be as they are further away from the source. Clearly microphone 21 is broken and microphone 63 is ill-performing at lower frequencies. Also for some microphones offsets at higher frequencies are seen.

B.2. Microphone calibration with a pistonphone

First, the general microphone performance is checked. This is done by analysing the time response of a microphone and by checking the output over frequency for the microphones in a test set-up in the Cyberzoo of Delft University of Technology. The latter is shown in Figure B.2.

From Figure B.2 it can be seen that microphone 21 is broken. Also microphone microphone 63 is ill-performing with hardly any output at low frequencies. These microphones thus are taken out of the data set. Furthermore this figure shows that several microphones find lower or higher values than their neighbours. This is in part due to the location of the sound source with respect to the microphones. The other part is caused by general attenuation differences per microphone which are evened out with a correction factor. The correction factor is calculated through an initial calibration with a pistonphone which emits a pure tone of 1000 Hz at 93.8 dB. This pistonphone has to be placed over a single microphone. The data of the microphone is read and a correction factor is determined based on the effective pressure as measured by the microphone. The equation for the correction factor is given in Equation B.1. Note that not only the correction factors of the individual microphones are gathered by doing this, but the correction factor also includes the correction factors needed for the DAQ due to impedance differences of the microphones. In Equation B.1 the effective pressure is calculated by averaging the signal over a time snapshot of 1 s.

$$f_{cor,m} = \frac{p_{eff,93.8dB}}{p_{eff,meas,m}} \tag{B.1}$$

In Figure B.2 deviations between the microphones at higher frequencies are visible. For that, an extensive calibration is performed as presented in Section B.3.

B.3. Microphone calibration in the anechoic room

With the pistonphone available, the microphones can only be corrected at a frequency of 1000 Hz. This way deviations at higher frequencies are not corrected. Therefore a cross-reference of the microphone output is performed with a fully-calibrated and more advanced set of microphones in the A-tunnel facility of Delft University of Technology. This is a vertical flow open-jet wind tunnel in an anechoic room. As the microphones only needed to be calibrated, the air flow was not needed, hence the room functions as anechoic room solely. Here the microphones are placed (per bundle of 8) next to the advanced microphones in the grid, see Figure B.3.

An omnidirectional source with white noise ranging from 315 to 6300 Hz at 63 dBA was used. By comparing the frequency spectrum of an outdoor microphone with the frequency spectrum of its closest indoor micro-

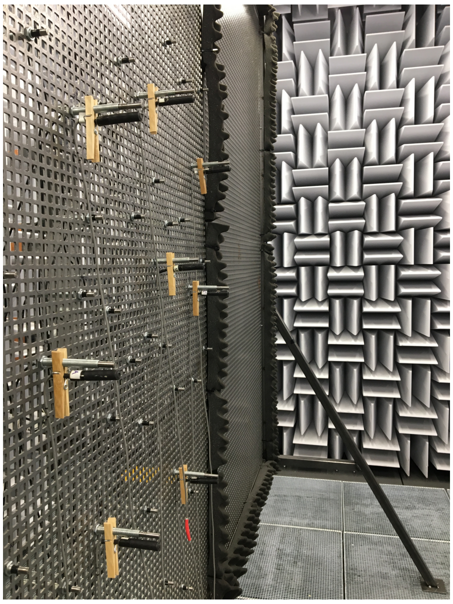

Figure B.3: Mounting of the outdoor microphones (black) under the indoor microphones (metallic) in the array of the A-tunnel anechoic room. The calibration is performed per bundle of 8 microphones.

phone, the attenuation decay of the outdoor microphones becomes visible. Another check can be done by looking at the frequency spectrum of the outdoor microphone solely. White noise should have equal power in each frequency. In other words, the PSD should be constant. Thus, the outdoor microphone should show a constant spectrum.

The analysis of the measurements showed that for most outdoor microphones the PSD results deviated 1 dB at most, see Figure B.4a. However, 5 microphones showed increasing deviations at higher frequencies as can be seen in Figure B.4b. For this research eventually only a small part of the analysis was performed above 6300 Hz, nonetheless the microphones with this behaviour are taken out when the acoustic data is imported for imaging.

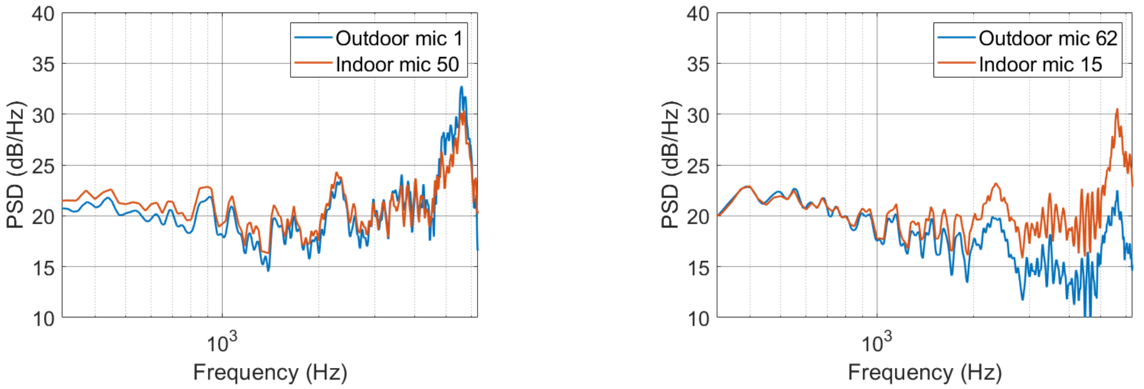

(a) PSD comparison for outdoor microphone 1 with indoor microphone 50.

(b) PSD comparison for outdoor microphone 62 with indoor microphone 50.

Figure B.4: PSD of the indoor microphones with respect to the outdoor microphones. The omnidirectional source generates white noise for a frequency range of 315 to 6300 Hz. For outdoor microphone 1 a slight deviation is visible where below 3000 Hz the outdoor microphone is 1 dB lower than the indoor microphone. Above 3000 Hz the outdoor microphone is 1 dB higher. For outdoor microphone 62 from a frequency of 1000 Hz onward the deviation increases. At 6000 Hz the outdoor microphone has a signal output 6 dB lower than the indoor microphone.

After the calibrations of these three sections, seven microphones are taken out of the analysis. The microphones that are taken out are coloured in the array in Figure B.5.

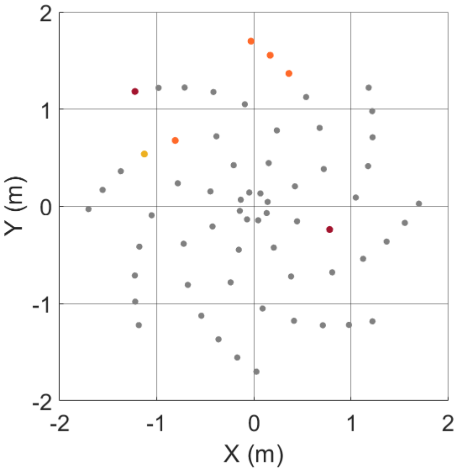

Figure B.5: Indication of the microphones taken out of the data set after calibration. Microphones that are broken (numbers 21, 63) are red. Microphone 40 for which the DAQ is ill-performing is yellow. The microphones with high frequency offsets (numbers 46, 54, 62, 32) are orange.

C

Atmospheric attenuation

When a pressure wave travels through the atmosphere, it is subject to losses. There are three main types of losses: heat conduction, shear viscosity, and molecular relaxation losses. These losses form a low pass filter over the pressure wave, where the high frequencies lose more acoustic energy [48].

The attenuation loss factor α can be described through a series of semi-empirical equations and is applied in Equation 4.10 to correct the SPL.

α can be calculated through the relaxation frequencies of nitrogen ($f_{r,N}$) and oxygen ($f_{r,O}$) which are defined in Equation C.1 and C.2 respectively. These equations are derived from [48].

$$f_{r,N} = \frac{p_{air}}{p_{ref,0}} \sqrt{\frac{T_0}{T_{air}}} \left(9 + 2.8 \cdot 10^4 H e^{-4.17\left((T_0/T_{air})^{1/3}-1\right)}\right) \tag{C.1}$$

$$f_{r,O} = \frac{p_{air}}{p_{ref},0} \left(24.0 + 4.04 \cdot 10^6 H \frac{0.02 + 100H}{0.391 + 100H}\right) \tag{C.2}$$

In the above equations, $p_{ref,0}$ is a reference pressure of 100 kPa, p_{air} is the air pressure during the measurement. T_{air} is the air temperature during the measurement and T_0 is a reference temperature of 293.16 K. H is the absolute humidity during the measurement.

Instead of the relative humidity (RH) as measured by the KNMI, the absolute humidity H as molar concentration of water vapour in air is used in Equations C.1 and C.2. H can be calculated with Equation C.3.

$$\begin{aligned} H &= \frac{\rho_{sat} RH p_0}{100 p_{air}} \\ \text{with } \rho_{sat} &= 10^{C_{sat}} \\ \text{and } C_{sat} &= -6.8346 \left(\frac{T_{sat}}{T_{air}}\right)^{1.261} + 4.6151 \end{aligned} \tag{C.3}$$

p_0 is the standard atmospheric pressure of 101.325 kPa. C_{sat} is the saturation constant, for which T_{sat} equals 273.16 K.

These equation are used as input in the calculation of the attenuation coefficient α, see Equation C.4. α is thus dependent on frequency, humidity, temperature, and pressure.

$$\alpha(f) = f^2 \left(\left(\frac{1.84 \cdot 10^{-11}}{\sqrt{\frac{T_0}{T_{air}}} \frac{p_{air}}{p_0}} \right) + \left(\frac{T_0}{T_{air}} \right)^{2.5} \left(\frac{0.10680 e^{-3352/T_{air}} f_{r,N}}{f^2 + f_{r,N}^2} + \frac{0.01278 e^{-2239.1/T_{air}} f_{r,O}}{f^2 + f_{r,O}^2} \right) \right) \tag{C.4}$$

In Equation C.4 the unit of α is Nepers/m, which is based on a natural logarithmic scale. This can be used when correcting the pressure data directly, see Equation C.5.

$$p_{cor}(t,r) = p e^{-\alpha r} \tag{C.5}$$

To transform it to a base-10 logarithm scale to apply it as in Equation 4.10, α is multiplied with a factor $\frac{20}{ln(10)}$ and has a unit of dB/m.

D

Background information on data processing

The DAQ saves raw data as signed 16 bit integers, which must be converted to Volts in order to be usable for post-processing the data. Moreover the calibration from Appendix B needs to be applied. The steps that need to be taken from reading the data to using it for calculations, are presented in a flow chart in Figure D.1.

The bits to Volts calculation is performed by multiplying the data with a factor of 2.5/32768. For the measurements presented in this report, the low amplification factor needs to be used. Following that, the calibration factors are applied which are determined from the pistonphone calibration explained in Section B.2.

The signal is reduced to only the selected snapshot of 0.05 s at the overhead time. At the sampling frequency of 50 kHz this snapshot results in 2500 samples. Note that with this snapshot time the frequency resolution is 20 Hz. The data columns with the broken microphones are then removed. Seven microphones are taken out. See Figure B.5 for the defective microphones.

For each of the remaining microphones the signal is Hanning weighted to reduce the side lobe levels in the frequency spectrum. Following that, zero-padding is applied to the time domain signal to decrease the frequency spacing in the spectrum. By zero-padding to lengthen the signal to a power of 2 length, the Fast Fourier Transform (FFT) is computed faster. Note that this will not result in resolving two frequencies spaced closer together than 20 Hz. It will however give a better representation of the filter function and thus a better representation of the spectrum.

Now these steps are all performed, the FFT algorithm from Matlab can be applied to the time domain signal. The result is essentially a filter bank where at each frequency the filter from the window is present.

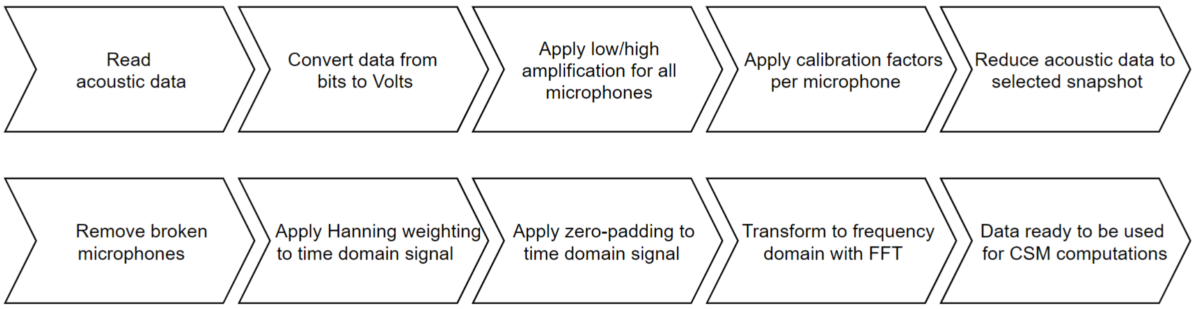

Figure D.1: Consecutive steps for the data processing. The process starts at the saved raw data file of the DAQ. After the last step, the researcher can use the data for calculations of source maps or PSDs.